HIGH RESOLUTION QUANTITATIVE OPTICAL COHERENCE TOMOGRAPHY FOR TISSUE IMAGING

JUN NI

(B. Eng., M. Eng., Shanghai Jiao Tong Univ., China)

A THESIS SUBMITTED FOR THE DEGREE OF

MASTER OF ENGINEERING

GRADUATE PROGRAM IN BIOENGINEERING

NATIONAL UNIVERSITY OF SINGAPORE

2007

ACKNOWLEDGEMENT

I would like to express my sincere gratitude to my supervisors, Associate Professor Ong Sim Heng and Associate Professor Hanry Yu, for giving me an opportunity to work in the bioimaging field and supporting me as I deal with innumerable challenges during this project. They have provided me incredible resources and collaborations to complete this thesis. Their guidance and patience in sharing their many years of research experience will always be appreciated.

I would also like to thank Dr. Sun Wan Xin, Ms. Chong Kwang May, Mr. Alvin Kang Chiang Huen, Ms. Min Xiao Shan for their valuable discussion.

I am also grateful to Lab officer Francis, Ph.D. students Hiew Litt Teen, Ng Hsiao Piau, and other members in the Vision and Image Processing lab who helped to provide a friendly and enjoyable working environment.

I wish to thank Ph.D. students San San Susanne Ng, Du Ya Nan, Zhao De Qiang, and other members in Tissue Engineering lab for their collaboration and encouragement.

Finally, I would like to thank my friends and my family, especially my parents and brother, without whose support and understanding none of this would have been remotely possible.

Extended appreciation goes to NUS for financial support and IBN for good research facilities during the course of research for my master degree.

SUMMARY

Optical coherence tomography (OCT) is a relatively new non-invasive imaging technique. As it can provide high-resolution, three-dimensional imaging of the internal microstructure of living tissue in real time and in vivo, it has been particularly useful in several biological fields, such as tissue engineering, drug discovery, and ophthalmology. With increasing potential applications in these fields, much research work has been performed to develop high resolution (micro scale), high speed (several frames/second) OCT systems.

In this project, the design and implementation of time-domain OCT system are discussed. Some key technologies have been investigated:

(1) Envelope detection technology. Fast Fourier Transform (FFT) method and Hilbert Transform (HT) method have been used to analyze the interferometric signal of time-domain OCT system. They show near-perfect envelope detection results under different conditions. However, less than 1.5 oscillations inside the envelope will limit their performance and degrade the envelope detection effects. Experimental results show that about 1.5 oscillations inside the envelope is enough for them to extract the envelope.

(2) Design of optical delay line. A rapid-scanning, high-repetition-rate, and long group delay optical delay line is important for real time OCT system. Fourier domain optical delay line (FD_ODL) has this capability and its actual optics design has been further optimized in our works. Some important relationship among optics components has been derived and their design parameters have been calculated. These will provide valuable guidance to set up FD_ODL. Geometric ray tracing analysis method has been used to analyze the dispersion problem of FD_ODL when a broadband light source was introduced. An appropriate optics layout has been

proposed to minimize the dispersion problem.

(3) 3D sample probe. A hand-held sample probe was used as the sample arm of the OCT system. As a two-axis scanning mirror was incorporated into the sample probe, it provides the OCT system real-time, 3D imaging capability. Some important relationship inside the sample probe has been derived.

(4) Image processing technology. To suppress the speckle noise and improve the quality of the OCT image, nonlinear PDEs-based denoising approaches have been investigated. They achieved good noise suppression and edge preserving effects. Segmentation and feature quantification of the OCT image are also important in practical applications. Fast marching method was used to extract the targeted curves in the OCT image and experimental results have been given.

LIST OF TABLES

LIST OF FIGURES

Figure 5.25 Calculated time map U using Figure 5.21

Figure 5.26 Bottom surface on Figure 5.21

Figure 5.27 Calculated time map U using Figure 5.22

Figure 5.28 Top surface on Figure 5.22

Figure 5.29 Calculated time map U using Figure 5.22

Figure 5.30 Bottom surface on Figure 5.22

TABLE OF CONTENTS

Chapter 1 Introduction

1.1 Background

During the past decades, many minimally invasive real-time imaging techniques have been developed with the increasing requirements of biological and medical applications. These techniques can perform three-dimensional visualization of biological samples and have become the most powerful investigative tools in biological and medical fields. They can be used to dynamically monitor object of interest in the patient and allow doctors or researchers to understand its disease states better.

These techniques provide powerful diagnosis means and greatly promote the research in biological and medical fields. They have their own advantages and disadvantages. For example, ultrasound imaging [1] can only achieve a few millimeters penetration depth because of acoustic attenuation in tissues, however with high resolution of 20 to 30 μm. X-ray computed tomography (CT), magnetic resonance imaging (MRI) [2], and diffuse optical tomography (DOT) can achieve several millimeters penetration depth, but their resolution is typically limited to a few millimeters. Confocal microscopy [3] is able to obtain high axial and transverse ($\leq 1\ \mu m$) resolution imaging, but with fairly low penetration depth, and therefore its in vivo applications has been limited.

Optical coherence tomography (OCT) is a novel, rapid, noninvasive optical imaging technology that emerged in the past decade [4]. It is similar to ultrasound, measuring the intensity of the interferometric signal between back-reflected light from tissues and reference light. The signal intensity is acquired by electronic hardware and assessed as a function of depth, which can reveal the tissue structure discontinuities. With advances in laser and optical fiber technology and the utilization of broad-bandwidth light sources, OCT systems can be implemented at low cost and

are able to image tissues on the micron scale with penetration depth of 2-3 millimeters [5-9]. So OCT has a great impact on the progress of bioimaging.

As OCT can provide high-resolution, two- or three-dimensional cross-sectional imaging of microstructure of transparent and nontransparent biological tissues in situ or in vivo, which has previously only been possible with histopathology, it has attracted much interest from biologists, clinicians, and material scientists, and so on [10-18]. It has been used to investigate many aspects of the human body, including the brain [19], skin [20, 21], blood vessels [22-24], and the eye [25].

One of the most successful applications of OCT system is in the field of ophthalmology. For example, high-resolution, cross-sectional imaging of the anterior segment of the lens, iris, corneal, and intra-ocular lens implants are performed to assess abnormalities of the anterior architecture of the eye. Retinal imaging was obtained to diagnose macular conditions and glaucomatous damage, etc. [26-34]. In addition, OCT is beginning to play an important role in tissue engineering, drug discovery, and cell biology [35]. It has been used to monitor cell dynamics in cell-based tissue models, including migration, proliferation, cell-material interactions. Many of the details related to pathologies can be understood in the complex, highly-scattering, thick three-dimensional tissue constructs [35-37].

1.2 Setup of time-domain OCT system

Figure 1.1 shows the basic components of an OCT system. The core of the OCT system is a standard Michelson interferometer where a low coherence light incident on a beamsplitter is divided into two paths; one to a reference mirror, and the other to a sample. The reflected light from them will be recombined and detected by photodiodes followed by signal processing electronics. The detected interferometric signal will be acquired by a high-speed data acquisition

card and analyzed to form the final OCT image using signal processing technologies.

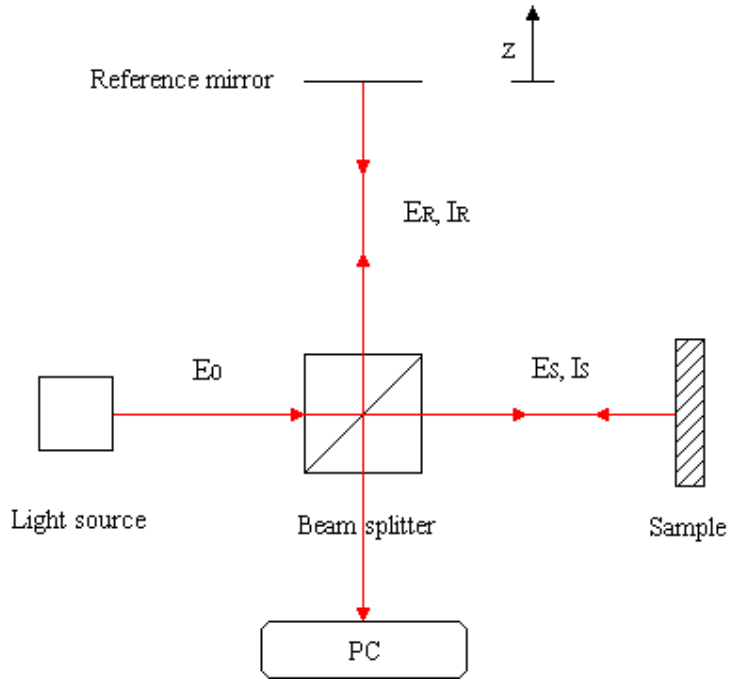

Figure 1.1: Standard OCT scheme based on a standard Michelson interferometer

1.3 Optical coherence technique

It is well known that the OCT system uses optical coherence technique. In fact, if two light waves are to interfere to produce stable interference fringes, they must satisfy three conditions:

(1) They have the same frequency,

(2) There is a constant initial phase difference between them,

(3) Their polarizations are not perpendicular to each other.

However, OCT system is not the first application example of optical coherence technique. Optical coherence technique has been widely used in some early optical microscopies, such as phase contrast microscopy, differential interference contrast microscopy, and polarized light microscopy, etc..

1.3.1 Phase Contrast Microscopy

Phase contrast microscopy is based on the theory of converting slight phase variations into amplitude changes through optical coherence technique. When incoming light from a condenser passes through a sample, it will be divided into two different components, namely surround wave and diffracted wave. Surround wave can pass through the sample without interacting. However, diffracted wave is scattered by the sample. They will interfere in the image plane of the microscopy and the minute phase shift between them will reflect the structure of the sample in detail. Phase contrast microscopy can be used to monitor living cells in vivo without the need for staining [38].

1.3.2 Differential Interference Contrast (DIC) Microscopy

DIC microscopy can be used to monitor living cells in vivo without staining. It uses Nomarski prism to shear the incoming polarized light to produce orthogonal components, viz. ordinary wave and extraordinary wave. These two waves will be focused into parallel components onto the sample by a condenser. After leaving the sample, they will interfere inside the second Nomarski prism and recombine into coaxial components to form an image of the sample. The gradients, due to the refractive index difference inside the sample, will be transformed into intensity differences that can be observed [39].

1.3.3 Polarized Light Microscopy

Polarized light microscopy is mainly used to investigate the structure of birefringent sample. This kind of sample can decompose the incoming polarized light into two components, viz. ordinary wave and extraordinary wave. The analyzer will recombine these two waves and reflect the structure of the sample [40].

1.4 Different OCT image modes

At present, there are two main OCT methods: Time-domain OCT and Fourier-domain OCT.

1.4.1 Time-domain OCT

The system in Figure 1.1, where a reference mirror is rapidly and accurately scanned to match the optical path from the reflected light within the sample, is called time-domain OCT. This type of OCT system analyzes the intensity of interferometric signal between reference light and back-reflected light from biological samples. The envelope of signal will be extracted to form the OCT image.

1.4.2 Fourier-domain OCT

Fourier-domain OCT system measures the time delay and magnitude of optical reflections from the sample in Fourier domain. Back-reflected light from different depths of the sample, which corresponds to different delays, will interfere with light from a reference path with a known delay. The interference spectrum, which is detected by a high-speed spectrometer as a function of wavelength, will be analyzed using Fast Fourier Transform (FFT) method to form the cross-sectional images of biological samples [41-53].

1.5 Design issues for OCT system

The four fundamental issues for OCT system design are optical light source, signal-to-noise ratio, resolution, and the acquisition speed.

1.5.1 Optical light source

The optical light source is one of the core components of an OCT system. Many system characteristics will be influenced by it, for example, spatial resolution, signal to noise ratio (SNR), imaging speed, ease of use, and so on. Some light sources recently used in the OCT system

include superluminescent diodes (SLD), $Ti:Al_2O_3$ mode-locked solid-state laser, and thermal tungsten halogen light source, etc.. Table 1.1 summarizes several light sources that can be used for the OCT system.

1.5.1.1 Key parameters of optical light sources

When we choose optical light source for an OCT system, we often consider its four key parameters: center wavelength l_0, bandwidth Δl, power P_s, and stability [54].

Table 1.1: Examples of optical light sources used in the OCT system

Light source	Center wavelength l_0 (nm)	Bandwidth Δl (nm)	Axial resolution (μm)	Power P_s (mW)
800 nm SLD [55]	800	20-30	10-20	1-10
1300 nm SLD [55]	1300	40-50	10-20	1-5
Ti : sapphire laser [56, 57]	800	250	2	60
Ti : sapphire laser +PCF fiber [58, 59]	800	400	1	150
Thermal tungsten halogen [60]	840	260	1	$100*10^3$

(1) Center wavelength l_0. The incident light will be attenuated in biological tissues by both scattering and absorption which are wavelength-dependent. Scattering decreases with increasing wavelength. However, absorption is relatively low in the diagnostic window about 700 nm-1300

nm, where there exists low water absorption of light [61, 62]. Thus, an optimum center wavelength should be chosen to increase the penetration depth of light into the tissue, so that deeper structure information of biological tissues can be obtained.

(2) Bandwidth Δl . The axial resolution l_c of the OCT system depends on bandwidth and the center wavelength of light source. It can be calculated using the equation [54, 63, 64],

$$l_c = \frac{2\ln 2}{p}\left(\frac{l_0^2}{\Delta l}\right) \approx 0.44\frac{l_0^2}{\Delta l} \tag{1.1}$$

This equation shows that the broader the bandwidth of the source, the better the axial resolution of OCT system. The relationship between the axial resolution and bandwidth of the source for different center wavelengths is plotted in Figure 1.2.

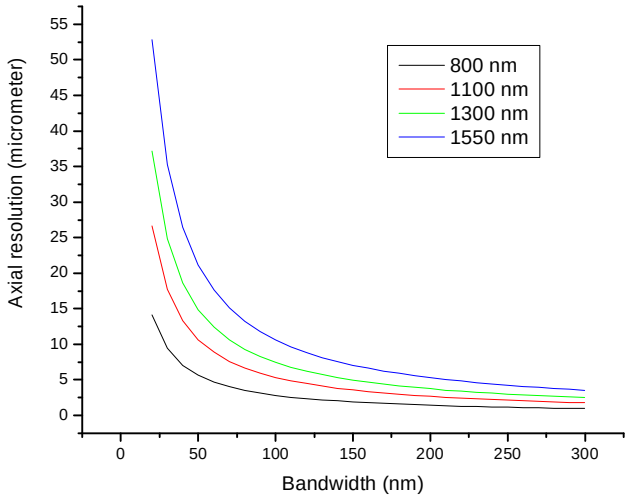

Figure 1.2: Axial resolution versus bandwidth of the source for center wavelength l_0 =800nm, 1100nm, 1300nm, 1550nm, respectively

(3) Power P_s. In order to achieve wide dynamic range and high detection sensitivity (SNR) with rapid scanning acquisition rate, great optical source power P_s is usually needed. In some situations, such as retinal imaging, the power is limited due to the safety concern.

(4) Stability of light source. A simple, portable, and stable OCT system will require a stable, small, and not too complex light source.

1.5.1.2 Superluminescent diodes

Superluminescent diodes (SLD) are optoelectronic semiconductor devices which generate broadband optical radiation based on superluminescence. SLD's mainly consist of an edge-emitting multiple quantum well structure with angled end facets which can minimize optical loss and feedback effects. Most superluminescent diodes are fabricated to operate at various wavelengths such as 800 nm, 1300 nm, and 1550 nm [65].

Its main advantages include high power output, broad optical spectral range and reasonable cost, etc.. In addition, as SLD's are continuous wave (CW) sources, several individual different center wavelength SLD's can be combined to generate broader spectrum at low cost. WDM (Wavelength Division Multiplexing) technology can achieve this synthesis by coupling the output of several sources into a single fiber. This kind of SLD has been commercially available in the market.

1.5.1.3 $Ti:Al_2O_3$ mode-locked solid-state laser

High-resolution OCT was investigated using a Ti: sapphire laser purchased from Femtolasers Company. This laser is based on a low threshold femtosecond oscillator powered by an integrated diode pumped green solid state laser. Generation of ultra-broadband laser radiation directly from a low-loss laser oscillator was achieved using Femtolasers' patented Dispersive Mirror (DM) technology. The schematic of the laser is shown in Figure 1.3. Its spectrum is shown in Figure 1.4.

With an optical bandwidth of about 160 nm at full width at half maximum (FWHM) centered around 800 nm and several tens of milliwatts of output power from a single mode fiber, the axial

resolution of OCT system can achieve about 3 μ m. Hence, the laser is perfectly suited for non-invasive, in vivo ultrahigh resolution OCT [66].

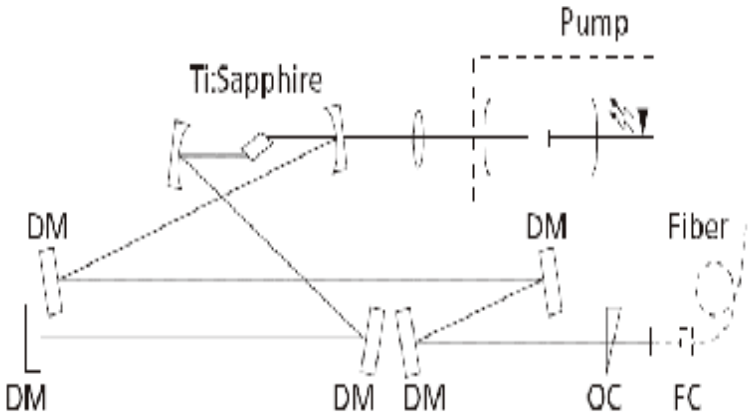

Figure 1.3: Schematic of the laser

DM: Dispersive Mirror, OC: Output Coupler, FC: Fibre Coupler

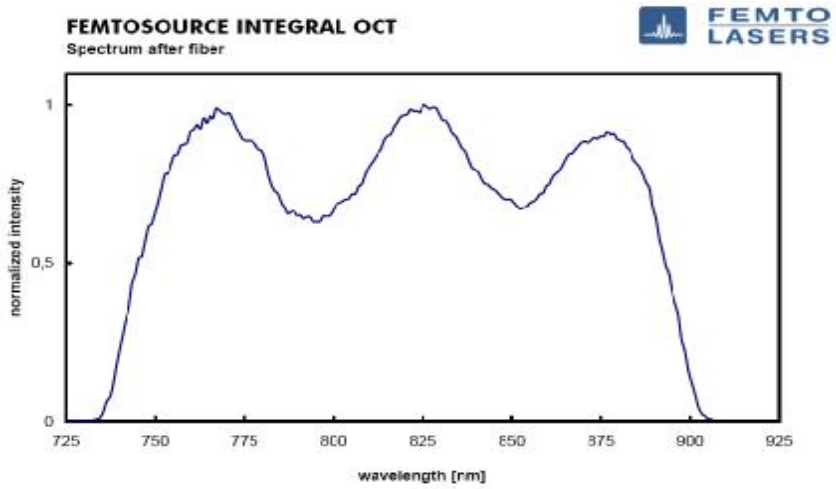

Figure 1.4: Spectrum of the laser

1.5.1.4 Quartz Tungsten Halogen (QTH) light source

The QTH light source was purchased from Newport Oriel Instruments and shown in Figure 1.5. It consists of: (1) Lamp Housing for QTH Lamps, (2) 69931 Radiometric Power Supply, (3) 100 W QTH Lamp (model 6333), (4) 68951 Light Intensity Controller (which can maintain a constant light level), (5) All necessary cables and mounting hardware. The spectrum of model

6333 lamp is shown in Figure 1.6 [67].

Figure 1.5: 66995 QTH Source with 68951 Light Intensity Controller and fiber optics

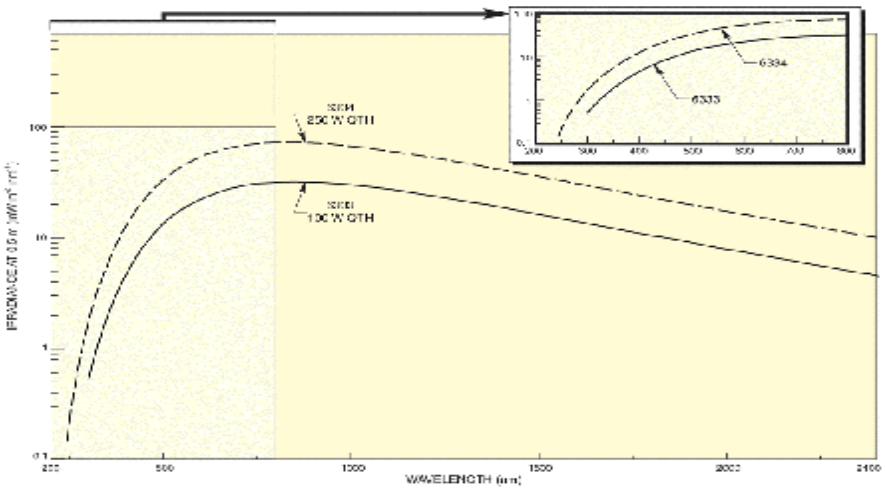

Figure 1.6: Spectrum of quartz tungsten halogen lamps

1.5.2 Signal to noise ratio (SNR)

In an OCT system, the measured signal unavoidably contains noise which comes from both electronic and optical sources. As noise has a significant impact on system performance, we have to consider the main noise sources that exist in OCT system and try to minimize their effects on the system sensitivity [54, 68-71]. The common metric that describes the degree of system sensitivity is signal-to-noise ratio (SNR). SNR is defined as:

$$SNR = \frac{I_S^{\ 2}}{s^{\ 2}} \tag{1.2}$$

where I_S is the signal current caused by the interference between light backscattered from the sample and reference mirror, and $s^{\ 2}$ is the background noise.

When measured in dB, we use

$$SNR = 10\log_{10}(\frac{I_S^{\ 2}}{s^{\ 2}}) \tag{1.3}$$

The main noise sources in the OCT system are the receiver noise $s_{re}^{\ 2}$, the shot noise $s_{shot}^{\ 2}$ and the intensity noise/beat noise $s_{ex}^{\ 2}$ [54].

$$s^{\ 2} = s_{re}^{\ 2} + s_{shot}^{\ 2} + s_{ex}^{\ 2} \tag{1.4}$$

More detailed defines about $s_{re}^{\ 2}$, $s_{shot}^{\ 2}$ and $s_{ex}^{\ 2}$ can refer to appendix B. Proper minimization of their effects on the signal can improve the SNR of the OCT system. Hence, very low intensity levels of backscattered light will be sensitively detected.

1.5.3 Dynamic range (DR)

Dynamic range is one of the most important parameters of an OCT system performance. It is mostly given in dB. SNR decides the minimum detectable optical interferometric signal, while dynamic range is defined as the highest detectable optical power $I_{\max imum}^2$ over the lowest detectable optical power,

$$DR = 10\log_{10}(\frac{I_{\max imum}^{\ 2}}{s^{\ 2}}) \tag{1.5}$$

The detected optical power is proportional to the photoelectrical current. The value of dynamic range is usually smaller than the value of SNR due to the saturation limit of the detection electronics of the system.

1.5.4 Speed

Rapid image acquisition speed is an important capability of an OCT system. It will help biologists to monitor dynamic morphologies of cells in vivo and greatly facilitate their biological experiments. At present, the reported video-rate OCT is implemented separately in time domain and fourier domain.

1.5.4.1 Time domain video-rate OCT system

This kind of OCT system uses high speed optical delay line in the reference arm of the OCT system. Different design methods of optical delay line have been reported, such as linear translation of retroreflective elements, fiber stretching to modify the path-length of the reference arm, and Fourier domain optical delay line. The major function of optical delay line is to perform fast, accurate, stable sweep of the time of flight difference between the reference arm and the sample arm.

1.5.4.2 Fourier domain video-rate OCT system

This type of OCT system has been introduced in 1.4.2, the reference path length is fixed and high-speed CCD is used to record the spectrum of the intereferometric signal. Each A-scan can be acquired in a single snapshot, so it can achieve video-rate acquisition speed. But the OCT system speed is limited by the time that data is transferred from CCD to PC for processing.

1.6 Contrast enhancement OCT

Fluorescence microscopy is a vital imaging tool in biological fields. With antibody-conjugated fluorescence molecules, it has been used to investigate some specific protein functions in biological experiments. However this fluorescence optical technique can only provide low penetration depth. The main reason is that since biological tissues are highly scattering, the backscattered fluorescence photons will cannot be well differentiated from multiple scattering

within tissues. The fluorescence photons from a specific volume of the tissue will unavoidably contain other fluorescence photons from the neighboring volumes [72]. This will increase the background noise in the signal and degrade the image quality. So fluorescence microscopy is not able to provide deep tissue information as the fluorescence signal is attenuated by multiple scattering within the turbid tissue.

OCT works as "coherence gating" and only detects the ballistic component of the light backscattered from a specific depth within the sample. Other backscattered light contributes little to the signal. So it can achieve superior penetration depth compared with fluorescence microscopy. However, as the scattering properties of early-stage pathological tissue are often morphologically or optically similar to that of normal tissue, OCT system is not easy to recognize early-stage tumors. To overcome this limitation, some novel contrast enhancing approaches have been recently proposed to detect early-stage pathological tissue and can be categorized to three types as follows:

1.6.1 Absorption-based method

A specific optically excitable molecular contrast agent, such as methylene blue, is used in this method [73, 74]. This method can be divided into two steps: the baseline OCT signal $I_{\text{int}erference,baseline}(l,z)$ is acquired firstly, then the contrast agent is optically excited and the second OCT signal $I_{\text{int}erference,excited}(l,z)$ is obtained. An intermediate quantity $Q(z)$ can be written as:

$$Q(z)=\frac{1}{\Delta s(l)}\ln\left(\frac{I_{\text{int}erference,baseline}(l,z)}{I_{\text{int}erference,excited}(l,z)}\right)=\int_0^z \Delta m(z_s')dz_s' \tag{1.6}$$

$$\Delta m(z)=\frac{dQ(z)}{dz} \tag{1.7}$$

where $\Delta s(l)$ is the change of absorption cross-section of the contrast agent by optical

excitation. $\Delta m(z)$ is the localized concentration of the contrast agents altered by optical excitation. $\Delta m(z)$ will give the contrast agent distribution within the sample and provide an important pathological information in the sample.

1.6.2 Scattering-based method

Engineered gold-shelled, oil-shelled microspheres are used as contrast agents in this method [75]. These agents can be introduced into the sample and are tagged to site-specific tissues or cells of interest. They increase the sample reflectivity $R(l,z)$, at a center wavelength l, as a function of scanning depth z, in specific sites. The measured interference signal $P_{\text{int}\,erference}(l,z)$ can be expressed as:

$$\begin{aligned} P_{\text{int}\,erference}(l,z) &\approx 2\sqrt{P_{R_0}P_S(l,z)} \\ &= 2\sqrt{P_{R_0}P_{S_0}}e^{-\int_0^z[m_a(l,z_s')+m_s(l,z_s')]dz_s'}\sqrt{R(l,z)} \end{aligned} \tag{1.8}$$

where P_{R_0} is the intensity reflected from the reference arm, $P_S(l,z)$ is the intensity reflected from the sample arm, P_{S_0} is the sample arm intensity if the sample is fully reflective. $m_a(l,z_s)$ is the absorption coefficient, $m_s(l,z_s)$ is the scattering coefficient.

The signal can provide the concentration and distribution information of the contrast agents in the sample and will enhance the diagnostic capability of OCT system.

1.6.3 Coherent emission-based method

Second harmonic generation (SHG) and coherent anti-stokes raman scattering (CARS) are some induced nonlinear processes when strong electric field is incident upon the material [76]. The nonlinear polarization process for a material can be described as below:

$$\overline{P} = e_0(c^{(1)}\cdot\overline{E} + c^{(2)}\cdot\overline{EE} + c^{(3)}\cdot\overline{EEE} + \cdots) \tag{1.9}$$

where $\overline{P}$ is the induced polarization for the material, e_0 is the vacuum permittivity, $\overline{E}$ is the

incoming electric field vector. The first term $c^{(1)}$ represents the linear effect. The second term $c^{(2)}$ is responsible for the nonlinear effect, like SHG. The third term $c^{(3)}$ is responsible for the nonlinear effect, like CARS.

SHG and CARS emission have definite phase relationship with the original incoming light source and are coherent. They have the advantage of interferometric detection and will enhance molecular-specific contrast capability of the OCT system.

1.7 Whole system configuration of time-domain OCT system

We set up the time-domain OCT system as shown in Figure 1.7. Compared to Fourier-domain OCT system, the main advantage of time-domain OCT system includes: (1) It can focus point by point in depth using dynamic focus technology. (2) High numerical aperture objective can be used to enhance the transverse resolution, etc..

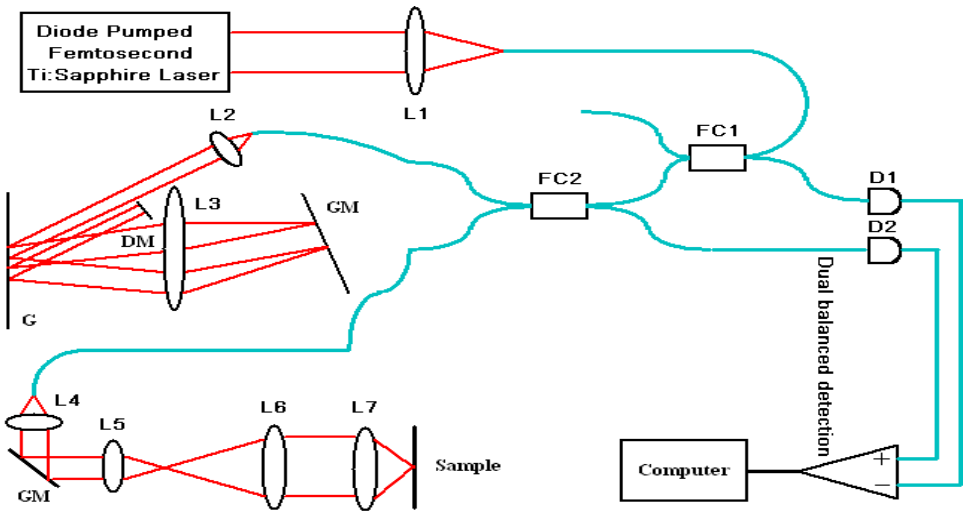

Figure 1.7: Ultrahigh resolution, real time, time-domain OCT system

L1-L7: chromatically corrected doublet, FC1,2: 2x2 fiber coupler, D1,2: InGaAs photodiods, M: mirror, DM: double-pass mirror, G: grating, GM: galvanometer controlled scanning mirror

In this system, the light source is a Ti: Sapphire laser. Its centre wavelength is at 800 nm with a bandwidth about 160 nm and an axial resolution about 3-4 μ m. Some important system

components are listed below.

1.7.1 Detector

The detector used the 125KHZ Nirvana Auto-balanced Photoreceiver (New Focus).

1.7.2 2 x 2 fiber coupler

The 2 x 2 fiber coupler was purchased from Femtolasers Company. It will divide the incoming light into two beams, one of them going to the optical delay line and the other to the sample arm.

1.7.3 Optical light source

The light source used the femtosecond laser from Femtolasers Company.

1.7.4 Data acquisition card (DAQ)

High-speed DAQ cards (model 6251 and model 6115) were purchased from National Instruments. NI PCI-6251 is 16-bit, M series high-speed multifunction DAQ. Single channel can achieve 1.25 MS/s. NI PCI-6115 is 12-bit, S series high-speed multifunction DAQ. Single channel can achieve 10 MS/s.

1.8 Thesis contributions

In this project, we aim to develop a fiber-based, portable and real-time time-domain OCT system. Key contributions in this work are outlined as follows:

1.8.1 Envelope detection of interferometric signal

We investigated the effects of ideal envelope detection technologies, such as FFT and HT methods on the OCT signals under different conditions. These signals were simulated according to the derived formulation of the interferometric signal of time-domain OCT system. Experimental results show good performance of the envelope detection effects.

1.8.2 Investigation of Fourier domain optical delay line

We used Fourier domain optical delay line as the reference arm of the OCT system. Some important relationship equations among its optics components have been derived and its design parameters have been further optimized. Geometric ray tracing method was employed to analyze the dispersion problem of this optical delay line. Its fabrication accuracy has been proposed according to experimental results.

1.8.3 Analysis of the sample arm

We used a deflecting probe, which incorporates an X-Y two-axis scanning mirror, as the sample arm. This design can provide the OCT system with a real-time, 3D imaging capability. Geometric ray tracing analysis method has been employed to analyze the relay optics of the sample arm. Some relationship equations inside the sample arm have been proposed and were used to setup relevant optics components. Its fabrication accuracy has also been proposed according to experimental results.

1.8.4 OCT image analysis

To suppress noise and improve the quality of OCT images, some classical nonlinear PDE-based diffusion methods have been investigated on OCT images. The denoising effects were evaluated using some measurement metrics. In addition, fast marching method was used to segment OCT images.

Chapter 2 Interferometric signal of time-domain OCT system

OCT is a novel, noninvasive imaging technology. Since it was reported in 1991 [4], it has achieved significant progress and has become an important imaging tool for real-time, in vivo optical diagnosis of ocular diseases, cancer and some other diseases [19-37].

OCT is based on the theory of classical low coherence interferometry. As the velocity of light is extremely high, direct measurement of weak reflected light from the sample cannot be performed electronically. So the light reflected from the sample will interfere with the light from the reference mirror at the interferometer or fiber couplers. The interferometric signal can be detected by electronic hardware when the path difference between these two waves is less than the coherence length of the light. The interferometric signal contains the structure information from the sample and can be analyzed to form the OCT image using signal processing technologies, which reveals the sample structure. With optical heterodyne detection, an extremely high detection sensitivity [4] may be achieved with a higher than 100-dB dynamic range. This enables the OCT system to have unique capability to penetrate into tissue samples at a depth of more than 1 mm. Therefore, it has the potential to greatly impact the field on high-resolution imaging on biomedical systems.

2.1 Electronic signal detection

The optical interferometric signal will be converted into an electronic current signal by photodiodes. The produced electronic current is proportional to the incident optical power. It will be converted into a corresponding electronic voltage via transimpedance amplifiers. The data

acquisition card which can be triggered to high-speed, automatically collects the electronic voltage output into a PC system.

2.1.1 Photodetection

A semiconductor photodiode is an important component of the OCT system. It contains a PN junction which consists of the P-layer material at the active surface and the N-layer material at the substrate. When light hits a photodiode, the electron within the crystal structure is stimulated. If the light energy is greater than the band gap energy, electron-hole pairs are generated in proportion to the optical power of incident light. This results in a positive charge in the P-layer and a negative charge in the N-layer, and current will flow in the photodiode.

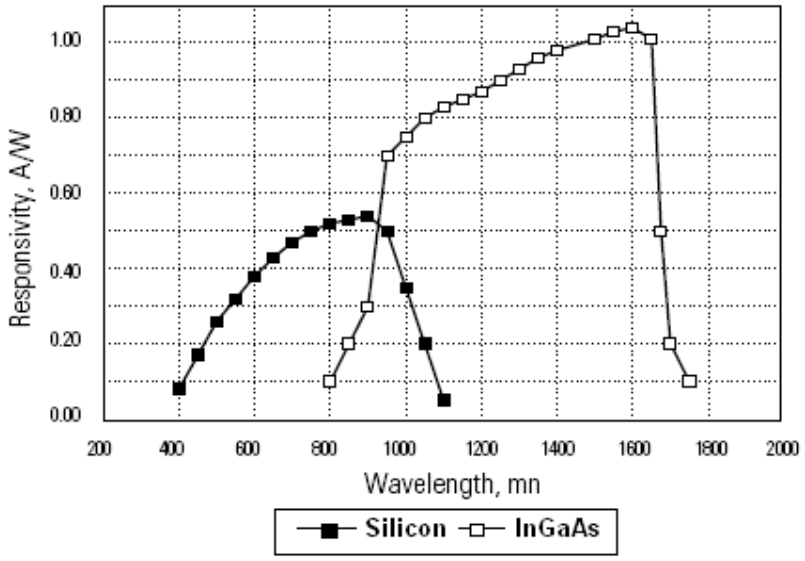

Figure 2.1: Typical photodiode responsivity [77]

Different kinds of photodiodes are sensitive to different ranges of optical wavelengths. For 600-1000 nm wavelength range, silicon photodiodes offer good conversion of photons into electrons. For 1000-1600 nm wavelength range, InGaAs photodiodes have good conversion efficiency. The photodiode responsivity is shown in Figure 2.1. Photodiodes can convert the

optical light energy into the electronic signal and will significantly impact the imaging performance of the OCT system.

2.1.2 Dual-balanced detection

Dual-balanced detection is a commonly used method to recover signals with increased signal-to-noise in the OCT system. This detection method can achieve better noise performance and sensitivity than a photodiode. Laser noise or "common mode noise" can be cancelled and small signal fluctuations on a large DC signal can be detected.

Newfocus Nirvana Model 2007 auto-balanced photodiodes has been used in our system. It consists of two photodiodes (one for the signal arm and the other for the reference arm), a current splitter, a current subtraction node, a transimpedance amplifier, and a feedback amplifier [77]. It can reduce laser noise by more than 50 dB at frequencies from DC to 125 kHz in either simple balanced mode, or by utilizing the auto-balancing circuit. The circuit uses a low-frequency feedback loop to maintain automatic DC balance between the signal and reference arms. The transimpedance amplifier is used to amplify and convert the current into a corresponding electronic voltage.

2.1.3 Analog to digital (A/D) conversion

To acquire the electronic voltage output from auto-balanced photodiodes, a high-speed National Instruments A/D data acquisition card (DAQ) is employed. It can transform the continuous voltage values into discrete digital numbers that can be processed by the control system. The DAQ card has two primary functions: (1) Magnitude quantization of the signal. (2) Sampling of the time-domain signal.

Magnitude quantization means conversion of an analog voltage value to a digital number.

Auto-balanced photodiodes typically provide continuous voltage values between 0-10 V. When this analog voltage value is converted to a digital number by the DAQ card, the resolution is limited by discrete steps. Usually the resolution of an A/D conversion is expressed in bits; the more bits, the finer the resolution. The number of bits determines the number of steps to approximate an analog input voltage. For example, 8-bit resolution of a 0-10 V input voltage means that the conversion steps equal to 2^8=256. 10-V input voltage corresponds to the digital number 255 and 0-V input voltage corresponds to 0. The conversion step size can be calculated as 10 V/256 = 0.039 V. The 0.039 V change in the input voltage will add or subtract 1 from the previous number. This signal magnitude quantization method unavoidably loses some information.

Continuous signal data is also quantized by the DAQ card in terms of time. Sampling rate of the DAQ card is an important parameter and can be set according to the clock frequency of PC system. The Nyquist theorem states that an analog signal may be uniquely reconstructed from samples taken at equal time intervals. The sampling rate must be equal to, or greater than, twice the highest frequency component in the analog signal. In practice, a higher sampling rate should be taken in order to recover the original signal better. Sampling at a lower frequency and ignoring the Nyquist criteria would result in aliasing of the original signal and missing of high frequency information. Once it happens, it is not possible to recover the original signal without error.

2.2 Band-pass filtering

As the reference path is scanned through one period, the interferometric signal voltage output from auto-balanced photodiodes is sampled and acquired by the DAQ card synchronously. Some unwanted noise, such as DC noise, thermal noise, irrelevant frequency noise, etc. will mix into the interferometric signal. It is often desirable to perform electronic filtering on the signal to remove

noise and obtain useful parts of the signal, such as the components mixing within a certain frequency range. A band-pass filter can realize this function.

There are two kinds of band-pass filters; analog and digital. An analog filter uses analog electronic circuits made up from components such as resistors and capacitors to produce the necessary filtering effect. It processes fast and can be realized easily. But it is not stable and sensitive to temperature variations. Typical band-pass electronic filters include Active Sallen and Key Cascade filter, Butterworth filter, etc..

A digital filter uses a digital processor to perform numerical calculations on sampled values of the signal. It is versatile, easily designed on PC system and extremely stable with respect to time and temperature. FFT converts time-domain signal into frequency domain information, and certain frequency range information will be reserved. Different window functions can be used to filter them, and reverse transform them into time domain signal. This enables us to recover the interferometric signal while at the same time suppress noise. Typical window functions include Rectangle window, Hanning window, Hamming window, etc..

In an OCT system, the carrier frequency of the electrical signal $\tilde{f}_0$, often referred to as the Doppler frequency, can be determined by optical centre wavelength l_0 of the light source and the velocity v_s at which the reference path is scanned. Assuming free space propagation,

$$\tilde{f}_0 = \frac{2v_s}{l_0} \tag{2.1}$$

The carrier frequency is important for determining an appropriate sampling rate for the A/D conversion. At present, our OCT system can achieve 53 A-scans/second. The OCT signal has a carrier frequency of about 40 KHz. 1 mega samples/sec acquisition rate is enough to recover the ideal signal.

With a broadband source, the frequency range becomes,

$$\Delta\tilde{f} = \frac{2v_s}{v_g}\Delta f \approx \frac{2v_s}{v_g}(\frac{c}{l_0^2})\Delta l \approx \frac{2v_s}{l_0^2}\Delta l \tag{2.2}$$

where v_g is the optical group velocity. In free space, $v_g = c$, c is the velocity of light.

So the bandwidth of the electrical signal can be given as,

$$\Delta\tilde{f} \approx \frac{\Delta l}{l_0} \cdot \tilde{f}_0 \tag{2.3}$$

In general, the bandwidth (BW) of an electronic filter is larger than the signal bandwidth $\Delta\tilde{f}$. Its range can be written as,

$$\Delta\tilde{f} \le BW \le 2 * \tilde{f}_0 \tag{2.4}$$

However, too large a bandwidth introduces excessive noise into the signal while too small a bandwidth results in a partial loss of the signal. So a rough estimate of bandwidth for the electronic filter is important for an OCT system. Some simulation experiments have been performed to evaluate it.

2.2.1 Simulation of interferometric signal

Assuming one glass with two surfaces as the sample, the relative distribution of reflectivity is shown in Figure 2.3. There are two obvious optical reflectivity coefficients on the glass sample surface. So the intensities of reflected light from these two surfaces are strong and interferometric signal will be obvious and easily detected.

Assuming the light source has a Gaussian spectral shape, a time-domain interferometric signal can be simulated as shown in Figure 2.3 when a small DC offset and 5% noise was added into the signal. Its corresponding FFT is shown in Figure 2.4.

2.2.2 Bandwidth of electronic filter

In an OCT system, different degrees of noise mix into the interferometric signal, so an

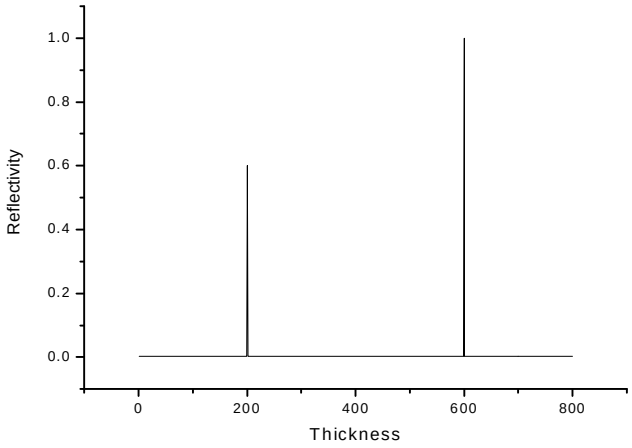

Figure 2.2: Reflectivity of glass sample

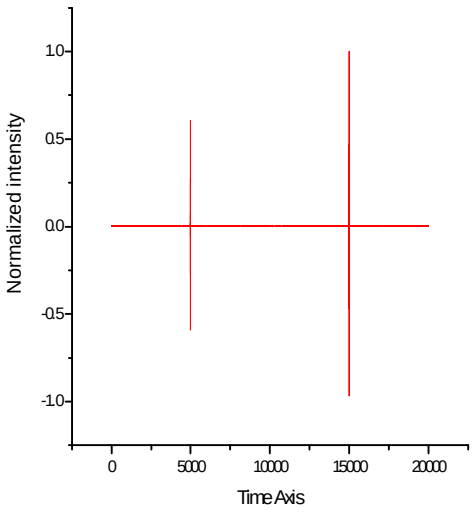

Figure 2.3: Interferometric signal

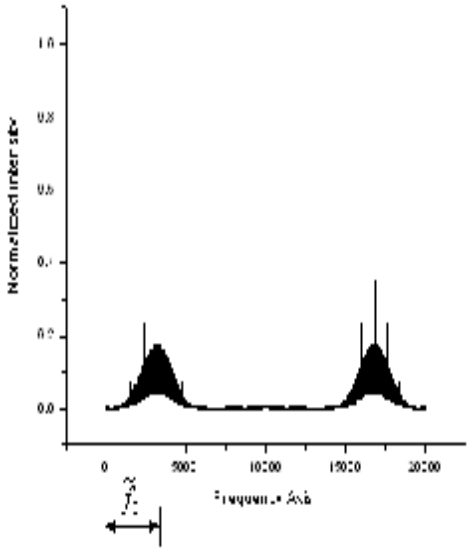

Figure 2.4: Frequency domain of interferometric signal

efficient design of band-pass electronic filter is important. Bandwidth of the filter is an important design parameter. Different bandwidths of the filter will have different filtering effects on the signal.

In designing the filter, we investigated the relationship between bandwidth of the filter and recovery effect of the interferometric signal. The interferometric signal was produced using the

numerical simulation method. In addition, the effects of different window functions on recovery of the interferometric signal were studied. Typical window functions used include Rectangle window, Gaussian window, Hanning window, Hamming window, etc.. Their shapes are shown in Figure 2.5. Simulation results are shown in Figures 2.6 and 2.7. It can be seen that window function can depress the noise in the signal, but degrades the resolution and amplitude of the signal.

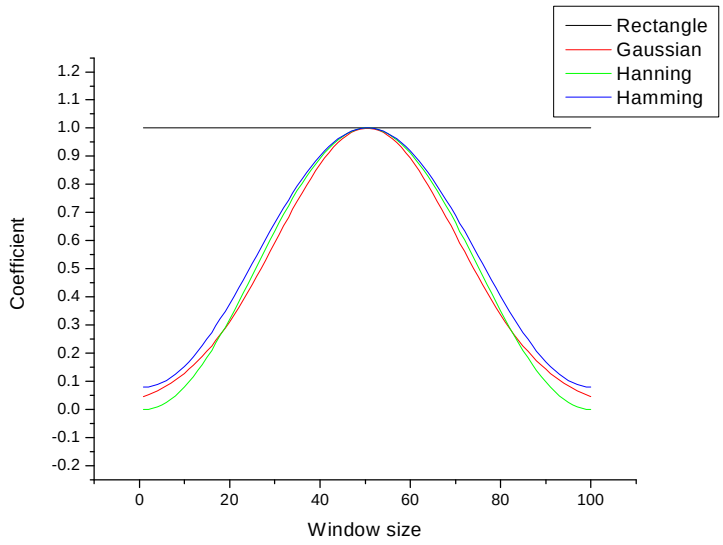

Figure 2.5: Typical window functions

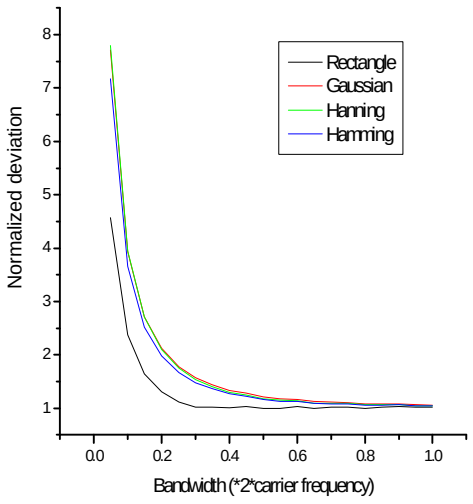

Figure 2.6: Deviation of interferometric signal

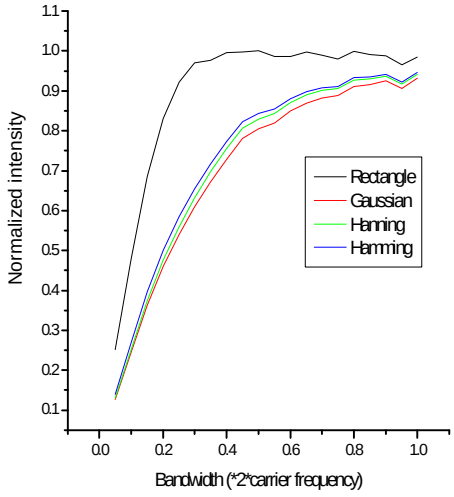

Figure 2.7: Amplitude of interferometric signal

In addition, simulation results show that in order to recover the signal efficiently and depress the noise, the bandwidth of the electronic filter should be set as

$$BW \approx 0.5\tilde{f}_0 \tag{2.5}$$

2.3 Envelope detection technology

For the intensity-based OCT system, only the intensity of the demodulated interferometer output is acquired and analyzed. The envelope is the overall shape of the amplitude maximae of the signal [78]. Therefore, it is important to extract the envelope of the interferometric signal to form the final OCT image, accurately extracted envelope can be used to form a high-resolution OCT image. Currently, the ideal envelope detection methods include Fast Fourier Transform method and Hilbert Transform method.

2.3.1 Interferometric signal

If a Gaussian input spectrum is used for the power spectral density, given by

$$S(w) = \sqrt{\frac{2p}{s_w^2}} e^{-\frac{(w-w_0)}{s_w^2}} \tag{2.6}$$

where w is the angular frequency of the light source, w_0 is the center frequency of the light source and s_w is the spectral bandwidth.

Then optical intensity at the detector (refer to appendix A) can be calculated as

$$I_D = real\left\{\frac{1}{2p} e^{-iw_0\Delta t_p} \int_{-\infty}^{\infty} \sqrt{\frac{2p}{s_w^2}} e^{-\frac{(w-w_0)^2}{s_w^2}} e^{-i\Delta t_g (w-w_0)} dw\right\} \tag{2.7}$$

where Δt_p is the phase delay, Δt_g is the group delay.

According to an integral identity

$$\int_{-\infty}^{\infty} e^{2bx-ax^2} = \sqrt{\frac{p}{a}} e^{\frac{b^2}{a}} \tag{2.8}$$

where a and b are the fixed parameters, x is a variable.

Equation (2.7) can be solved as

$$I_D = real\left\{ e^{-iw_0 \Delta t_p} e^{-\frac{1}{2}\Delta t_g^2 s_w^2} \right\} \tag{2.9}$$

Considering that the spectral bandwidth is inversely proportional to the pulse duration s_t,

$$s_w = \frac{1}{s_t} \tag{2.10}$$

Then equation (2.9) can be written as

$$I_D = real\left\{ e^{-iw_0 \Delta t_p} e^{-\frac{\Delta t_g^2}{2 s_t^2}} \right\} \tag{2.11}$$

2.3.2 Fast Fourier Transform method

According to equation (2.11), it can be known that the detected interferometric signal has the form

$$g(t) = a(t) + b(t)\sin(wt + f)$$

$$= a(t) + c(t)e^{iwt} + c^*(t)e^{-iwt} \tag{2.12}$$

With $$c(t) = \frac{1}{2} b(t) e^{if} \tag{2.13}$$

where * denotes a complex conjugate, $b(t)$ is the message signal of interest, $\sin(wt + f)$ is a carrier with time-varying frequency and phase, and t is the time variable.

Equation (2.12) can be transformed using Fast Fourier Transform (FFT) algorithm, which gives,

$$G(f) = A(f) + C(f - f_0) + C^*(f - f_0) \tag{2.14}$$

We can make use of either of the two spectra on the carrier and translate it by f_0 on the frequency axis toward the origin to obtain $C(f)$, then use inverse Fast Fourier Transform for

$C(f)$ to obtain $c(t)$. Envelope information $b(t)$ can be obtained using equation (2.13) [79].

2.3.3 Hilbert Transform method

The Hilbert Transform provides a 90^0 phase shift to its input signal regardless of the original phase. If $g(t)$ is the real input signal, and the Hilbert transformed signal is $h(t)$, then the analytic signal $z(t)$ is given by

$$z(t) = g(t) + ih(t) \tag{2.15}$$

where
$$h(t) = \frac{1}{p} P\int_{-\infty}^{\infty} \frac{g(t)}{t-t} dt \tag{2.16}$$

Considering the interferometric signal as

$$\begin{aligned} g(t) &= A(t)\cos(wt) \\ &= \frac{A(t)}{2}(e^{jwt} + e^{-jwt}) \end{aligned} \tag{2.17}$$

and applying the $\pm p/2$ phase shifts, the Hilbert Transform is

$$\begin{aligned} h(t) &= \frac{A(t)}{2}(e^{jwt-jp/2} + e^{-jwt+jp/2}) \\ &= \frac{A(t)}{2}(-je^{jwt} + je^{-jwt}) \\ &= A(t)\sin(wt) \end{aligned} \tag{2.18}$$

Then the analytic signal is

$$z(t) = A(t)(\cos(wt) + \sin(wt)) = A(t)e^{jwt} \tag{2.19}$$

The signal envelope is just the magnitude of the analytic signal [63]:

$$A(t) = |z(t)| \tag{2.20}$$

2.3.4 Simulation results of envelope detection

Assuming that the incident light source has a Gaussian spectrum, the interferometric signal would have the form derived in equation (2.11). We can then use equation (2.21) to simulate the interferometric signal data, which can be analyzed using Fast Fourier Transform and Hilbert

Transform methods. According to equation (2.11), the interferometric signal can be written as

$$g(t) = a + b * e^{-\frac{(t-c)^2}{d^2}} * \sin(w * t + f) + n(t) \qquad (2.21)$$

where a is the offset, b is the amplitude of the signal, c is the centre of the envelope, d is the deviation, $\sin(w * t + f)$ is the carrier, w is the angular frequency, f is the initial phase, $n(t)$ is the random noise.

We used equation (2.21) to simulate interferometric signals. Different degrees of noise were added, then Fast Fourier Transform (FFT) and Hilbert Transform (HT) methods were used to extract the envelope. Figures 2.8, 2.9, 2.10 are the results using FFT method. The black line repre

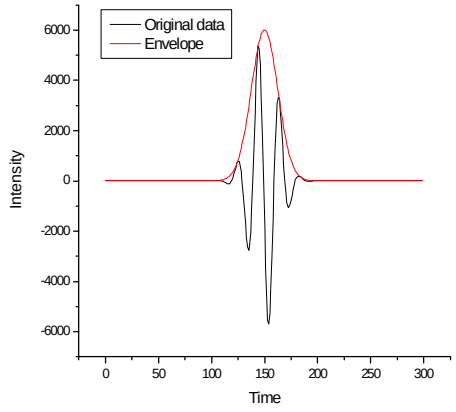

Figure 2.8: Envelope extracted using FFT without noise

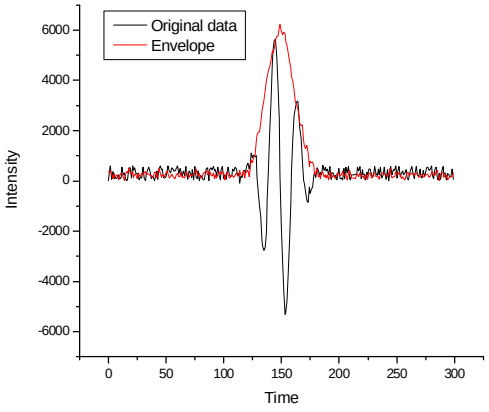

Figure 2.9: Envelope extracted using FFT with 5% noise

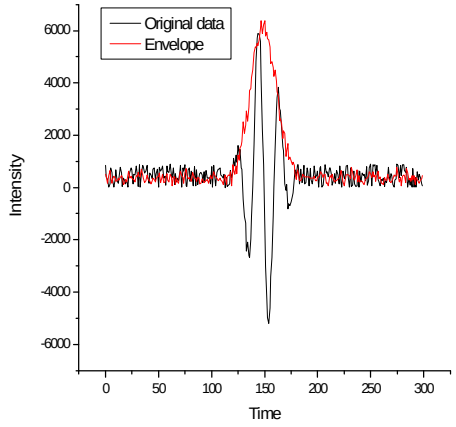

Figure 2.10: Envelope extracted using FFT with 10% noise

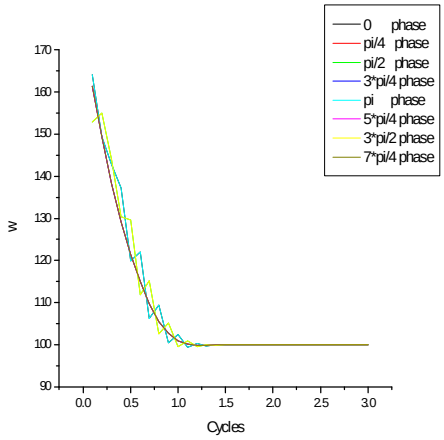

Figure 2.11: Deviation d without noise

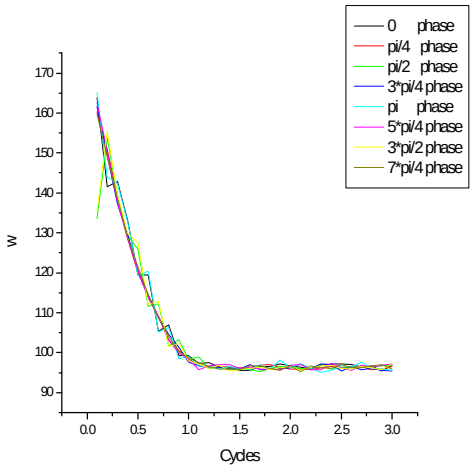

Figure 2.12: Deviation d with 5% noise

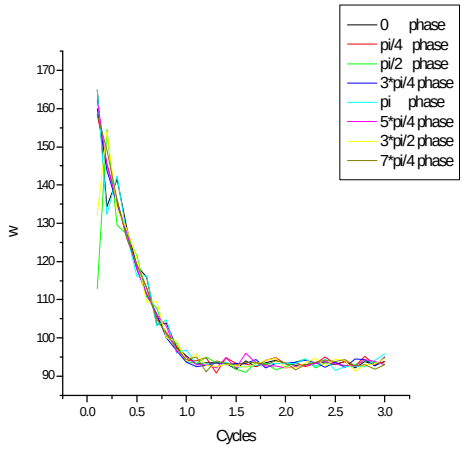

Figure 2.13: Deviation d with 10% noise

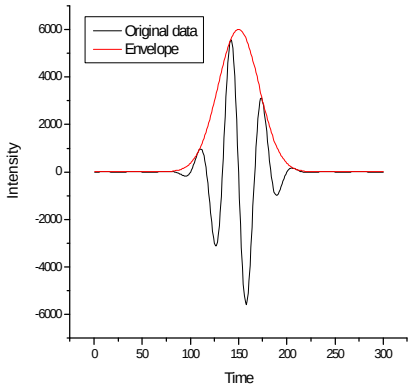

Figure 2.14: Envelope extracted using HT without noise

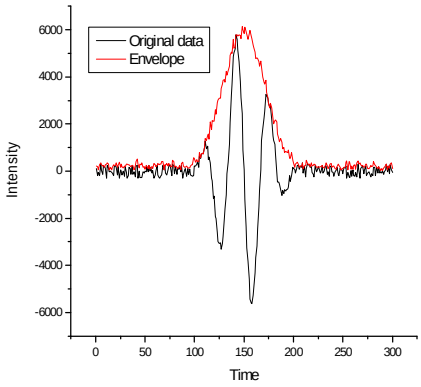

Figure 2.15: Envelope extracted using HT with 5% noise

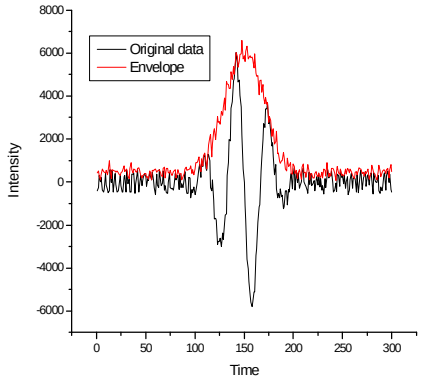

Figure 2.16: Envelope extracted using HT with 10% noise

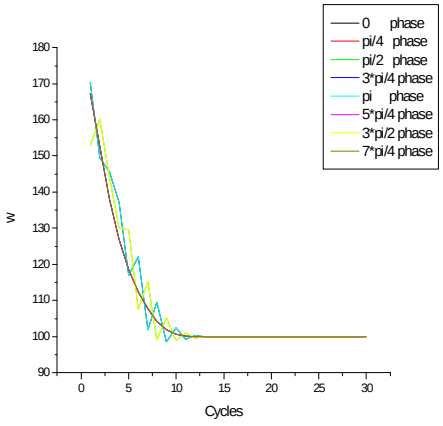

Figure 2.17: Parameter d without noise

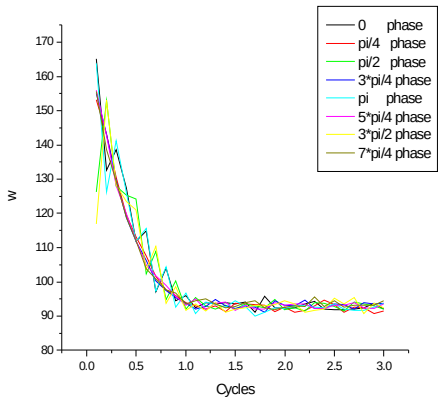

Figure 2.18: Parameter d with 5% noise

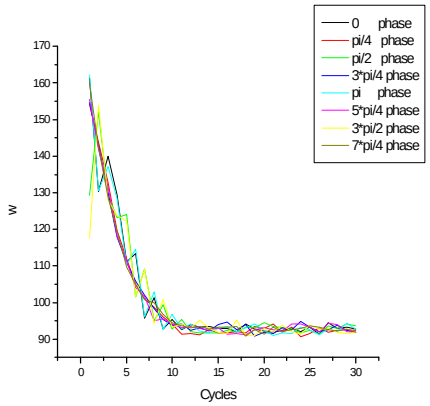

Figure 2.19: Parameter d with 10% noise

-sents the interferometric signal while the red line represents the envelope that has been extracted. Simulation shows that FFT method can achieve near-perfect result for the typical interferometric signal with different degrees of noise.

Curve fitting method has been employed to analyze the extracted envelope and the effects of FFT method have been evaluated. Equation (2.21) was used as initial curve, with some initial parameter values, to fit the envelope that has been extracted. Parameter d was an important fitted parameter and used to estimate the effect of FFT method. According to the FWHM criteria, the resolution should be $2\ln 2 * d$. Therefore fitted parameter d can give direct indication of the effect of envelope detection.

The effect of FFT on envelope detection has been evaluated using different interferometric signals with (1) Different carrier frequency, which determines the numbers of oscillations within the envelope, (2) Different initial phase of the carrier. In addition, different degrees of random noise have been added into the original signals.

Figures 2.11, 2.12, 2.13 are the simulation results using FFT method and have been evaluated

by the curve fitting method. The x-axis shows how many oscillations there are inside the envelope, while the y-axis shows the results of fitted parameter d. Different initial phases of the carrier (0, $p/4$, $p/2$, $3p/4$, p, $5p/4$, $3p/2$, $7p/4$) have been used to generate the interferometric signal. From these figures, it can be seen that the curves are sharp before 1.5 oscillations and d decreases very obviously with the increase of the numbers of the oscillations. This means that FFT method does not recover the envelope well when there are less than 1.5 oscillations inside the envelope of the interferometric signal. In this case, the extracted envelope was degraded using FFT method. However, the curves inside these figures become flat and d is stable after 1.5 oscillations. This means that the envelope has been extracted accurately using FFT method. Therefore, 1.5 oscillations inside the e^{-1} envelope will be enough for FFT method to extract the envelope. In addition, the effectiveness of FFT method is hardly affected by the initial phases of the interferometric signal.

Similarly, the HT method has also been tested. Figures 2.14, 2.15, 2.16 are the results using HT method. The red line represents the envelope that has been extracted. Figures 2.17, 2.18, 2.19 show that 1.5 oscillations inside the e^{-1} envelope will be enough for HT method to extract the envelope of the interferometric signal.

2.3.5 Some comparison between FFT method and HT method

From above simulation results, it is seen that FFT method and HT method both are ideal envelope detection algorithms which can achieve near-perfect results.

We further compare their detection effects on the signal data under different acquisition speeds. Figures 2.20, 2.21 are some examples of the simulation data. For the interferometric signal which has about 1.5 oscillations inside the envelope, different acquisition speeds are used to

sample the signal. The acquired data is then analyzed separately using FFT and HT methods. The results are shown in Figure 2.22 and Figure 2.23. It can be seen that under slower acquisition speeds (less than 25 data points/cycle), HT method shows more accurate results on envelope detection of interferometric signal. However under higher acquisition speed, FFT and HT achieve nearly the same results.

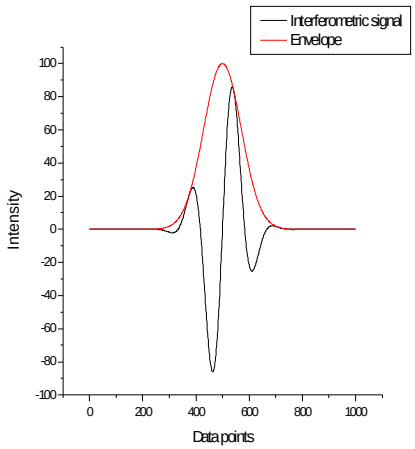

Figure 2.20: 100 data points/cycle

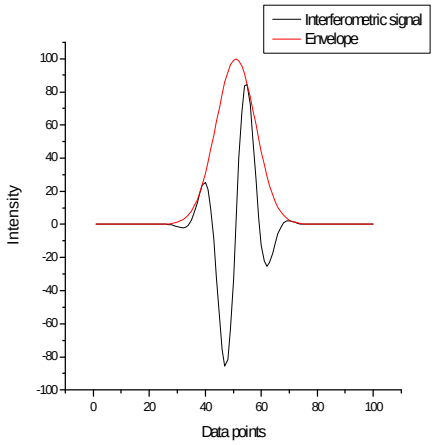

Figure 2.21: 10 data points/cycle

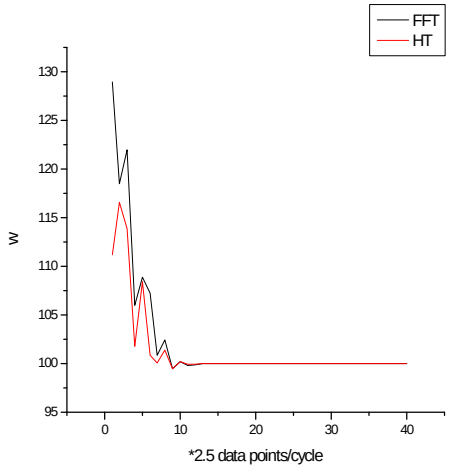

Figure 2.22: Parameter d under different acquisition speed

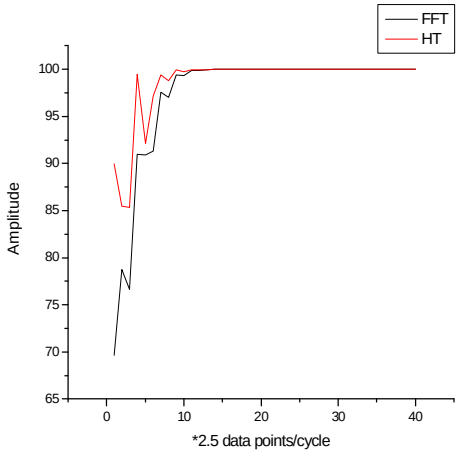

Figure 2.23: Amplitude under different acquisition speed

Since FFT method is faster than HT method, it has been used for data processing in our system.

2.4 OCT image formation

After the envelope of the interferometric signal of each A-scan is extracted from the raw data acquired by the DAQ card, it can be transformed to image scale value and an OCT image is formed.

Quantization is an important step in OCT image formation; it will map real values of the envelope data to a series of fixed gray levels taking values, viz. [1,…,256]. The raw envelope data

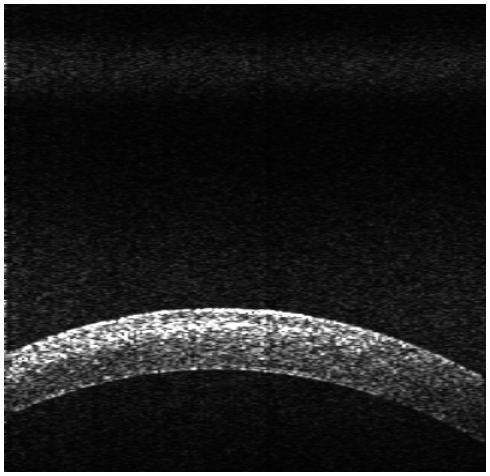

Figure 2.24: Cornea

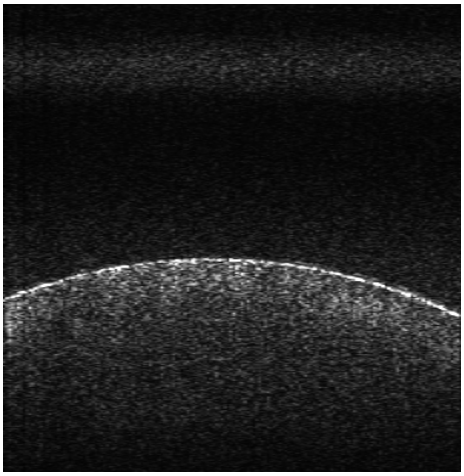

Figure 2.25: Anterior lens

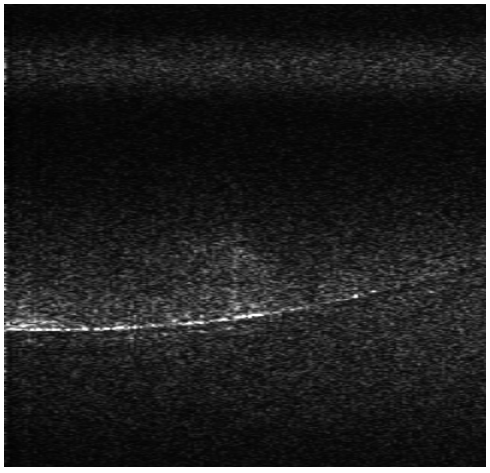

Figure 2.26: Posterior lens

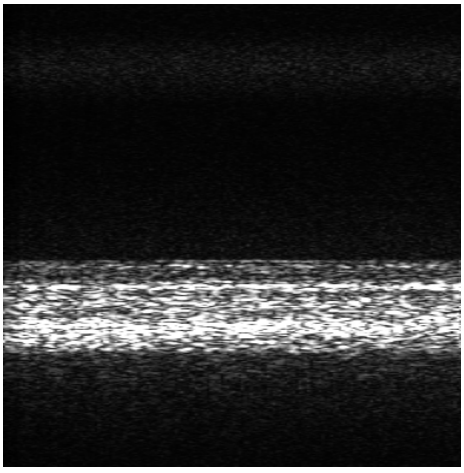

Figure 2.27: Retina

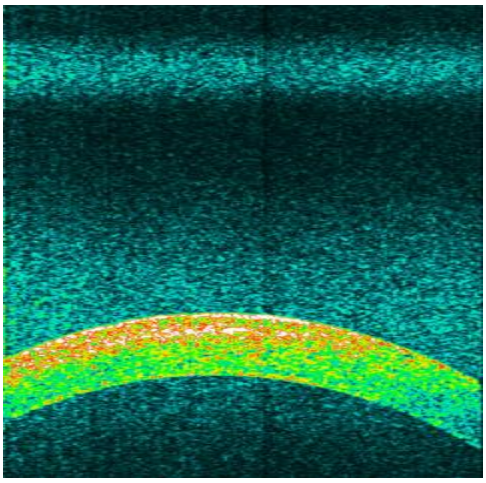

Figure 2.28: Pseudo-color cornea

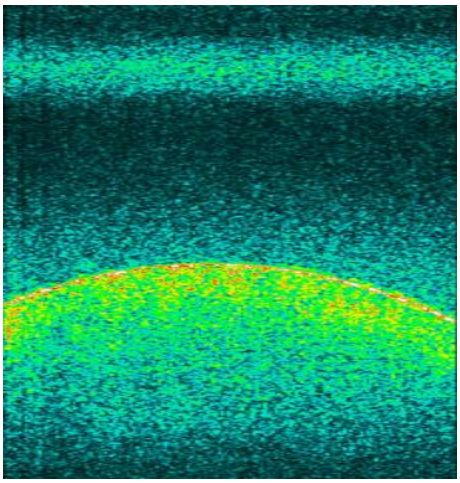

Figure 2.29: Pseudo-color anterior lens

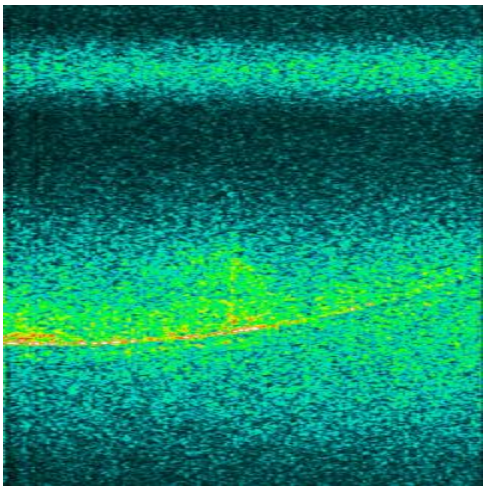

Figure 2.30: Pseudo-color posterior lens

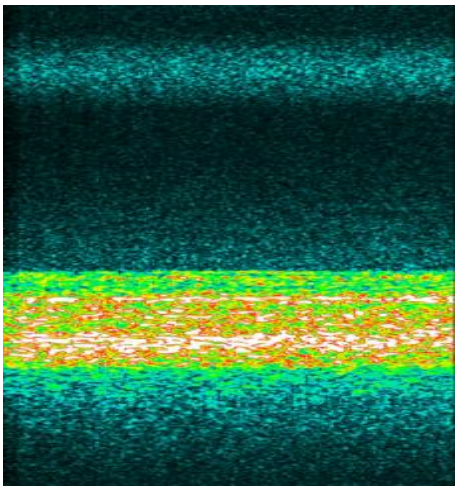

Figure 2.31: Pseudo-color retina

usually has a different distribution from that of the image gray levels, and thus real values can not be displayed on PC screen directly. Therefore, it is necessary to quantize the raw envelope data, using scalar quantization.

In digital image processing, commonly used quantization methods include equal-interval, equal-probability, minimum-variance and histogram hyperbolization, etc.. In addition, logarithm-based methods are commonly used in OCT image formation [80]. We used

equal-interval quantization method to form final gray-level OCT image. Figures 2.24-2.27 are OCT images of the structures of the rabbit eye.

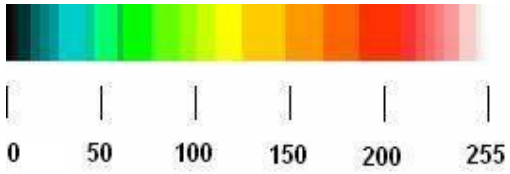

Figure 2.32: Colormap setting

Pseudo-color OCT images, as shown in Figures 2.28-2.31, have been generated from gray-level OCT images using Colormap setting as shown in Figure 2.32.

2.5 Conclusions

The electronic signal detection method has been discussed in this chapter. Numerical simulation methods were employed to find suitable bandwidth for band-pass filtering. About 0.5*carrier frequency bandwidth will efficiently recover the signal and depress the noise in the signal.

The basic formulation of interferometric signal of time-domain OCT has been derived. Different envelope detection technologies, such as FFT method and HT method, have been tested on the interferometric signal of time-domain OCT system. Simulation results show near-perfect envelope detection effects. However, either FFT or HT method does not extract the envelope well if too small oscillations are inside the envelope of the interferometric signal. About 1.5 oscillations inside the envelope will be enough for extracting the envelope using FFT or HT method.

Current OCT image formation methods were simply described.

Chapter 3 Design of Fourier domain optical delay line (FD_ODL)

3.1 Design of FD_ODL

3.1.1 Basic theory of FD_ODL

In order to acquire images quickly, a high speed scanning optical delay line is necessary for the time-domain OCT system. For example, an image consisting of 160 A-scans to be acquired in 3 seconds requires that the optical delay line must be scanned at 160/3 A-scans per second. In addition, the optical delay line should be designed long enough to have a useful imaging scanning depth in biological samples.

Different designs for optical delay lines have been reported in recent years. Early optical delay lines used a flat mirror mounted on linear translation stage which is driven by a dc motor or voice coil, shown in Figure 3.1 (a) [4]. But it usually results in slow repetition rates of about 30 HZ. The scanning speed of a translating retroreflector can be improved by a few times using piezoelectric transducer to drive one of the two parallel mirrors and allow the reference light to make multiple passes between parallel mirrors, shown in Figure 3.1 (b) [81].

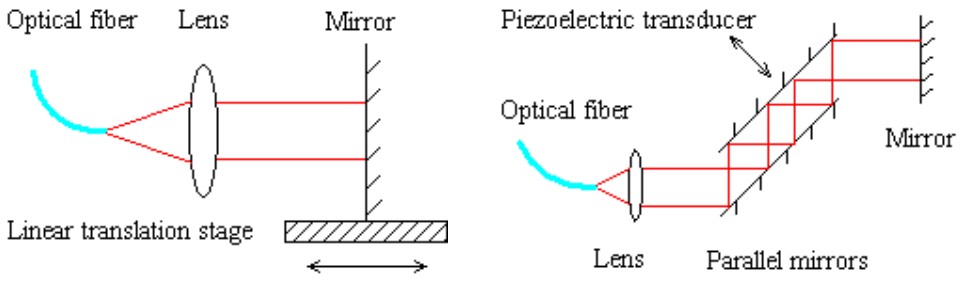

Figure 3.1: (a) Linear translating retroreflector (b) Piezo-actuated multipass translating retroreflector

Rotational motion-based methods are proposed to vary optical path-length of the reference arm. The light beam traverses through a rotating glass cube at constant speed, the optical delay will be generated at high repetition rate, shown in Figure 3.2 (a) [82]. An optical delay line based on rotary mirror array was designed as shown in Figure 3.2 (b) [83, 84]. The facets of the mirrors are tilted at a small angle. When the mirror array moves at a constant speed, the periodical optical delay will be generated with high speed.

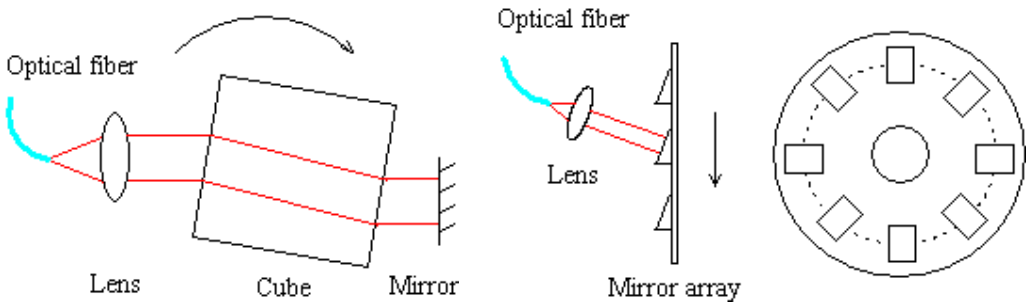

Figure 3.2: (a) Optical delay line with rotating cube (b) Optical delay line with rotary mirror array

Fibre stretching around cylindrical piezoelectric transducer that modify the path-length of the reference arm has been used for optical delay line, shown in Figure 3.3 [85], but it is limited by polarization mode dispersion, hysteresis, usually very high voltages and poor temperature stability.

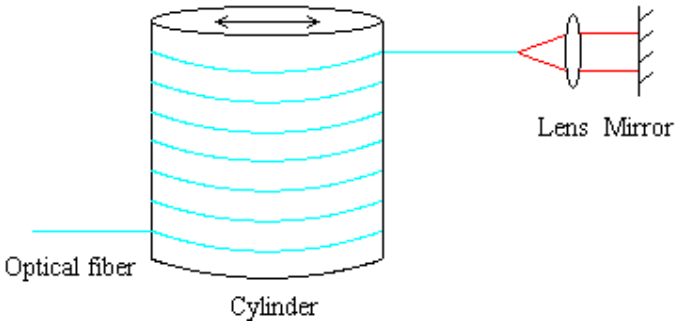

Figure 3.3: Optical delay line based on optical fibre stretching

Recently FD_ODL, which was developed from femtosecond pulse-shaping technology, has

been reported to be used successfully into OCT system. This optical delay line can achieve several millimeters depth at repetition rates of at least several tens hertz [86-94]. In this project, we used this high speed FD_ODL, which consists of diffraction grating, doublet achromatic lens, rapid scanning mirror, double-pass mirror, etc.. The main advantages of FD_ODL include: (1) It can provide 10-100 times faster scan velocity and scan repetition rate than conventional translational scanner as shown in Figure 3.1 (a). (2) It is more stable compared to other methods. Small angular mirror rotation (about 5-10 degrees) can achieve depth scans of a few millimeters without moving parts. So it will be hardly affected by the hysteresis. (3) The group delay is independent from the phase delay, and the center frequency and bandwidth of the OCT signal can be controlled in FD_ODL. (4) The group velocity dispersion between the two arms of the OCT system could be tuned by displacing the diffraction grating from the focal plane of the lens, without using an additional prism like other optical delay lines. But in this design, the light is diffracted into the first order at the diffraction grating; the optical power loss will be significantly greater than other optical delay lines.

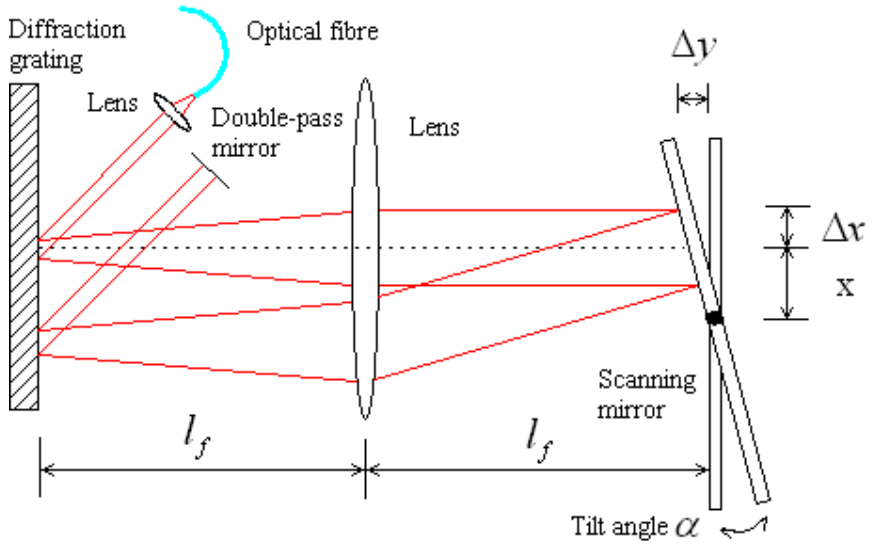

Figure 3.4: Schematic of fourier-domain optical delay line [89]

The basic configuration of FD_ODL is shown in Figure 3.4. It can be seen that the incoming light will go to the diffraction grating and be spectrally dispersed by it. The dispersed spectrum is then focused on the rapid scanning mirror. The reflected light from the scanning mirror will be reconverged onto the grating by the lens, and then be diffracted towards the double-pass mirror. The double-pass mirror will return and re-couple the light into the OCT system.

The general grating equation can be written as

$$n\,l = p(\sin(q) + \sin(q')) \tag{3.1}$$

where n is the order of diffraction, l is the diffracted wavelength, p is the grating constant (the distance between grooves), q is the angle of incidence measured from the normal and q' is the angle of diffraction measured from the normal.

Assuming that the first order diffraction of centre wavelength light l_0 is perpendicular to the diffraction grating, i.e. $n = 1,\ q' = 0$,

$$l_0 = p\sin(q) \tag{3.2}$$

Then the diffraction angle of the spectrum can be calculated as

$$\Delta q = \arcsin(\frac{l - l_0}{p}) \approx \frac{l - l_0}{p} = \frac{\Delta l}{2p} \tag{3.3}$$

The spectrum will be displaced a distance along the lateral direction, given by

$$\Delta x = l_f tg(\Delta q) \approx l_f \Delta q \tag{3.4}$$

When the wavelength component l traverses as a function of scanning mirror tilt angle s, the caused distance Δd is

$$\Delta d = tg(s)(x + \Delta x) \approx s\,(x + \Delta x) \tag{3.5}$$

where x is the distance offset of the center wavelength component from the morror pivot.

As the light pass through the distance Δd four times due to the double pass configuration

of this optical delay line, the phase shift $f(l)$ as a function of wavelength l is written as [89]

$$f(l) = \frac{2p}{l} \cdot 4 \cdot \Delta d = \frac{8ps}{l}(x + \Delta x)$$

$$= \frac{8psx}{l} + \frac{8psl_f(l - l_0)}{pl} \tag{3.6}$$

w and l can be related by

$$w = \frac{2p}{l/c} \tag{3.7}$$

Finally the phase shift is obtained as a function of angular optical frequency w [89],

$$f(w) = \frac{4sxw}{c} - \frac{8psl_f(w - w_0)}{pw} \tag{3.8}$$

From the definition of phase delay, $t_p = f(w_0)/w_0$, the phase delay is calculated as [89]

$$t_p = \frac{4sx}{c} \tag{3.9}$$

which corresponds to the free space phase pathlength difference Δl_p [89],

$$\Delta l_p = 4sx \tag{3.10}$$

From the definition of group delay, $t_g = \partial f(w)/\partial w\Big|_{w=w_0}$, the group delay is given by [89],

$$t_g = \frac{4sx}{c} - \frac{4sl_f l_0}{cp} \tag{3.11}$$

which corresponds to the free space group pathlength difference Δl_g [89],

$$\Delta l_g = 4sx - \frac{4sl_f l_0}{p} \tag{3.12}$$

3.1.2 Relationship between phase delay and group delay

According to the simulation results in chapter 2, 1.5 oscillations contained within e^{-1} full width of the envelope is enough to extract the envelope accurately. This means phase delay Δt_p can be given as

$$\Delta t_p = \frac{l_0}{c} \cdot s \tag{3.13}$$

where c is the velocity of light, s is the number of oscillations inside the envelope

$$s = 1.5 \tag{3.14}$$

It is known that group delay can be given as

$$\Delta t_g = 2\sqrt{2} s_t \tag{3.15}$$

In free space, the full-width half-maximum spectral bandwidth is given by

$$\Delta w_{FWHM} = 2\sqrt{2\ln 2} s_w \tag{3.16}$$

In addition,

$$\Delta w = dw = d(2pc / l) = \frac{2pc}{l_0^2} \Delta l \tag{3.17}$$

From equation (3.16) and (3.17), we can get

$$s_w = \frac{pc}{\sqrt{2\ln 2} l_0^2} \Delta l \tag{3.18}$$

Group delay can be rewritten as

$$\Delta t_g = 2\sqrt{2} / s_w = \frac{4\sqrt{\ln 2} l_0^2}{pc\Delta l} \tag{3.19}$$

So the relationship between phase delay and group delay can be described as

$$\frac{\Delta t_g}{\Delta t_p} = \frac{4\sqrt{\ln 2} l_0}{ps\Delta l} \approx \frac{5.3}{s} \tag{3.20}$$

3.1.3 Computation of key parameters of FD_ODL

According to the basic theory of FD_ODL, group delay and phase delay can be related by the following equation,

$$\frac{\left|\Delta l_g\right|}{\left|\Delta l_p\right|} = \frac{\left|\Delta t_g\right|}{\left|\Delta t_p\right|} \tag{3.21}$$

From equations (3.10), (3.12), (3.20), as well as (3.21), the equation below can be obtained,

$$\frac{|\Delta l_g|}{|\Delta l_p|} = \frac{5.3}{s} \tag{3.22}$$

$$\frac{4s l_f l_0 / p}{4sx} = \frac{l_f l_0}{px} = \frac{5.3}{s} + 1 \tag{3.23}$$

$$x = \frac{l_f l_0}{(\frac{5.3}{s} + 1)p} \tag{3.24}$$

In practical OCT system, the oscillations s inside the envelope can be carefully adjusted by the offset x according to equation (3.24). Assuming that the groove of the diffraction gratings is 600 lines/mm (p = 1/600 mm), their relationship can be rewritten as,

$$s = \frac{5.3}{\frac{0.48 \cdot l_f}{x} - 1} \tag{3.25}$$

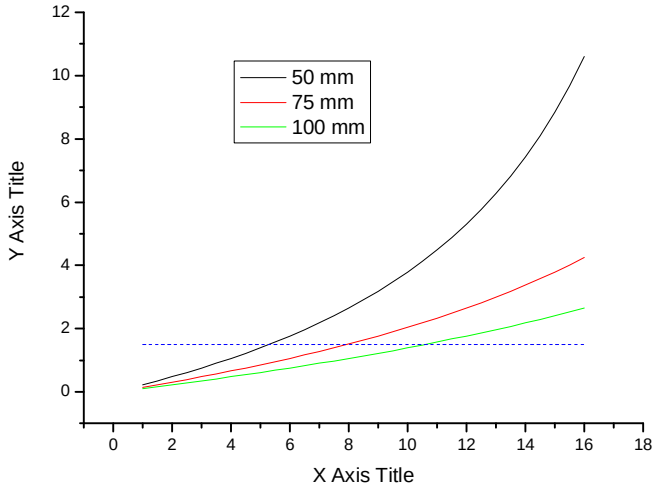

Figure 3.5: Oscillations s versus offset x for different focal lengths 50mm, 75mm and 100mm

For different focal lengths, the relationship between the oscillations s and the offset x is plotted in Figure 3.5. When the offset x is adjusted large, the oscillations s inside the envelope

can be controlled to increase. So the offset x plays an important role in controlling the oscillations s and tuning the shape of the interferometric signal. In order to efficiently extract the envelope of the interferometric signal, the offset x should be set to a suitable value so that s is more than 1.5.

From equations (3.3), (3.4) and (3.24), the mirror size L that confines the laser spot within the mirror is given by equation (3.26), which depends on the focal length l_f of the lens:

$$L \geq 2(x + \Delta x) = 2(\frac{l_0}{(\frac{5.3}{s} + 1)} + \frac{\Delta l}{2}) l_f / p$$

$$\geq 0.96 \cdot (\frac{1}{(\frac{5.3}{s} + 1)} + 0.1) \cdot l_f \qquad (3.26)$$

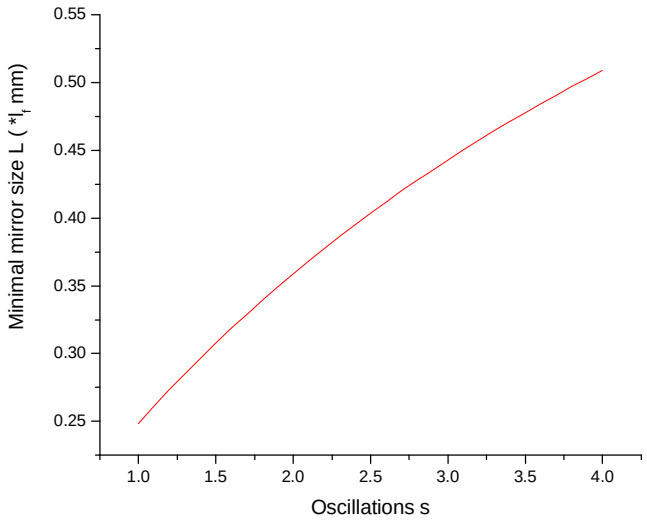

Figure 3.6: Relationship between minimal mirror size L and oscillations s

The relationship between minimal mirror size L and oscillations s is plotted according to equation (3.26) (Figure 3.6). It can be seen that when oscillations s increases, the minimal

mirror size L increases, so the system needs bigger size of the scanning mirror.

In addition, the imaging depth z of the OCT system can be given as

$$z = \frac{\Delta l_g}{2n} = \frac{5.3\Delta l_p}{2sn} = \frac{5.3 \cdot 4sx}{2sn} = \frac{10.6sx}{sn} \tag{3.27}$$

where n is the refractive index of the tissues. We will approximate it as 1.4 in biological tissues, i.e. $n \approx 1.4$.

Then the scanning mirror tilt angle s can be computed as

$$s = \frac{snz}{10.6x} \tag{3.28}$$

We chose some typical focal lengths, then calculated the minimal mirror sizes as well as tilt angles according to derived equations (3.14), (3.26) and (3.28). These data have been listed in table 3.1. They will serve as an important guideline when we set up the FD_ODL for the OCT system.

Table 3.1: Important design parameters of FD_ODL

Focal length l_f (mm)	Minimal mirror size L (mm)	Offset x (mm)	Tilt angle s (degree) ($z = 2mm$)	Tilt angle s (degree) ($z = 4mm$)
45	13.91	4.80	4.8	9.5
50	15.45	5.34	4.3	8.6
60	18.54	6.40	3.6	7.2
75	23.18	8.00	2.9	5.7
100	30.90	10.67	2.1	4.3

According to these calculation results, we have chosen the diffraction grating of 600 lines/mm and a lens of focal length 50 mm. For the high-speed scanning mirror, we have chosen

model 6650 moving coil closed loop galvanometer based optical scanner (Cambridge Technology). These components have been used to set up FD_ODL for our system.

3.2 Geometric ray tracing analysis and optics alignment of FD_ODL

3.2.1 Ray tracing analysis of FD_ODL

The main objective of ray tracing analysis of FD_ODL is to determine the problems caused by dispersion and optical alignment. In addition, it will also help to optimize the lay-out of the optical components in our system.

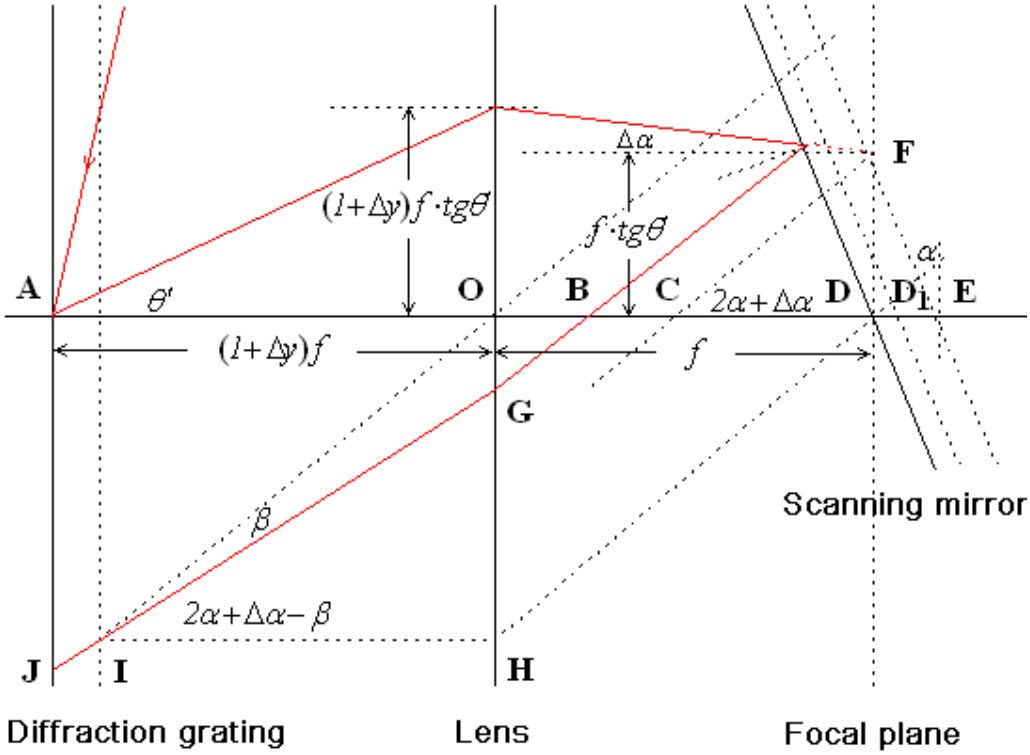

Figure 3.7: Ray tracing analysis of the reference arm

Assume that the optics system has not been aligned well (Figure 3.7), the diffraction grating has not been put in the focal plane, and a little slight displacement $\Delta y \cdot f$ exists, $\overline{AO} = (1+\Delta y) \cdot f$. Then the diffracted light will pass through the lens and be focused onto the

focal plane at point F. A small bending angle Δa can be computed as

$$tg(\Delta a) = \frac{\Delta y \cdot tg(q') \cdot f}{f} = \Delta y \cdot tg(q') \tag{3.29}$$

If the scanning mirror doesn't pass through the focal point D, but goes through the point D_1, then there is a slight displacement $\overline{DD_1} = \Delta z \cdot f$,

$$\overline{D_1 E} = f \cdot (tg(q') \cdot tg(a) - \Delta z) \tag{3.30}$$

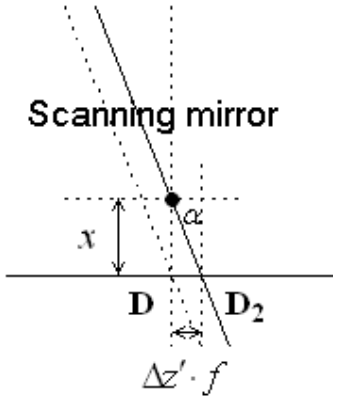

Figure 3.8: The placement position of the scanning mirror

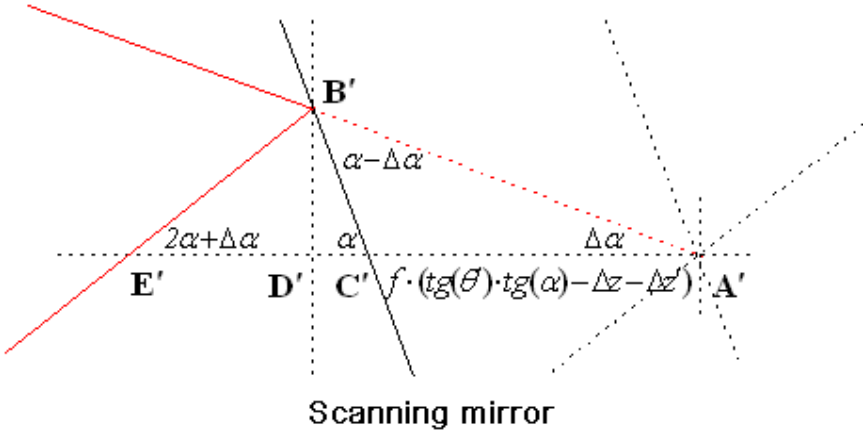

Figure 3.9: Enlarged figure showing the position of incidence light on the scanning mirror

In addition, we should notice that as the centre of the scanning mirror is not located in the optical axis of lens, it will also cause a little slight displacement $\overline{DD_2} = \Delta z' \cdot f$ as shown in Figure 3.8.

$$\Delta z' \cdot f = x \cdot tg(a) \tag{3.31}$$

So $\overline{D_1E}$ can be revised to

$$\overline{D_1E} = f \cdot (tg(q') \cdot tg(a) - \Delta z - \Delta z') \tag{3.32}$$

In Figure 3.9,

$$\overline{A'C'} = \overline{D_1E} = f \cdot (tg(q') \cdot tg(a) - \Delta z - \Delta z') \tag{3.33}$$

In the triangle $\Delta A'B'C'$, we have the following equation:

$$\frac{\overline{A'C'}}{\sin(a - \Delta a)} = \frac{\overline{B'C'}}{\sin(\Delta a)} \tag{3.34}$$

So

$$\overline{B'C'} = \overline{A'C'} \cdot \frac{\sin(\Delta a)}{\sin(a - \Delta a)} \tag{3.35}$$

In the triangle $\Delta B'C'D'$,

$$\overline{B'D'} = \overline{B'C'} \cdot \sin(a) \tag{3.36}$$

$$\overline{C'D'} = \overline{B'C'} \cdot \cos(a) \tag{3.37}$$

In the triangle $\Delta B'D'E'$,

$$\overline{D'E'} = \overline{B'D'} \cdot \frac{\cos(2a + \Delta a)}{\sin(2a + \Delta a)} \tag{3.38}$$

So we can get

$$\overline{A'E'} = \overline{A'C'} + \overline{C'D'} + \overline{D'E'}$$

$$= \overline{A'C'} \cdot (1 + \frac{\sin(\Delta a) \cdot \cos(a)}{\sin(a - \Delta a)} + \frac{\sin(\Delta a) \cdot \sin(a) \cdot \cos(2a + \Delta a)}{\sin(a - \Delta a) \cdot \sin(2a + \Delta a)})$$

$$= (1 + \frac{\sin(\Delta a) \cdot \cos(a)}{\sin(a - \Delta a)} + \frac{\sin(\Delta a) \cdot \sin(a) \cdot \cos(2a + \Delta a)}{\sin(a - \Delta a) \cdot \sin(2a + \Delta a)}) \cdot (tg(q') \cdot tg(a) - \Delta z - \Delta z') \cdot f$$

$$= \frac{\sin(a) \cdot \sin(2a)}{\sin(a - \Delta a) \cdot \sin(2a + \Delta a)} \cdot (tg(q') \cdot tg(a) - \Delta z - \Delta z') \cdot f \tag{3.39}$$

Then

$$\overline{BC} = \overline{A'E'} = \frac{\sin(a)\cdot\sin(2a)}{\sin(a-\Delta a)\cdot\sin(2a+\Delta a)}\cdot(tg(q')\cdot tg(a)-\Delta z-\Delta z')\cdot f \quad (3.40)$$

$$\overline{CD} = (\frac{\cos(2a+\Delta a)}{\sin(2a+\Delta a)})\cdot tg(q')\cdot f \quad (3.41)$$

$$\overline{BD} = \overline{BC} + \overline{CD}$$

$$= (\frac{\sin(a)\cdot\sin(2a)}{\sin(a-\Delta a)\cdot\sin(2a+\Delta a)}\cdot(tg(q')\cdot tg(a)-\Delta z-\Delta z') + (\frac{\cos(2a+\Delta a)}{\sin(2a+\Delta a)})\cdot tg(q'))\cdot f$$

$$= m\cdot f \quad (3.42)$$

In our OCT system, the focal length of the lens f =50 mm and the displacement is x =5.34 mm. Assuming that system optics has been aligned well, then $\Delta y = 0, \Delta z = 0$. The parameter m of equation (3.42) can be simplified as

$$m = \frac{tg(q')}{\sin(2a)} - \Delta z' = \frac{tg(q')}{\sin(2a)} - \frac{x}{f}\cdot tg(a)$$

$$= \frac{tg(q')}{\sin(2a)} - 0.1068\cdot tg(a) \quad (3.43)$$

3.2.1.1 Condition 1:

If $m \le 1$,

In the triangles ΔOIH and ΔODH shown in Figure 3.7,

$$\frac{\overline{BD}}{\overline{OD}} = \frac{\overline{GH}}{\overline{OH}} = m \quad (3.44)$$

$$\frac{\overline{GH}}{\overline{IH}} = tg(2a+\Delta a-b) \quad (3.45)$$

$$\frac{\overline{OH}}{\overline{IH}} = tg(2a+\Delta a) \quad (3.46)$$

So

$$\frac{tg(2a+\Delta a-b)}{tg(2a+\Delta a)}=m \tag{3.47}$$

$$tg(b)=\frac{(1-m)\cdot tg(2a+\Delta a)}{(1+m\cdot(tg(2a+\Delta a))^2)} \tag{3.48}$$

Thus, the reflected light from the scanning mirror will go through the lens and reconverge onto the diffraction grating at the incidence angle g ,

$$g=2a+\Delta a-b \tag{3.49}$$

The angle g will be affected by the parameters Δx , Δy , q' as well as a .

Then it will be diffracted towards the double-pass mirror at the diffraction angle g', which may be computed according to equation:

$$l=p\cdot(\sin(g)+\sin(g')) \tag{3.50}$$

3.2.1.2 Condition 2:

If $m>1$,

In the triangles $\Delta C''H''G''$ and $\Delta O''H''G''$ as shown in Figure 3.10,

$$\overline{C''O''}=(m-1)\cdot f\cdot tg(2a+\Delta a) \tag{3.51}$$

$$\overline{O''G''}=f\cdot tg(2a+\Delta a) \tag{3.52}$$

So

$$\frac{tg(2a+\Delta a+b)}{tg(2a+\Delta a)}=\frac{\overline{C''G''}}{\overline{O''G''}}=m \tag{3.53}$$

$$tg(b)=\frac{(m-1)\cdot tg(2a+\Delta a)}{(1+m\cdot(tg(2a+\Delta a))^2)} \tag{3.54}$$

The reflected light from the scanning mirror will go through the lens and reconverge onto the diffraction grating at the incidence angle g ,

$$g=2a+\Delta a+b \tag{3.55}$$

Then it will be diffracted towards the double-pass mirror at the diffraction angle g', which may be computed according to equation (3.50).

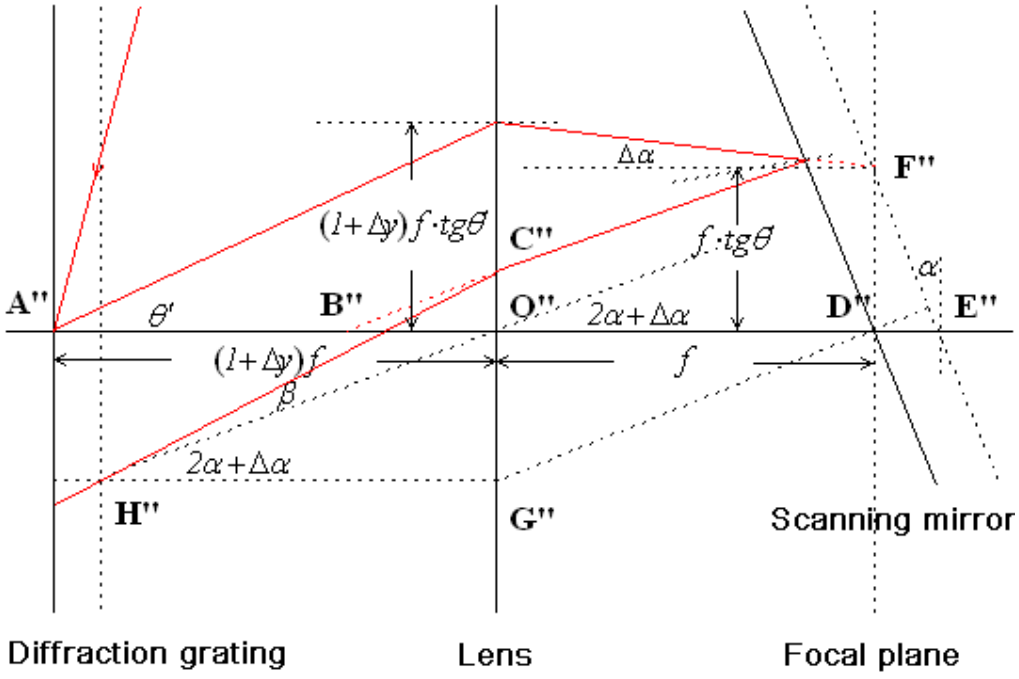

Figure 3.10: Ray tracing analysis of FD_ODL

3.2.2 Simulation results of the diffraction angle of back-reflected light

From the foregoing derivation, it can be seen that for the wavelength component l, the diffraction angle g' can't be kept constant; it will change with the rotation angle a of the scanning mirror. We chose some typical wavelength and rotation angles, and calculated the diffraction angle g'. To describe the degree of deflection from the incoming direction, $\Delta g'_{deflection}$ has been computed as

$$\Delta g'_{deflection} = g' - q \tag{3.56}$$

For center wavelength component l_0=800 nm of the light source, the incidence angle q equals to 28.68540250° and diffraction angle equals to $q' = 0^{\circ}$. To understand the ideal

condition for back-reflected light from FD_ODL, numerical simulation experiments have been performed, deflection angles for light of different wavelength components have been computed, and the results are shown in Figure 3.11. It can be seen that the deflection angle will increase with the absolute value of rotation angle $|a|$ of the scanning mirror. As the diameter of the core of the single-mode optical fibre in our system is only 5 microns and its numerical aperture is about 0.13, it will not be focused into the optical fibre well if the deflection angle $\Delta g'_{deflection}$ of the back-reflected light is too large. So the intensity of longer wavelength components of the light will attenuate or be lost with the increase of rotation angle $|a|$.

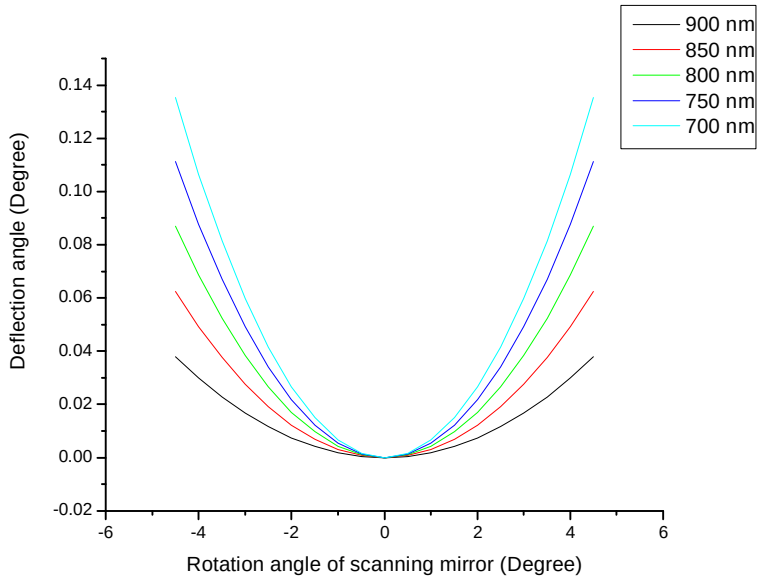

Figure 3.11: Deflection angle of back-reflected light

3.2.3 Function of double-pass mirror

When the light goes to the double-pass mirror at the incidence angle g', it will be reflected and goes to the diffraction grating at the incidence angle q_1 again. The incoming light will be spectrally dispersed by the diffraction grating at the diffraction angle q_1'. The reflected light from

the scanning mirror will go through the lens and reconverge onto the grating at the incidence angle g_1, and thence be diffracted back into the system at the diffraction angle g_1'.

From the Figure 3.12, we have that

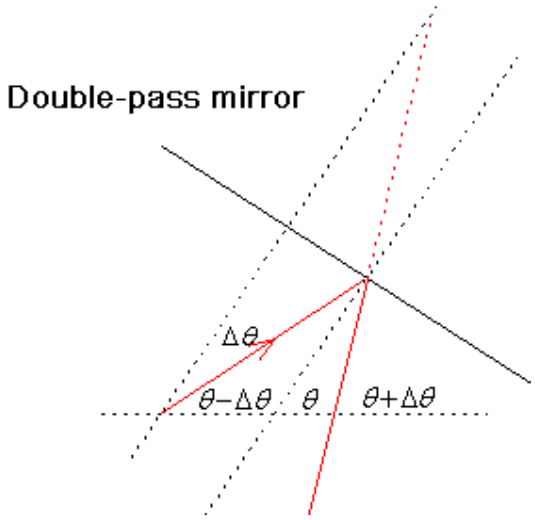

Figure 3.12: Function of double-pass mirror

$$g' = q - \Delta q \tag{3.49}$$

$$q_1 = q + \Delta q \tag{3.50}$$

where $\Delta q = -\Delta g'_{deflection}$.

From the general grating equation, the equation below may be obtained:

$$l = p \cdot (\sin(q) + \sin(q')) = p \cdot (\sin(q_1) + \sin(q_1')) \tag{3.51}$$

If $\Delta q > 0$, then $q_1 > q$, $q_1' < q'$.

If $\Delta q < 0$, then $q_1 < q$, $q_1' > q'$.

Numerical simulations have been further performed to investigate the effect of the double-pass mirror on the deflection angle. The simulation results are shown in Figure 3.13. It can be seen that the deflection angle $\Delta g_{1\ deflection}'$ will increase with the absolute value of rotation

angle of the scanning mirror. However, it has been reduced to an imperceptible value with the double-pass mirror.

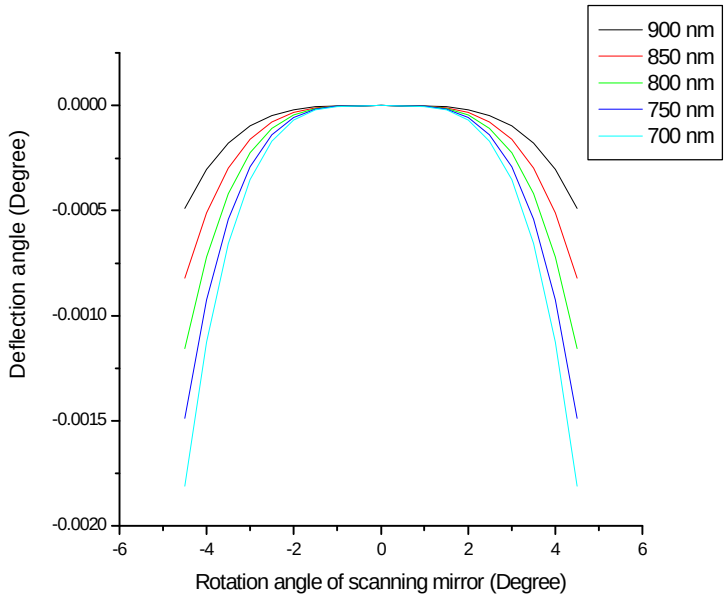

Figure 3.13: Deflection angle of back-reflected light with double-pass mirror

The quadratic equation $f(x) = a_0 + a_1 x + a_2 x^2$ was used to fit all curves in Figures 3.11 and 3.13, where a_0 is the constant coefficient, a_1 is the linear coefficient, and a_2 is the quadratic coefficient. Results are listed in table 3.2. In addition, the effect of the double-pass mirror was evaluated using below equation

$$Ra = \frac{\left|a_2(with \quad mirror) - a_2(ideal)\right|}{\left|a_2(no \quad mirror) - a_2(ideal)\right|} \tag{3.52}$$

where Ra is the ratio, $a_2(with \quad mirror)$ is the quadratic coefficient of the curves using the double-pass mirror, $a_2(no \quad mirror)$ is the quadratic coefficient of the curves without the double-pass mirror, $a_2(ideal)$ is the ideal quadratic coefficient of the curves. $a_2(ideal) = 0$ and no deflection angle will be generated when the scanning mirror rotates in ideal conditions.

Table 3.2: The fitted quadratic coefficient a_2 of the curves in Figures 3.11 and 3.13

	700 nm light	750 nm light	800 nm light	850 nm light	900 nm light
a_2 (no mirror)	0.0066730	0.0056539	0.0042929	0.0030939	0.0018735
a_2 (with mirror)	-0.00000776	-0.00000473	-0.00000368	-0.00000038	-0.00000023
Ra	0.0012	0.0008	0.0009	0.0001	0.0001

In table 3.2, Ra shows that the double-pass mirror has lowered down the quadratic coefficient at least 1000 times and its value is negligible with the double-pass mirror. The curves in Figure 3.13 approach to straight lines, therefore all wavelength components of light will be nearly parallel to the incoming direction and be coupled back into OCT system.

To simplify optical alignments and couple broader spectrum of reflected-back light into the system, the rotation angle of scanning mirror a should be controlled to smaller ranges. It is valuable to notice that $\Delta g_{1\ deflection}'$ has good symmetry about a. This point is very useful and has been used in our system. In order to achieve certain imaging depth, the rotation angle of the scanning mirror should be set to $|a|$. It can be realized by rotating the scanning mirror from $-a/2$ to $a/2$. This will achieve the same imaging depth and also efficiently reduce dispersion problem caused by the deflection angle $\Delta g_{1\ deflection}'$ in FD_ODL.

3.3 Optical implementation of FD_ODL

3.3.1 Optical layout of FD_ODL

The optical layout of FD_ODL is shown in Figures 3.14 and 3.15. From the top view as shown in Figure 3.14, it can be seen that scanning mirror can be controlled to scan symmetrically around the incoming direction. From the side view as shown in Figure 3.15, it can be seen that the

diffraction grating and lens have been moved downwards. The light beam will go down to hit the surface of scanning mirror. This will ensure that the double pass mirror can be put before fiber collimator and below the incoming light.

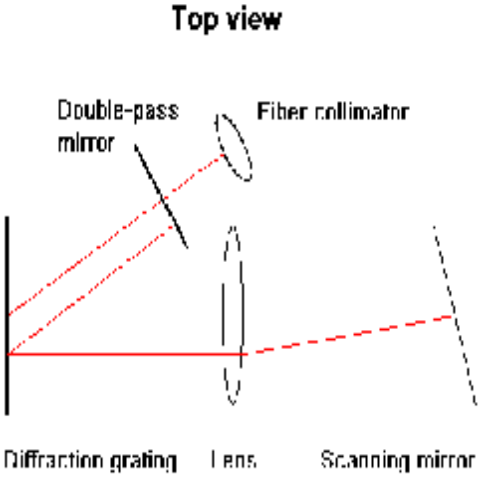

Figure 3.14: Top view of FD-ODL

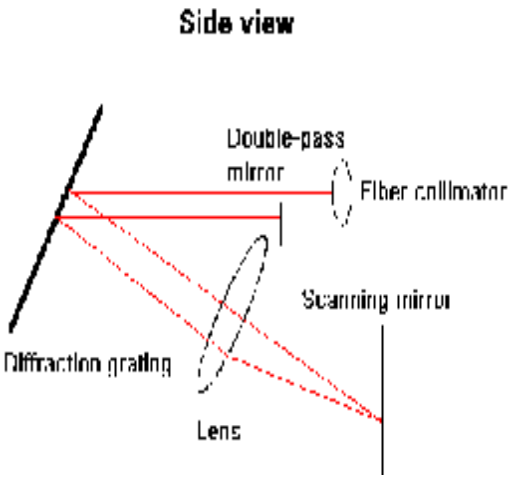

Figure 3.15: Side view of FD-ODL

The optical alignment procedure of FD-ODL can be divided into two steps. The first alignment step is to ensure that the incoming light hits the diffraction grating, from where the first order diffraction of centre wavelength light should go perpendicularly to hit the middle surface of the lens. After that, it will go to the scanning mirror and be reflected back by it, and then be aligned well to be coupled back into the system.

The second alignment step is to tilt the diffraction grating and the lens downwards. The light beam will then travel to the surface of the scanning mirror. After which it will be reflected back to just below the centre of the lens, and collide thereafter to the surface of the diffraction grating. The diffracted light will be below the incoming light, so the double pass mirror can then be properly placed between diffraction grating and the collimator. The light reflected from the double-pass mirror should be aligned well to go back into the system.

The spectrum of coupled-back light was acquired using the USB4000 portable spectrometer from Ocean Optics, Inc. Boxcar width was set to 10 and scans to average was set to 10.

The scanning mirror was controlled to different angles to check the effect of optics alignment. Figures 3.16-3.20 are some typical spectra under different rotation angles 1.84, 0.92, 0, -0.92, -1.84 degrees. We can see that broad spectrum from reference arm has gone back into OCT system when the scanning mirror rotated. In addition, we analyzed the spectrum under different rotation angles, the area, centroid and FWHM of spectrum, as shown in Figures 3.21-3.23. These figures showed that the spectra are not very stable, so optical alignment should be further optimized in future experiment.

Interestingly, it was observed that the spectrum of coupled-back light is broader than that of the original light (about 160 nm). This was mainly due to self phase modulation, Raman, soliton, and four-wave mixing effects in the normal, positive dispersion optical fibres [93].

3.3.2 Optical alignment of FD_ODL

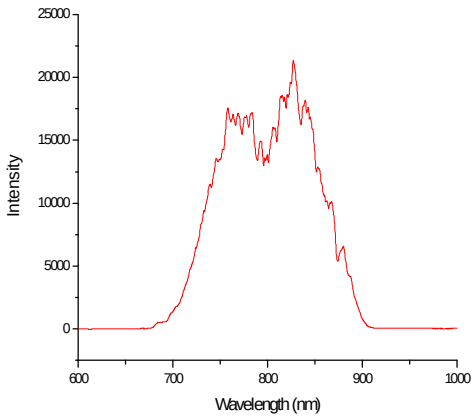

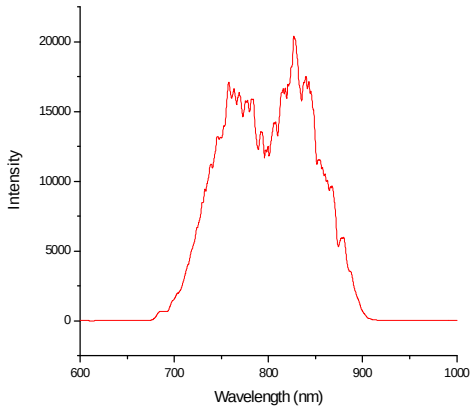

Figure 3.16: Spectrum under 1.84 degree (0.4 volt)

Figure 3.17: Spectrum under 0.92 degree (0.2 volt)

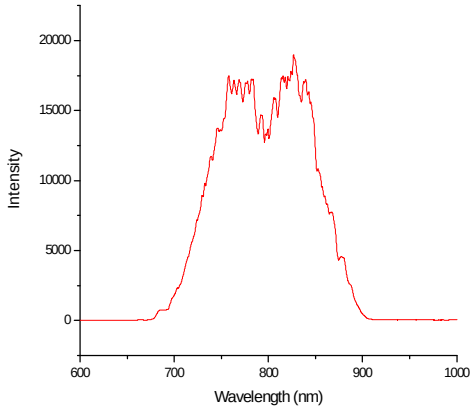

Figure 3.18: Spectrum under 0 degree (0 volt)

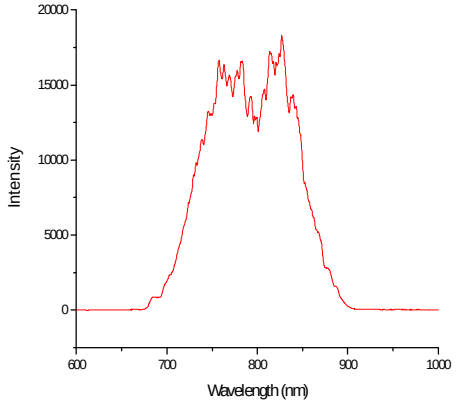

Figure 3.19: Spectrum under -0.92 degree (-0.2 volt)

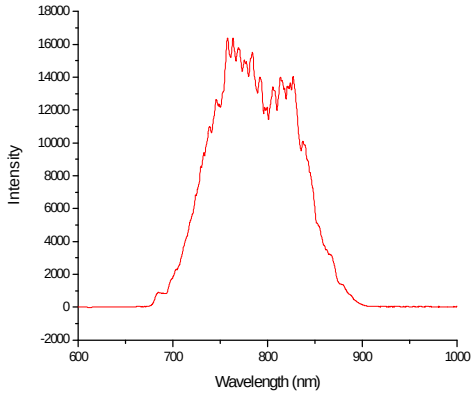

Figure 3.20: Spectrum under -1.84 degree (-0.4 volt)

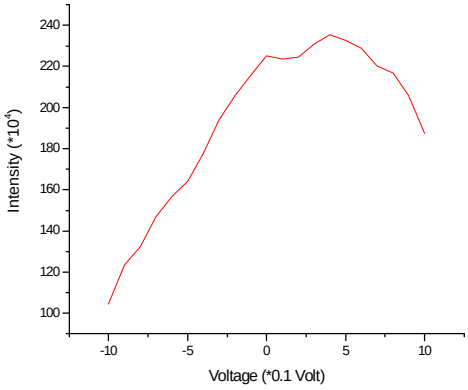

Figure 3.21: Area of spectrum

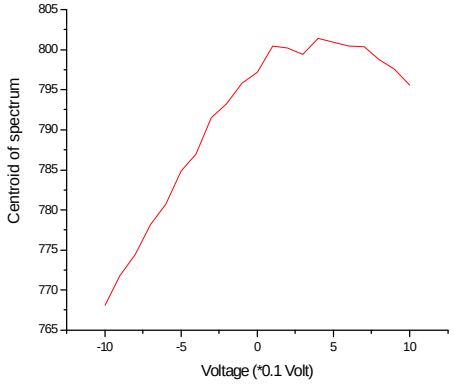

Figure 3.22: Centroid of spectrum

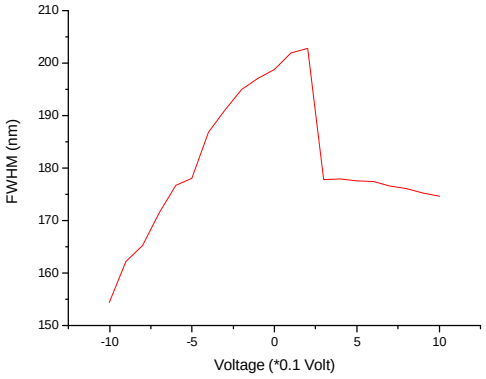

Figure 3.23: FWHM of spectrum

The optical alignment of FD_ODL is a difficult and time-consuming work. To enable broad-band spectrum of light source to go back into the OCT system, lots of optical alignment experiments were performed in the lab. We found that many parameters would affect the spectrum of light that goes back into the system from FD_ODL.

The most important four parameters are: (1) The incidence angle of the light source, (2) The offset from the centre of the lens, (3) The distance between the diffraction grating and the lens, and (4) The distance between the scanning mirror and the lens. They will greatly affect the shape of the spectrum, especially when the scanning mirror rotates. However, if the spectrum going back from FD_ODL is not stable, the interferometric signal caused by it and the spectrum going back from biological sample will be affected. The resolution of OCT system will be degraded, such that an optimization of these parameters and minimization of their effect on the shape of spectrum will efficiently improve the system capability.

To improve further the optical alignment of FD_ODL, we have estimated quantitatively the tolerance of these parameters. These values can provide a valuable guidance for the fabrication of FD_ODL. The tolerance of these parameters was calculated according to the criteria that the fluctuation of spectrum intensity would be within 10%.

3.3.2.1 The incidence angle of light source (Static)

Align the optics well, and then rotate the mirror mount to change the incidence angle of light source. The spectra going back into OCT system was recorded at the same time. These spectra have been analyzed and the area, centroid and FWHM of spectrum have been calculated as shown in Figures 3.24, 3.25, 3.26. The experimental results have shown that the shape and intensity of spectrum have been greatly affected by the incidence angle of light source.

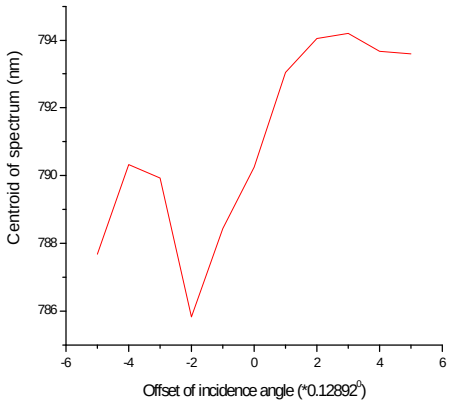

Figure 3.24: Centre of spectrum at different offset of incidence angle

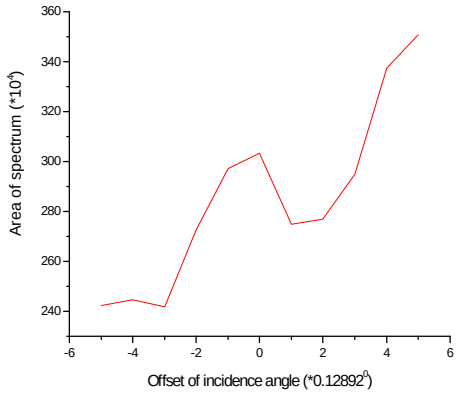

Figure 3.25: Area of spectrum at different offset of incidence angle

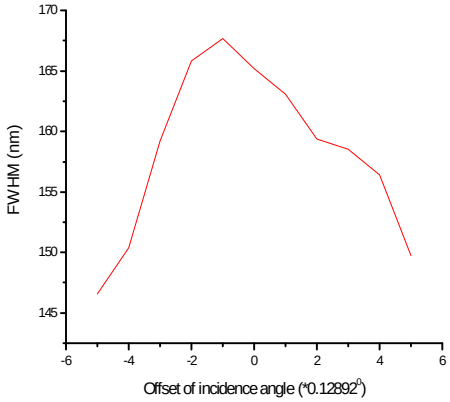

Figure 3.26: FWHM of spectrum at different offset of incidence angle

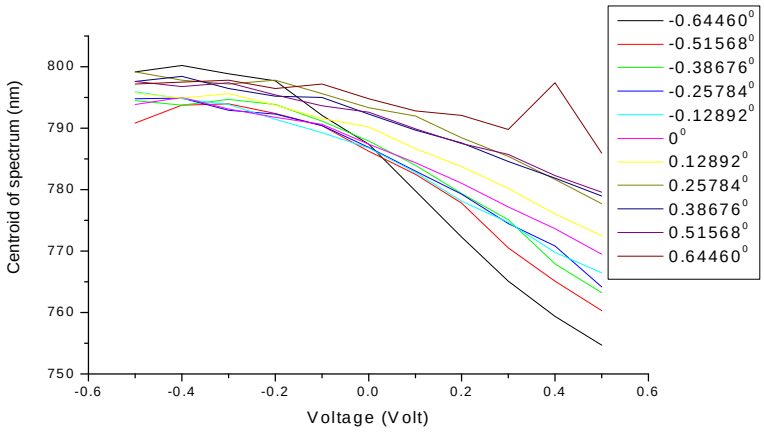

Figure 3.27: Centre of spectrum when scanning mirror rotates

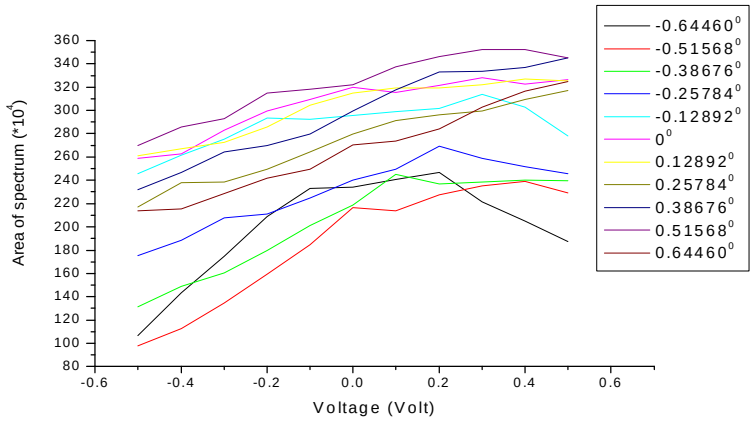

Figure 3.28: Area of spectrum when scanning mirror rotates

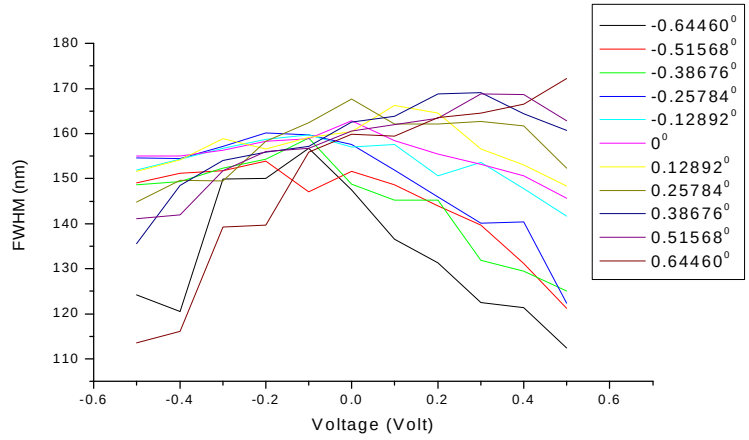

Figure 3.29: FWHM of spectrum when scanning mirror rotates

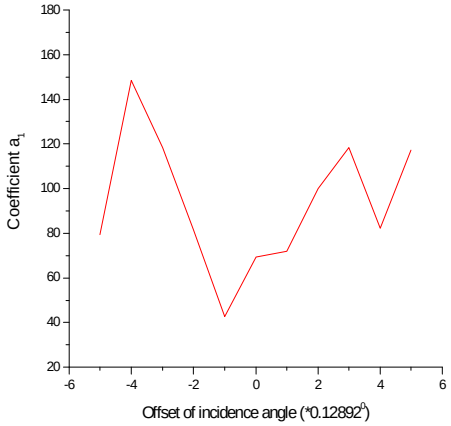

Figure 3.30: Coefficient a_1

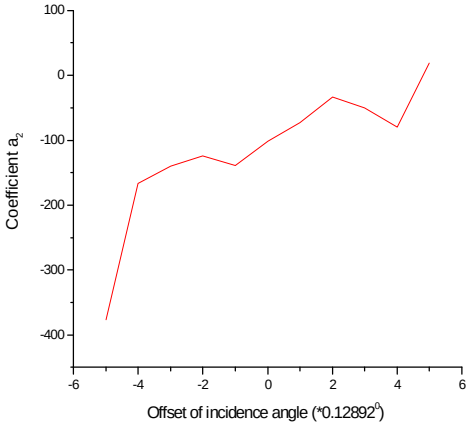

Figure 3.31: Coefficient a_2

For different offset values of the incidence angle, the scanning mirror was controlled to rotate symmetrically. The spectra have been analyzed as shown in Figures 3.27, 3.28, 3.29. Experimental results show that these spectra have nearly the same changing trend at different offsets of the incidence angle. In Figure 3.28, it can be seen that the intensity of spectrum fluctuates obviously at different offset of the incidence angle. The spectrum at 0.12892^0 or -0.12892^0 offset of the incidence angle can approach the spectrum at 0^0 offset of the incidence angle within 10% fluctuation of the intensity. So the tolerance of the incidence angle of light source can be set to 0.12892^0.

Quadratic equation $f(x) = a_0 + a_1 x + a_2 x^2$ was used to fit the curves in Figures 3.28. Results are shown in Figures 3.30, 3.31, it can be seen that coefficients a_1 and a_2 fluctuate very obviously with the change of the incidence angle. This proved that the shape and intensity of spectrum is very sensitive to the incidence angle of light source.

3.3.2.2 Centre of the lens (static) (From left to right)

Align the optics well, and then move the lens from left to right. The spectra going back into the OCT system was recorded at the same time. These spectra have been analyzed as shown in

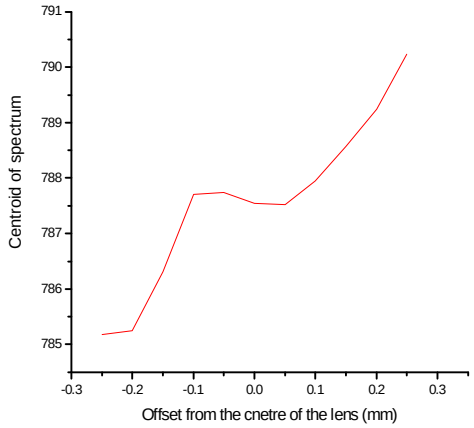

Figure 3.32: Centre of spectrum at different offset from the centre of the lens

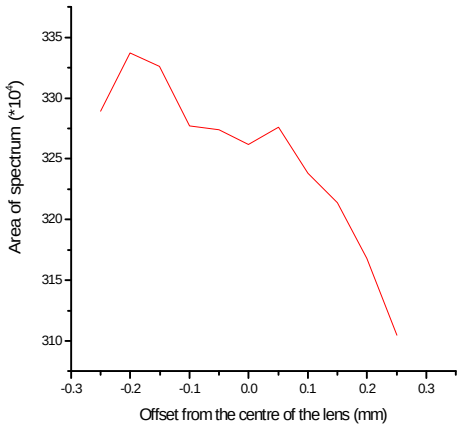

Figure 3.33: Area of spectrum at different offset from the centre of the lens

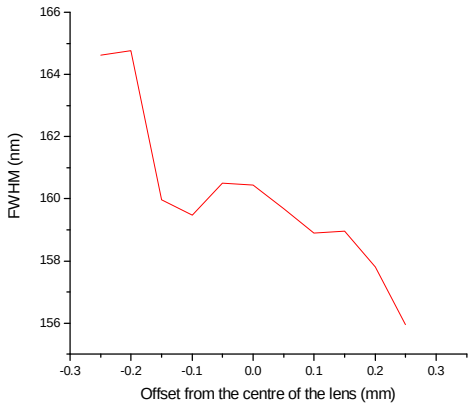

Figure 3.34: FWHM of spectrum at different offset from the centre of the lens

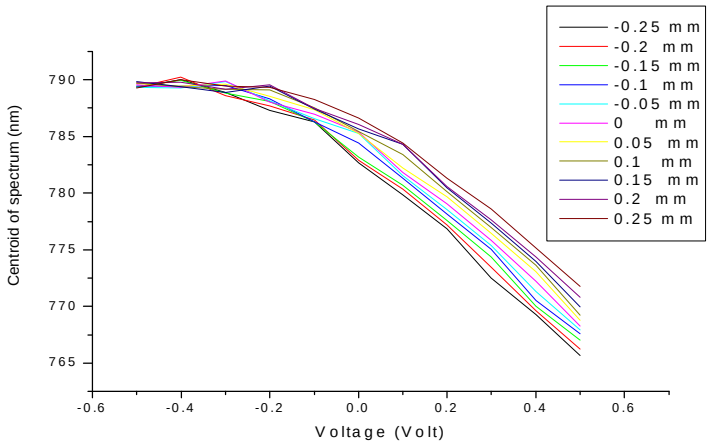

Figure 3.35: Centre of spectrum when scanning mirror rotates

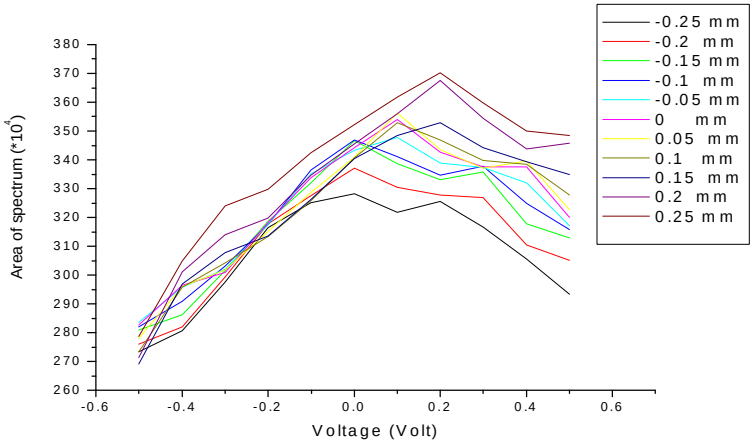

Figure 3.36: Area of spectrum when scanning mirror rotates

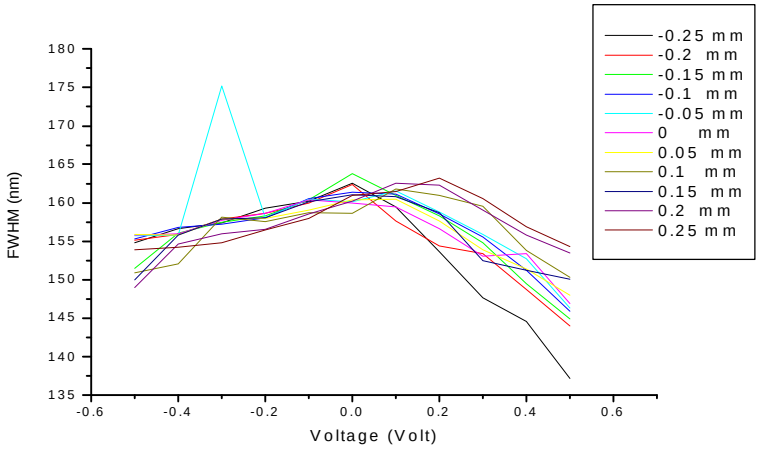

Figure 3.37: FWHM of spectrum when scanning mirror rotates

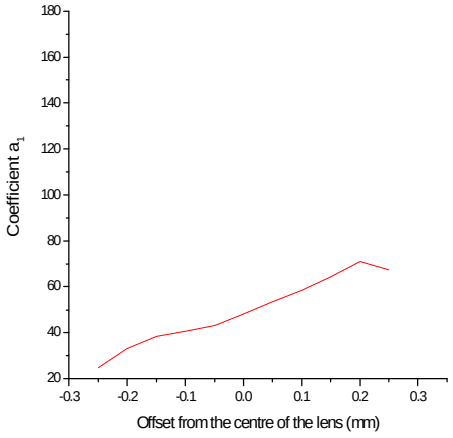

Figure 3.38: Coefficient a_1

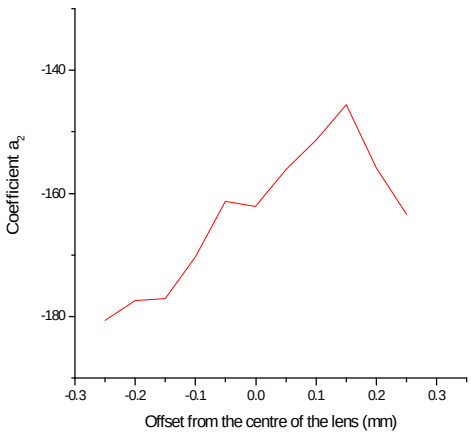

Figure 3.39: Coefficient a_2

Figures 3.32, 3.33, 3.34. The experimental results have shown that the shape of the spectrum changed and the centre of the spectrum increased. The intensity of spectrum will decrease when the lens moves from left to right.

For every position of the offset from the centre of the lens, the scanning mirror was controlled to rotate symmetrically. The relevant sequences of spectrum have been acquired and analyzed as shown in Figures 3.35, 3.36, 3.37. Experimental results show that these spectra have nearly the same changing trend at different offsets from the centre of the lens. In Figure 3.36, it

can be seen that the intensity of spectrum fluctuates imperceptibly at different offsets from the centre of the lens. The spectrum at -0.1mm or 0.1mm offset from the centre of the lens can approach the spectrum at 0 offset from the centre of the lens within 10% fluctuation of the intensity. The tolerance of the centre of the lens can be set to 0.1mm.

All curves in figure 3.36 were fitted using quadratic equation and results are shown in Figures 3.38, 3.39. It can be seen that coefficients a_1 and a_2 fluctuate negligibly at different offsets from the centre of the lens. This proved that the shape and intensity of spectrum is not sensitive to the offset from the centre of the lens.

3.3.2.3 Distance between diffraction grating and the lens (Static)

After optical alignment, the spectra going back into the OCT system was recorded for variant distances between the diffraction grating and the lens, as shown in Figures 3.40, 3.41, 3.42. The experimental results show that the shape of the spectrum is not sensitive to the distance between the diffraction grating and the lens.

For different distances between diffraction grating and lens, the scanning mirror was controlled to rotate symmetrically and the relevant sequences of spectrum were acquired and

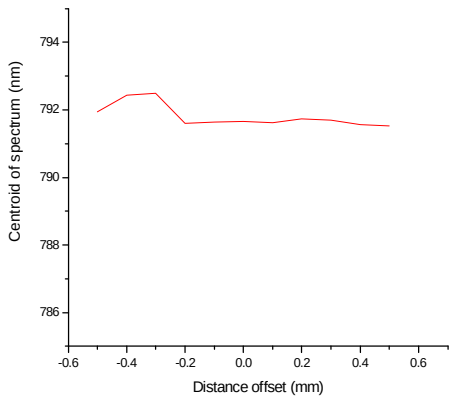

Figure 3.40: Centre of spectrum at different distance offset

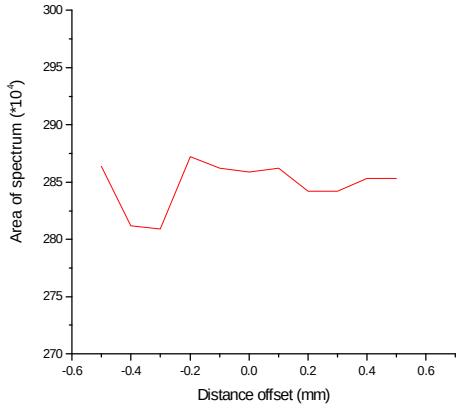

Figure 3.41: Area of spectrum at different distance offset

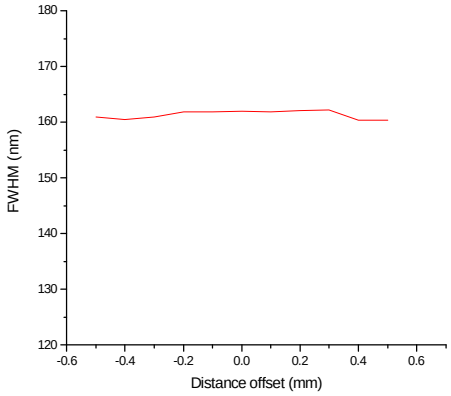

Figure 3.42: FWHM of spectrum at different distance offset

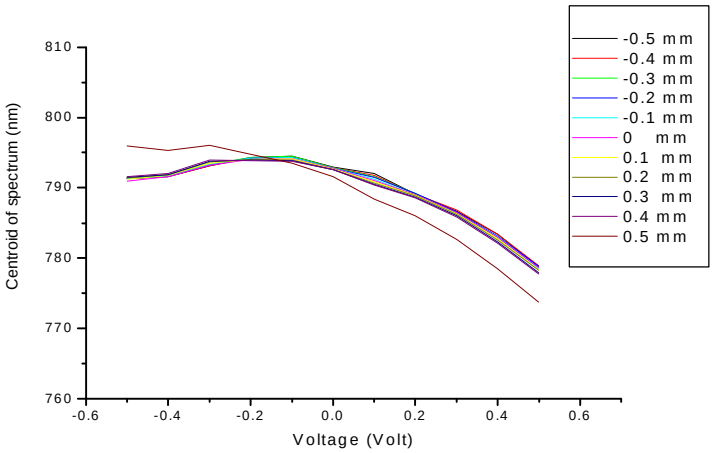

Figure 3.43: Centre of spectrum when scanning mirror rotates

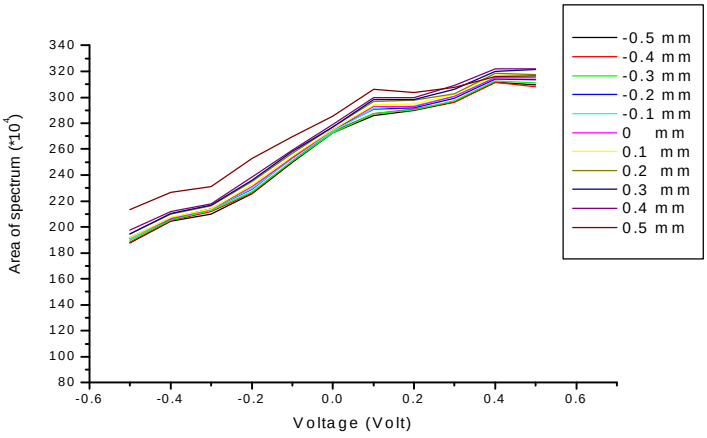

Figure 3.44: Area of spectrum when scanning mirror rotates

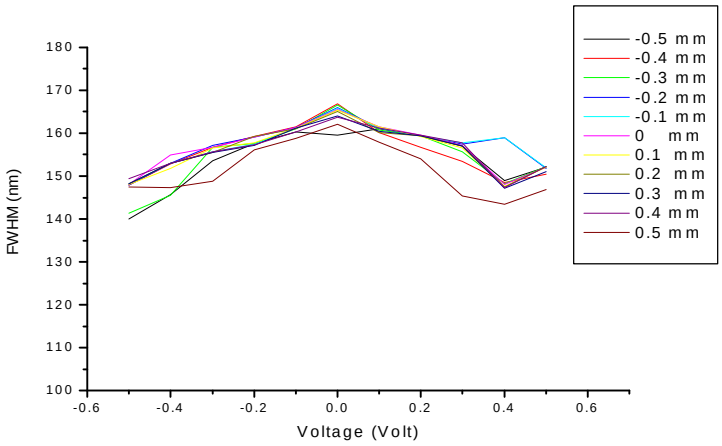

Figure 3.45: FWHM of spectrum when scanning mirror rotates

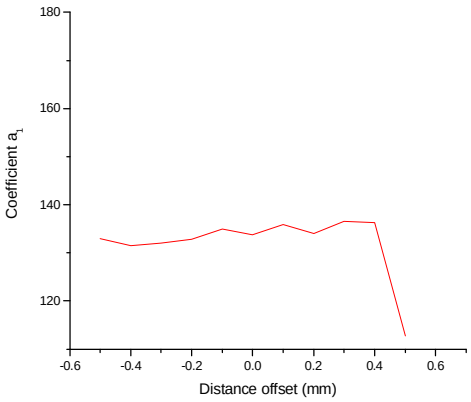

Figure 3.46: Coefficient a_1

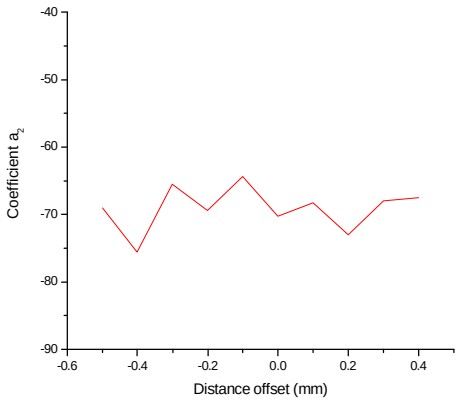

Figure 3.47: Coefficient a_2

analyzed as shown in Figures 3.43, 3.44, 3.45. Experimental results show that the shapes of these spectra are similar at different distance offsets. In Figure 3.44, it can be seen that the intensity of spectrum fluctuates negligibly at different distance offsets. The tolerance of the distance between the diffraction grating and the lens can be set to 0.2 mm.

All curves in Figure 3.44 were fitted using quadratic equation and results are shown in Figures 3.46, 3.47. It can be seen that coefficients a_1 and a_2 fluctuate less than 10% at different distance offsets between diffraction grating and lens. This proved that the shape and intensity of spectrum is not sensitive to the distance between diffraction grating and the lens.

3.3.2.4 Distance between the lens and the scanning mirror (Static)

After optical alignment, the spectra going back into the OCT system was recorded for variant distances between the lens and the scanning mirror, as shown in Figures 3.48, 3.49, 3.50. The experimental results show that the shape of the spectrum is very sensitive to the distance between the lens and the scanning mirror. In Figure 3.49, it can be seen that the intensity of spectrum decreases quickly with increase in absolute value of the distance offset.

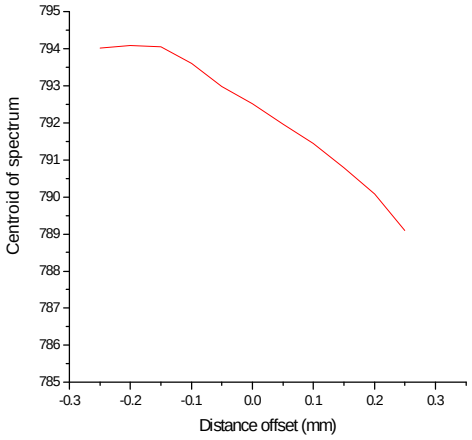

Figure 3.48: Centre of spectrum at different distance offset

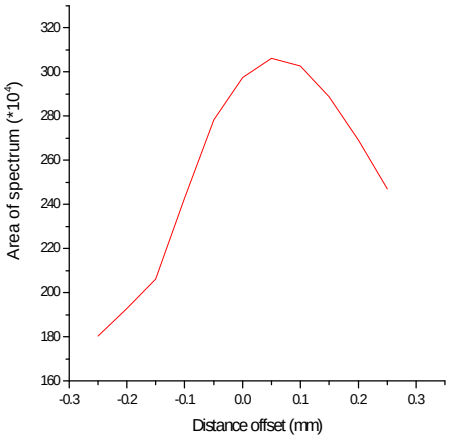

Figure 3.49: Area of spectrum at different distance offset

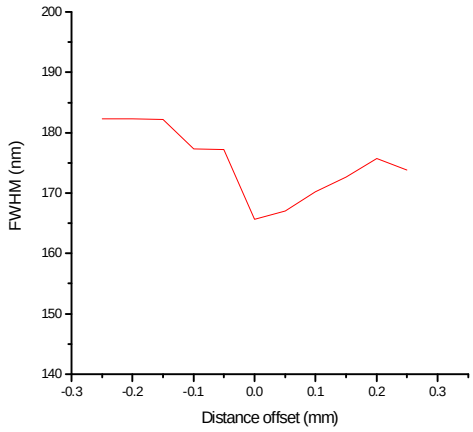

Figure 3.50: FWHM of spectrum at different distance offset

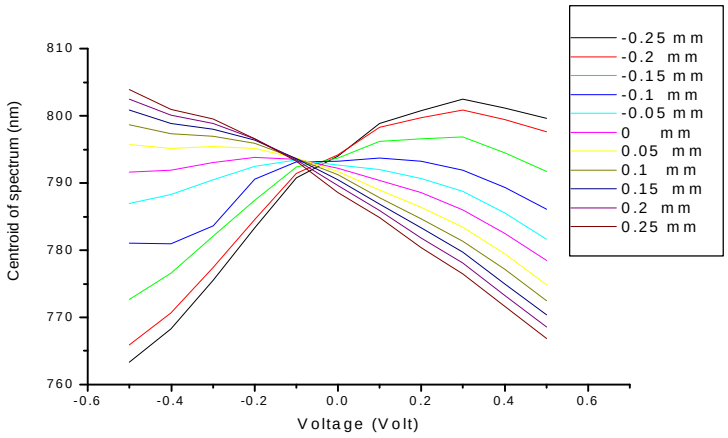

Figure 3.51: Centre of spectrum when scanning mirror rotates

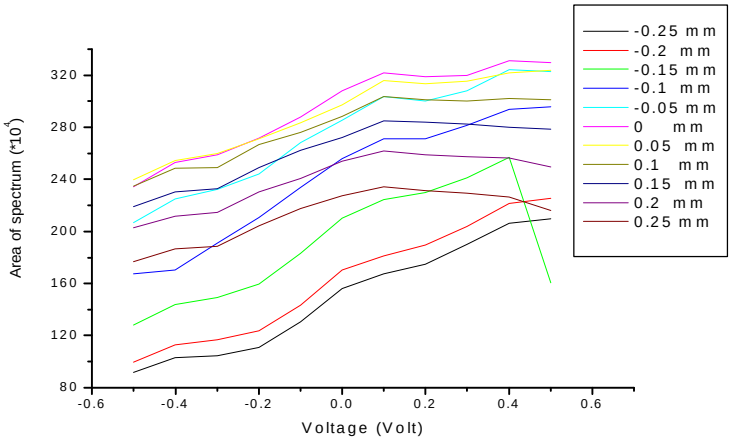

Figure 3.52: Area of spectrum when scanning mirror rotates

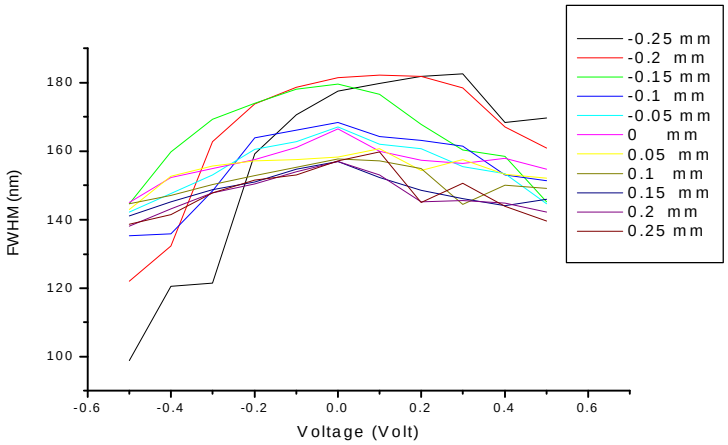

Figure 3.53: FWHM of spectrum when scanning mirror rotates

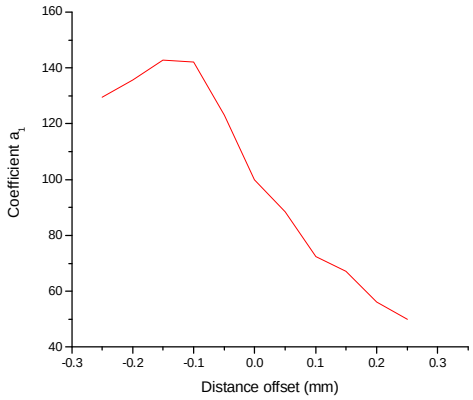

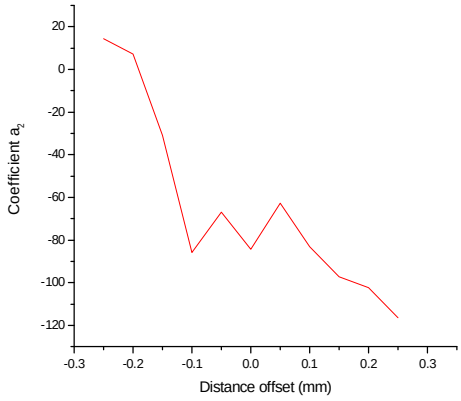

Figure 3.54: Coefficient a_1

Figure 3.55: Coefficient a_2

For different distances between the lens and the scanning mirror, the scanning mirror was controlled to rotate symmetrically and the relevant sequences of spectrum were acquired as shown in Figures 3.51, 3.52, 3.53. Figure 3.51 shows that the centroid of the spectrum has a reverse changing trend when the distance offset was changed from negative value to positive value. Figure 3.52 shows that the intensity of spectrum is affected very noticeably by different distance offsets. The spectrum at 0.05 mm distance offset can approach the spectrum at 0 mm distance offset within 10% fluctuation of the intensity. However, the spectrum at -0.05 mm distance offset can not approach well the spectrum at 0 mm distance offset within 10% fluctuation of the intensity. So the tolerance of the distance between the lens and the scanning mirror can be set to 0.03 mm.

All curves in Figure 3.52 were fitted using quadratic equation and results are shown in Figures 3.54, 3.55. It can be seen that coefficients a_1 and a_2 fluctuate very obviously at different distance offsets between the lens and the scanning mirror. This proved that the shape and intensity of the spectrum is very sensitive to the distance between the lens and the scanning mirror.

3.4 Effect of spectrum shape from FD_ODL on the system resolution

In a standard OCT system, the broad-band optical beam will be divided into two paths, one to

the reference optical delay line, and one to the sample arm. If the spectrum going back from FD_ODL is not stable, this will result in differing spectrum returning from the two arms of the interferometer and hence, the resulting interferometric signal will be affected. Experimental results show that the center wavelength and intensity of spectrum from FD_ODL have small fluctuations when the scanning mirror rotates. To further investigate their effect on the system resolution, numerical simulations have been conducted.

Assume that the reference spectrum and the sample spectrum can be represented as $E_R(l)$ and $E_S(l)$ respectively with Gaussian distributions,

$$E_R(l) = Ae^{-\frac{(l-(l_0-\Delta l))^2}{s^2}} e^{-j(2p(x+\Delta x)/l - wt)} \tag{3.52}$$

$$E_R(l) = e^{-\frac{(l-l_0)^2}{s^2}} e^{-j(2px/l - wt)} \tag{3.53}$$

where Δl is the offset from centre wavelength l_0=800 nm. A is the scale factor to be used to describe the intensity fluctuation of the reference spectrum compared to the sample spectrum. Then the interference signal I at the detector is proportional to the real part of the cross-spectral term $E_R^* E_S$,

$$I \propto real\{\int_{-\infty}^{\infty} E_R(l) * E_S(l) dl\} \tag{3.54}$$

3.4.1 Offset from center wavelength at 800 nm

The effect of offset from centre wavelength on the OCT system has been simulated. Figure 3.56 shows the result of the intensity that will be detected at the photodiodes when small deviation of centre wavelength exists in the reference spectrum from FD_ODL. It can be seen that the intensity of interferometric signal will decrease if there exists small deviation of centre wavelength. Figure 3.57 shows the numerical simulation result of the interference signal at different centre wavelength offsets -50 nm, 0 nm and 50 nm. These interference signals under different offsets are

produced according to equation (3.54). Then the FFT method was used to extract the envelope of the interference signal and the deviation of the envelope was evaluated using curve fitting method. Figure 3.58 is the result of the deviation of the envelope at different centre offsets. It can be seen that the offset from center wavelength 800 nm will degrade the system resolution.

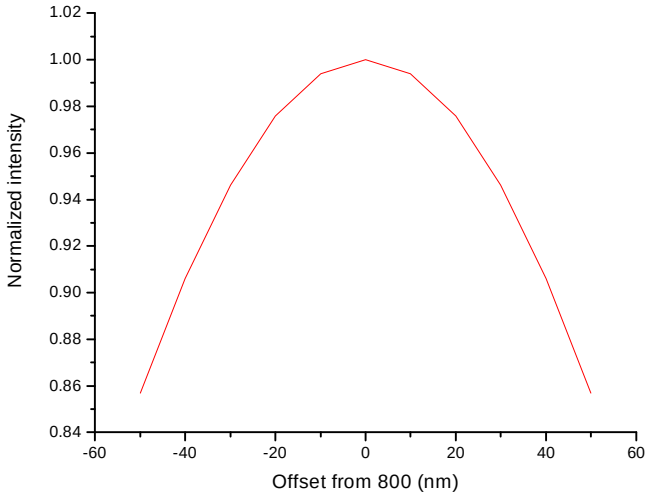

Figure 3.56: Intensity of interferometric signal at different centre offsets

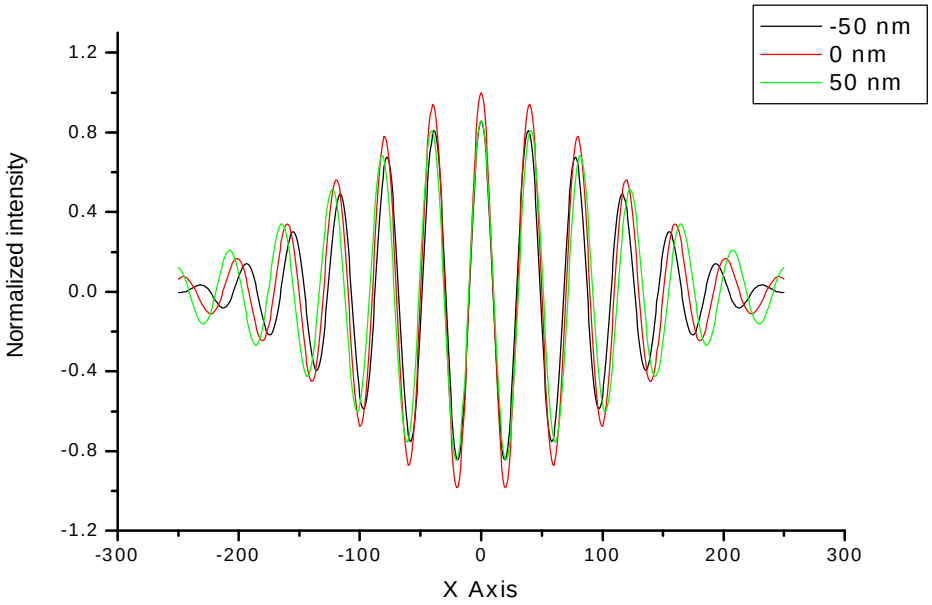

Figure 3.57: Interference spectrum at different centre offsets

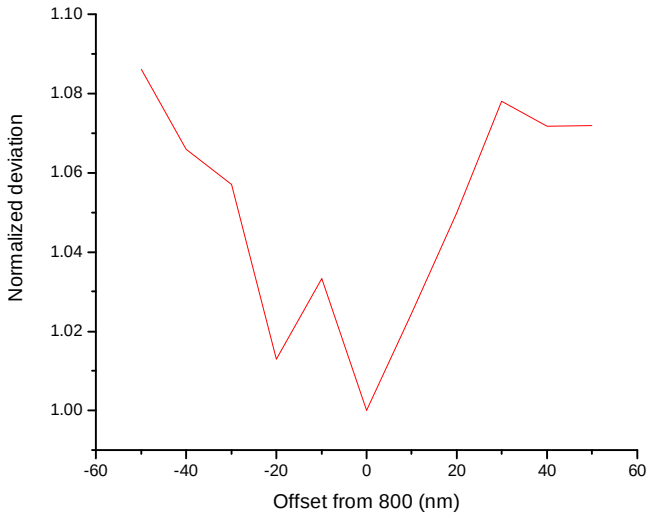

Figure 3.58: Deviation of the envelope at different centre offsets

3.4.2 Intensity of spectrum

The effect of the reference spectrum intensity from FD_ODL on the OCT system has been investigated. Figure 3.59 shows the intensity detected at the photodiodes for small fluctuations of the reference spectrum intensity. It can be seen that the intensity of the interferometric signal is

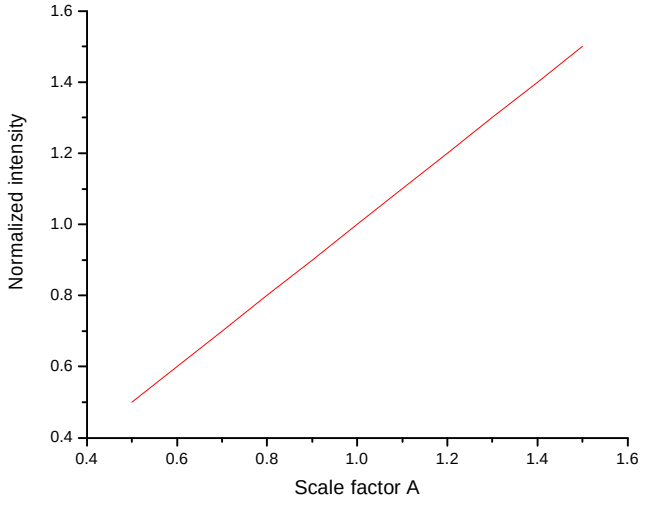

Figure 3.59: Intensity of interferometric signal at different scale factors

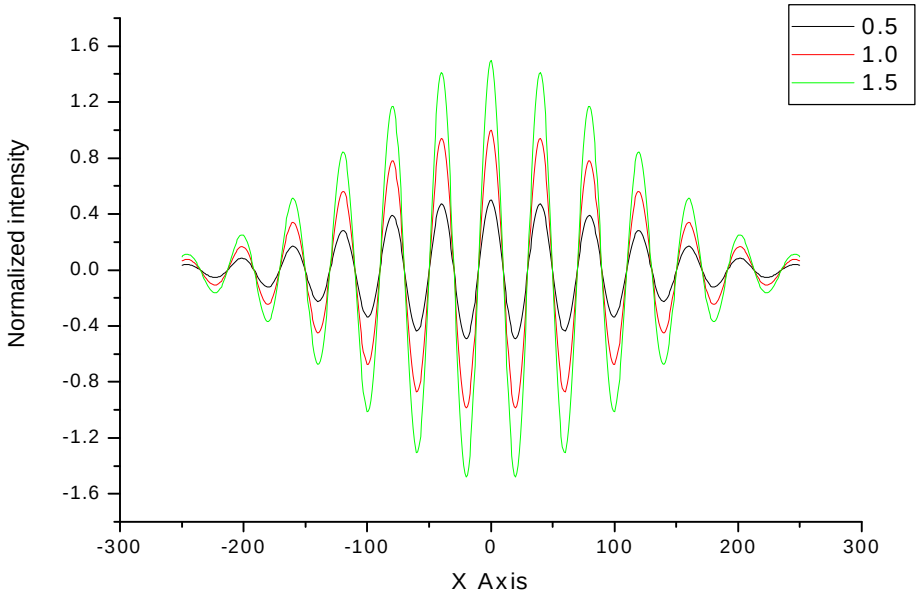

Figure 3.60: Interference spectrum at different scale factor

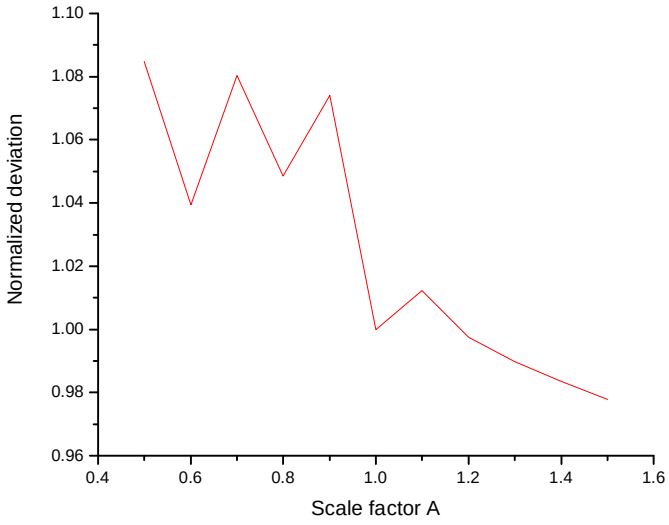

Figure 3.61: Deviation of the envelope at different scale factor

nearly proportional to scale factor. Figure 3.60 is the numerical simulation result of the interference signal at different intensities of the reference spectrum, where the scale factor A

was set to 0.5, 1.0 and 1.5 respectively. These interference signals under different intensities are produced according to equation (3.54). Then the FFT method was used to extract the envelope of the interference signal and the deviation of the envelope was evaluated using curve fitting. Figure 3.61 shows the deviation of the envelope for different intensity scale factors. It can be seen that the decrease of intensity of the reference spectrum will degrade the system resolution. However, the increase of intensity of the reference spectrum will slightly improve the system resolution

3.4.3 Rotation of scanning mirror

When the scanning mirror rotates, there is some slight fluctuation in the shape of spectrum from FD_ODL. The center wavelength and intensity of spectrum will change with the rotation angle of scanning mirror at the same time. In order to simulate the interference spectrum, $A(x), \Delta l(x)$ was calculated as the function of control voltage of scanning mirror.

Quadratic equation $f(x) = a_0 + a_1 x + a_2 x^2$ was used to fit the curves in Figures 3.21 and 3.22. Figure 3.21 shows the fluctuation of the intensity of reference spectrum, with fitted parameters a_0 =218.98, a_1 =5.0999, a_2 =-0.711. So the scale factor for the intensity of reference spectrum can be described as

$$A(x) = 1 + (\frac{a_2}{a_0}) \cdot x^2 = 1 - 0.00325 \cdot x^2 \tag{3.55}$$

Figure 3.22 shows the deviation of centre wavelength of reference spectrum, with fitted parameters a_0 =797.11, a_1 =1.502, a_2 =-0.15782. So the offset from the centre wavelength of reference spectrum can be described as

$$\Delta l(x) = -0.15782 \cdot x^2 \tag{3.56}$$

Figure 3.62 shows the intensity detected at the photodiodes when the scanning mirror rotates. It can be seen that the intensity of the interferometric signal decreases as the scanning mirror

rotates. Figure 3.63 is the numerical simulation result of the interference signal at different rotation angles of the scanning mirror, the control voltage for scanning mirror being set to 0, 0.5 and 1.0 volt respectively. These interference signals for different rotation angle of the scanning mirror are

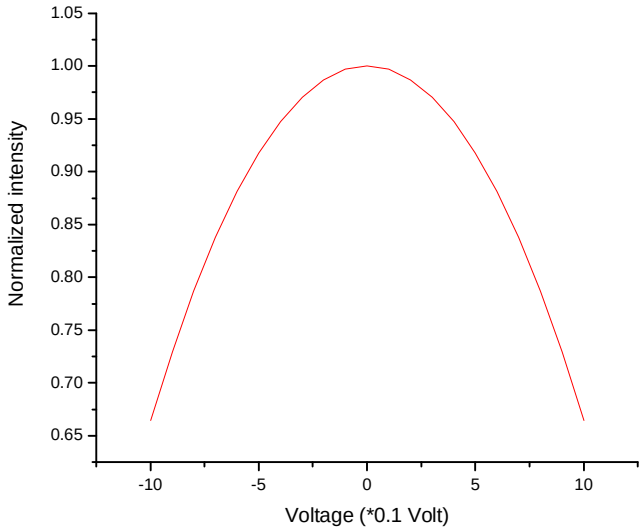

Figure 3.62: Intensity of interferometric signal when scanning mirror rotates

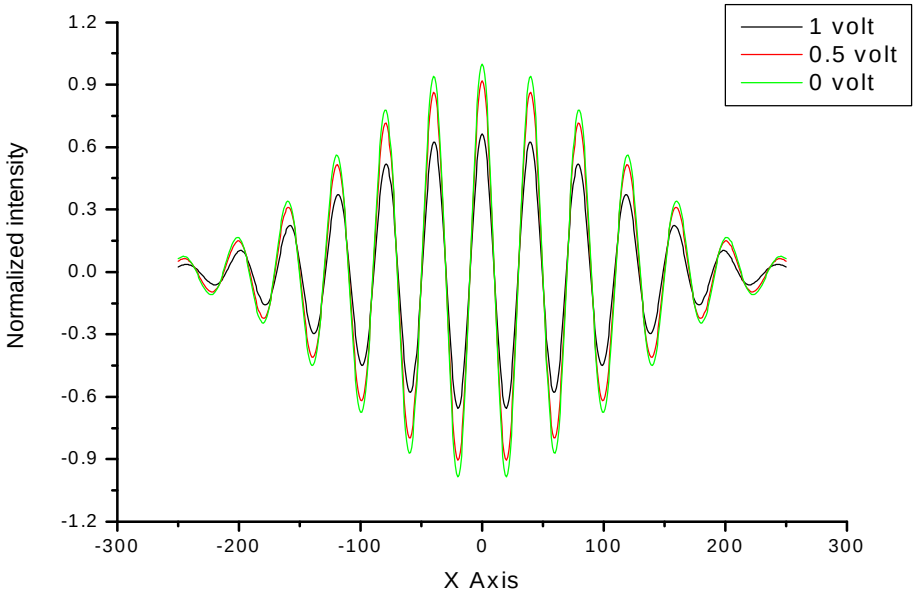

Figure 3.63: Interference spectrums at different rotation angle of scanning mirror

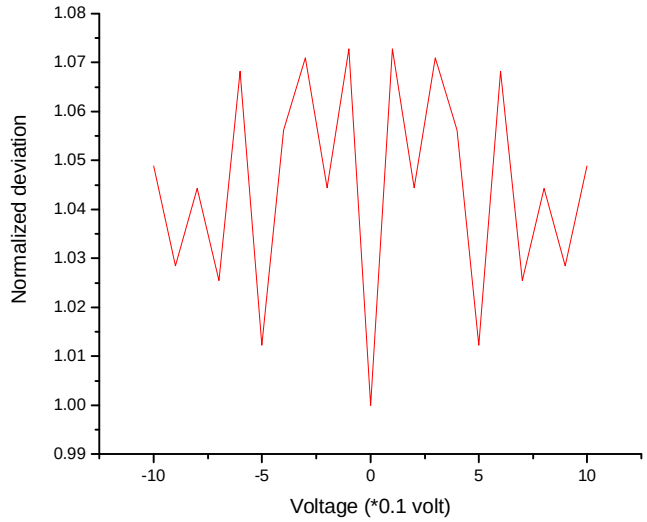

Figure 3.64: Deviation of the envelope when scanning mirror rotates

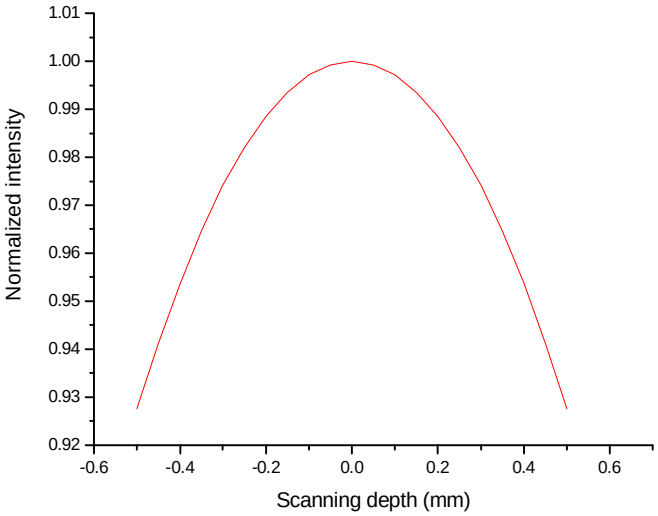

Figure 3.65: Intensity of interferometric signal when scanning mirror rotates

generated from equation (3.54), where equations (3.55), (3.56) will be incorporated into. Then the FFT method was used to extract the envelope of the interference signal and the deviation of the envelope was evaluated using curve fitting. Figure 3.64 shows the deviation of the envelope when

the scanning mirror rotates. It can be seen that rotation of scanning mirror degrades the system resolution.

According to equation (3.28), in order to achieve the scanning depth z =1 mm of FD_ODL, the tilt angle of scanning mirror $s \approx 2.15^{\circ}$. The control voltage for scanning mirror should be set as about 0.47 volt. Figure 3.65 shows the result of the intensity that will be detected at the photodiodes when scanning depth of FD_ODL was controlled to 1 mm.

3.5 Conclusions

In this chapter, we have studied thoroughly the fast FD_ODL for time domain OCT system. A sufficient scanning depth (more than 1 millimeter) can be achieved with high repeatability (several kHz) using this design. The relationship between phase delay and group delay of the interferometric signal of time domain OCT system has been investigated. We found that the offset of the scanning mirror can control numbers of oscillations inside the envelope of the interferometric signal. The constrained condition among the focal length of the lens, numbers of oscillations inside the envelope and the minimal size of the scanning mirror has been obtained. In addition, the scanning depth of the OCT system is related to the tilt angle of the scanning mirror. These important relationship equations will help to set up FD_ODL.

To allow broadband spectrum of light source to go back into OCT system, the optics implementation of FD_ODL has been investigated. Results show that the reference spectrum returning from FD_ODL is sensitive to the incidence angle of light source and distance between the lens and the scanning mirror. The fabrication accuracy for the incidence angle of light source and the lens to scanning mirror distance should be at least $28.68586^{0} \pm 0.12892^{0}$, 50 ± 0.03 mm separately. Since the reference spectrum is not very sensitive to the offset from the

centre of the lens and the distance between diffraction grating and the lens, it is acceptable for their fabrication accuracy to be 0 ± 0.1 mm, 50 ± 0.2 mm separately.

Geometric ray tracing analysis has been used to analyze the dispersion problem of FD_ODL when broadband light source was introduced. Its appropriate optics layout has been proposed to minimize the dispersion problem.

In addition, when the scanning mirror rotates, the reference spectrum is not stable if optics alignment for FD_ODL has not been done well. There is a small deviation on the centre wavelength and intensity of the reference spectrum. Numerical simulations have been performed to verify their effect on the system resolution. Results show that when the scanning mirror rotates, the slight offset from center wavelength and the intensity decrease of the reference spectrum returning from FD_ODL will degrade the system resolution.

Chapter 4 Design of the sample probe for time-domain OCT system

4.1 Basic theory of the sample probe

It is well known that most time-domain OCT systems perform A-scan (in-depth scan) firstly. The probing depth and scanning speed can be controlled by the optical delay line of the reference arm. However, in order to acquire cross-sectional imaging of tissues (B-scan), lateral scanning must be performed sequentially along the tissue surface. A sample probe should provide the function of lateral scanning. In addition, another important purpose of the sample probe is to deliver and focus the light onto the tissue surface and reconverge the scattered light back to the OCT system. Usually lateral scanning is slower than in-depth scanning [94].

To meet different application requirements, different kinds of sample probe for the OCT system have been designed [94-101]. These sample probes can be classified into three types: circumferential, deflecting and translational probes. In these sample probes, the light beam will be moved in different ways.

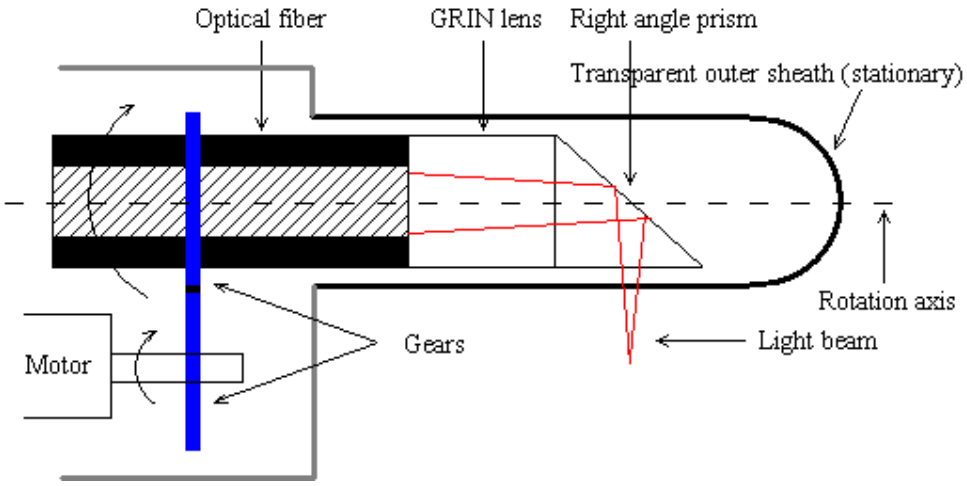

Figure 4.1: The circumferential probe

In the circumferential probe, the focusing light beam will be controlled to rotate about the probe axis. One probe of this kind is shown in Figure 4.1 [95, 96]. It mainly consists of optical fiber, Graded index (GRIN) lens and right angle prism. They are packaged into a transparent sheath. The output light beam from the optical fiber will be focused by the GRIN lens and be directed perpendicular to the axis of the probe by the right angle prism. When the probe is driven by a DC motor to rotate, the light beam is scanned circumferentially around the sample. An OCT image is usually acquired as the rotation angle is varied 360 degree. The circumferential probe can be constructed small size, diameter of about 1 mm, using miniature focusing and directing optics, and suitable for imaging internal organ systems, such as the intravascular system, the urinary tract and the respiratory tract, etc. [97].

In the deflecting probe, the focusing light beam will be controlled to deflect transversely to its incidence direction. Different mechanisms have been proposed to cause the deflection of the light beam. For example, the optical fiber is translated periodically by motors, piezoelectric cantilevers, or elastrostatic or magnetic techniques as shown in Figure 4.2 [98, 99]. In this method, the translation of optical fiber is enough to move the focused beam 2 mm along the sample.

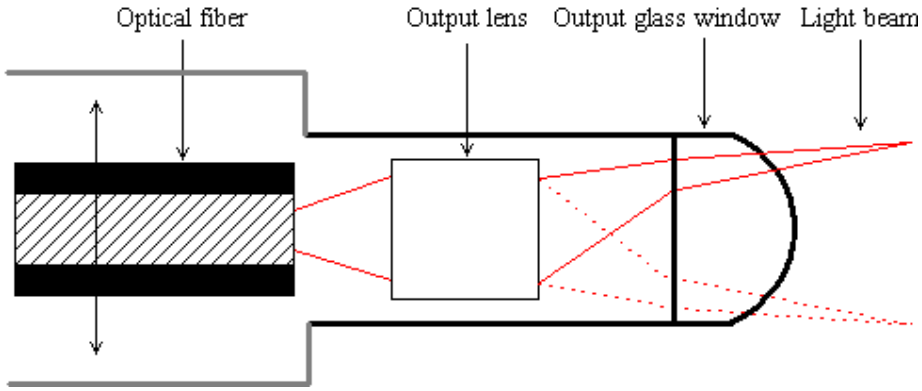

Figure 4.2: The deflecting probe

In addition, the light beam can be deflected with galvanometer-driven scanning mirror in the sample probe. A recently reported hand-held sample probe is shown in Figure 4.3 [100]. It contains a X-Y two-axis scanning mirror that can change the incidence angle of the incoming light beam in a stationary assembly of relay lens (Hopkins type). This design is simple and makes use

of the translational principle of scanning. It can extend the working distance and operate conveniently using the theory of Hopkins relay lens which confines the chief ray bundle more tightly to the optical axis by reducing the ray divergence. Incorporation of a two-axis scanning mirror in this sample probe provides the time-domain OCT system 3D rapid imaging capability. So it may be applied in biological fields and be used to monitor the dynamic progress of biological experiments. 3D real-time data may be obtained to help biologists understand biological phenomena more thoroughly. In this project, we will use this sample probe for the OCT system and detailed analysis will be given later.

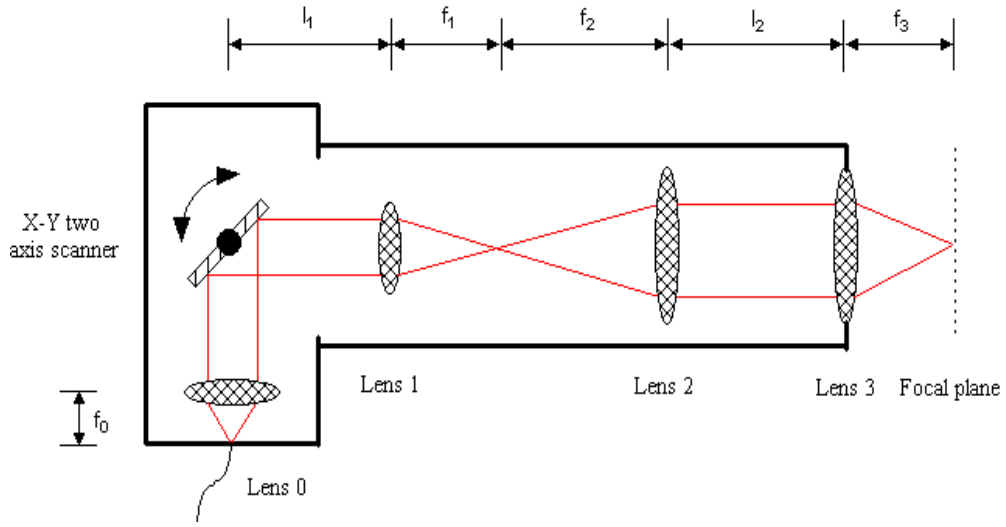

Figure 4.3: Hand-held sample probe

In the translational probe, the focusing light beam will be controlled to move along the probe axis. This can be realized by translational motion of optical fiber and focusing lens using motor or galvanometer. A typical design is shown in Figure 4.4 [101]. A galvanometer is connected to a linearly translating carriage. The optical fiber will be fixed to the carriage. GRIN lens and prism will be placed static to the optical fiber. When the galvanometer rotates, the carriage will be

linearly translated and attached optical fiber will be stretched or compressed. So the focusing beam will be translated along the probe axis. This kind of sample probe will have minimal image aberration.

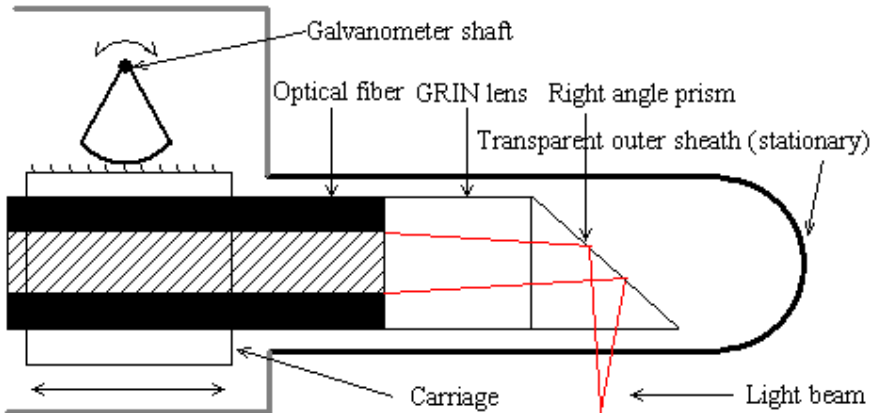

Figure 4.4: The translational probe

4.2Ray tracing analysis of the sample probe

To investigate the sample probe shown in Figure 4.3, ray tracing analysis was employed to analyze the relay optics of the sample probe. The inner relationship between positions of lens 1 and lens 2 has been derived and obtained. This analysis will help to configure the optics components of sample probe.

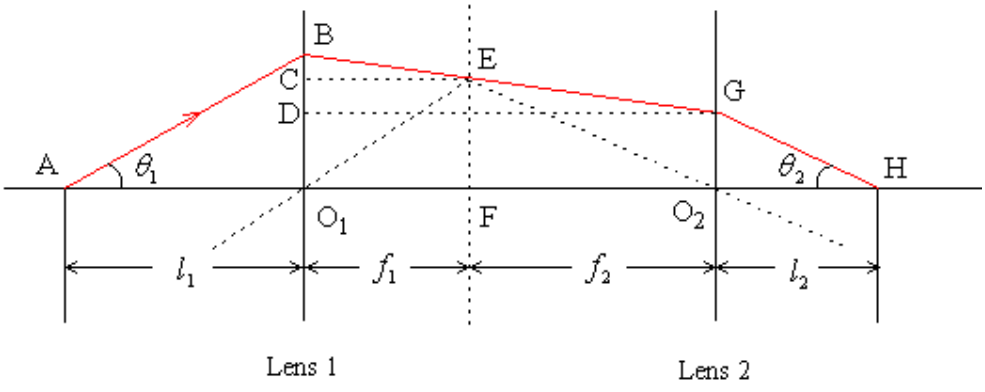

Figure 4.5: Ray tracing analysis of relay optics in the sample probe

The schematic of ray tracing analysis for the sample probe is shown in Figure 4.5.

Let $\overline{AO_1} = l_1$, $\overline{O_1F} = f_1$, $\overline{FO_2} = f_2$, $\overline{O_2H} = l_2$.

From the plane geometry in the figure, the following two equations may be obtained

$$\frac{\overline{EF}}{f_1} = tg(q_1), \quad \frac{\overline{EF}}{f_2} = tg(q_2)$$

$$\Rightarrow \quad f_1 \cdot tg(q_1) = f_2 \cdot tg(q_2) \tag{4.1}$$

Now $\frac{\overline{BC}}{\overline{BD}} = \frac{\overline{BE}}{\overline{BG}} = \frac{\overline{O_1F}}{\overline{O_1O_2}}$,

$$\Rightarrow \quad l_1 \cdot tg(q_1) - \frac{l_1 \cdot tg(q_1) - f_1 \cdot tg(q_1)}{f_1}(f_1 + f_2) = l_2 \cdot tg(q_2) \tag{4.2}$$

Combining equations (4.1) and (4.2), we have

$$l_1 \cdot tg(q_1) - l_1 \cdot tg(q_1) + f_1 \cdot tg(q_1) - \frac{f_2}{f_1}(l_1 \cdot tg(q_1) - f_1 \cdot tg(q_1)) = l_2 \frac{f_1 \cdot tg(q_1)}{f_2}$$

$$f_1 - \frac{f_2}{f_1} l_1 + f_2 = l_2 \frac{f_1}{f_2}$$

$$f_1 + f_2 = \frac{f_2}{f_1} l_1 + \frac{f_1}{f_2} l_2 \tag{4.3}$$

Equation (4.3) gives the important relationship between lens 1 and lens 2. If $f_1 = f_2$, then total length $\overline{AH}$ is

$$\overline{AH} = l_1 + l_2 + f_1 + f_2 = 4 f_1 \tag{4.4}$$

If $f_2 = 2 f_1$, then

$$3 f_1 = 2 l_1 + 0.5 l_2 \tag{4.5}$$

$$\Rightarrow \quad \overline{AH} = l_1 + l_2 + f_1 + f_2 = 9 f_1 - 3 l_1 \tag{4.6}$$

Based on the design and ray tracing analysis of the sample probe, the relevant optical components have been purchased and fabricated.

Component list for the sample probe of our OCT system:

Lens 0: AC127-019-B (Thorlabs)

Lens 1: AC127-025-B (Thorlabs)

Lens 2: AC254-050-B (Thorlabs)

Lens 3: AC254-035-B (Thorlabs)

Two-axis scanning mirror: 6210H (Cambridge Technology).

The following parameters were chosen:

f_0 =19 mm, f_1 =25 mm, f_2 =50 mm, f_3 =35 mm, l_1 =25 mm, l_2 =50 mm, $\overline{AH}$ =150 mm.

4.3 Optical implementation of the sample probe

Optics alignment experiments of the sample probe were performed using a piece of glass (1 mm thick) as the sample. Experimental results showed that broad-band spectrum of light source can be reflected and reconverged back into OCT system. However, the positions of the lenses inside the sample probe can affect the shape of back spectrum. Their slight displacements will lead to the translation of the focal plane of the sample probe and have considerable effect on the back spectrum.

We systemically investigated their effects on the performance of the sample probe. Four parameters were studied: (1) The position of lens 0 f_0, (2) The position of lens 1 f_1, (3) The position of lens 2 f_2, and (4) The position of lens 3 f_3. The tolerances of these parameters were quantitatively estimated based on the criteria that: the fluctuation of the intensity of spectrum within the tolerance is within 10%. These values provide a valuable guide in the fabrication of the sample probe.

4.3.1 The position of lens 0 f_0

Align the optics well, and then move lens 0 to change the distance f_0, while the spectrum going back into OCT system was recorded. These spectra were analyzed, and the area, centroid and FWHM were calculated as shown in Figures 4.6, 4.7, 4.8. The experimental results show that

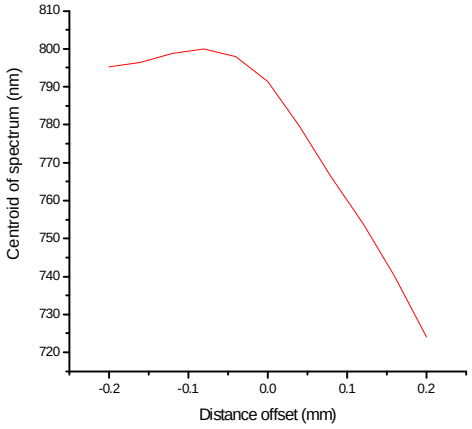

Figure 4.6: Centre of spectrum at different distance offset

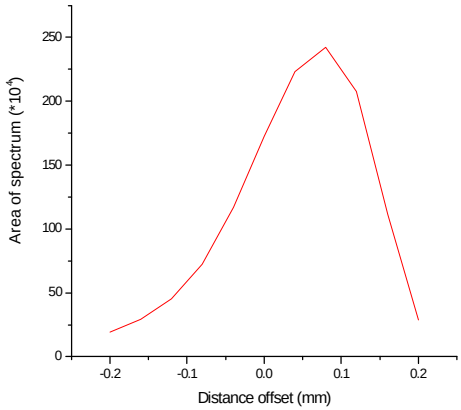

Figure 4.7: Area of spectrum at different distance offset

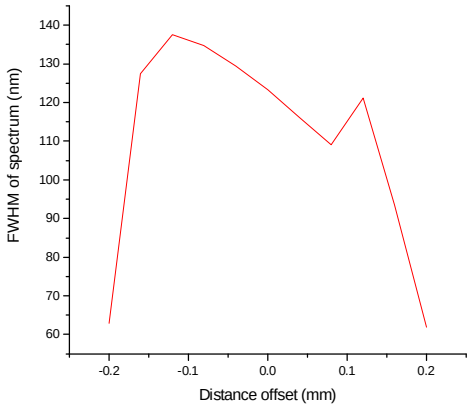

Figure 4.8: FWHM of spectrum at different distance offset

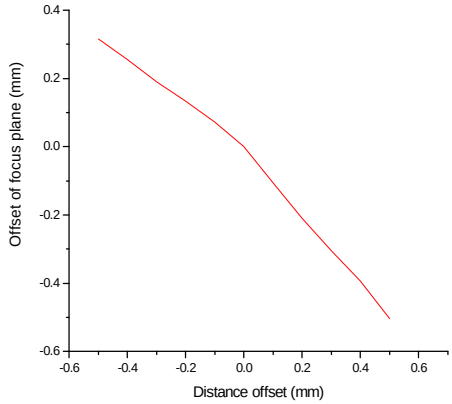

Figure 4.9: Offset of focal plane at different distance offset

the shape and intensity of spectra were greatly affected by offset of the distance f_0. The main reason is that small offset of the distance f_0 has caused the translation of focal plane of the

sample probe. The relationship between offset of focal plane and offset of f_0 has been investigated and the result is shown in Figure 4.9. A 0.1 mm offset increase can cause the focal plane to go back about 0.1 mm. However, a 0.1 mm offset decrease causes the focal plane to go forward about 0.06 mm.

For different offsets of the distance f_0, the sample was moved to the focal plane of the

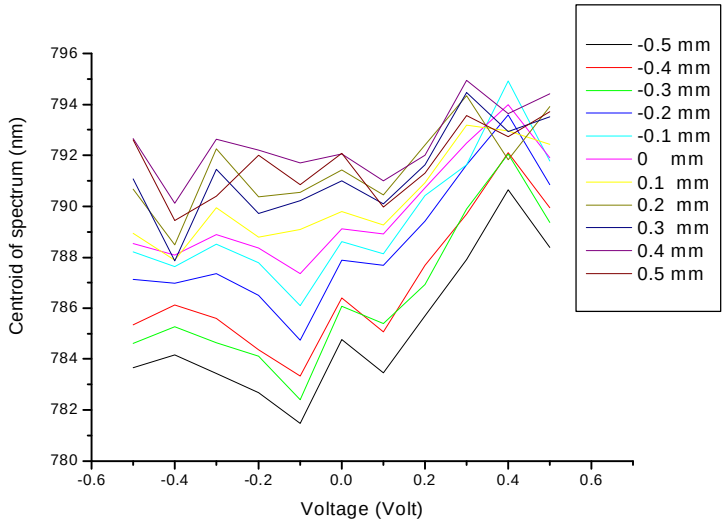

Figure 4.10: Centre of spectrum when scanning mirror rotates

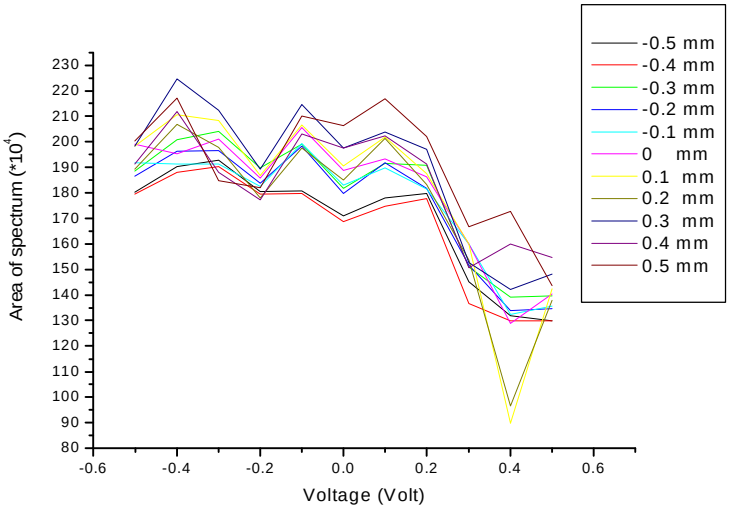

Figure 4.11: Area of spectrum when scanning mirror rotates

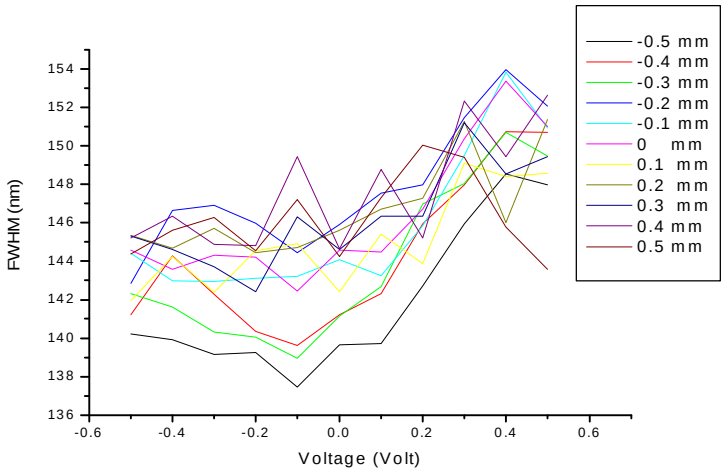

Figure 4.12: FWHM of spectrum when scanning mirror rotates

sample probe and the light source can be focused on the surface of the sample. The scanning mirror was controlled to rotate symmetrically and the relevant sequences of spectra were acquired. These spectra have been analyzed as shown in Figures 4.10, 4.11, 4.12. Experimental results show that these spectra have nearly the same changing trend at different distance offsets. In Figure 4.11, it can be seen that the tolerance for f_0 can be set to 0.1mm. The fluctuation of the intensity of spectrum within this tolerance will be below 10%. In addition, the offset within this tolerance does not cause obvious translation of the focal plane.

4.3.2 The position of lens 1 f_1

The tolerance for offset of the distance f_1 has been measured using the same method. When moving lens 1 and keeping the sample static, the area, centroid and FWHM of back spectrum have been calculated as shown in Figures 4.13, 4.14, 4.15.

The experimental results have shown that the shape and intensity of spectra were greatly affected by the distance f_1. The main reason is that small offset of the distance f_1 has caused the translation of focal plane of the sample probe. The relationship between offset of focal plane

and offset of f_1 has been investigated and the result is shown in Figure 4.16. A 0.1 mm offset of f_1 can cause about 0.04 mm offset of the focal plane.

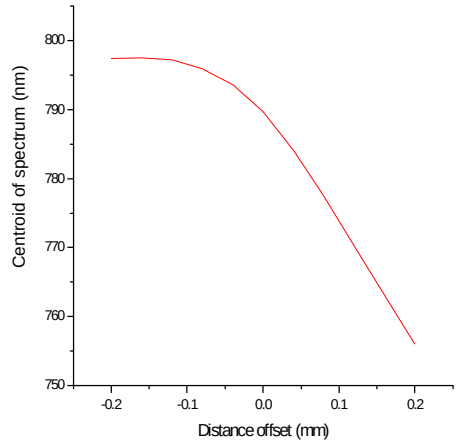

Figure 4.13: Centre of spectrum at different distance offset

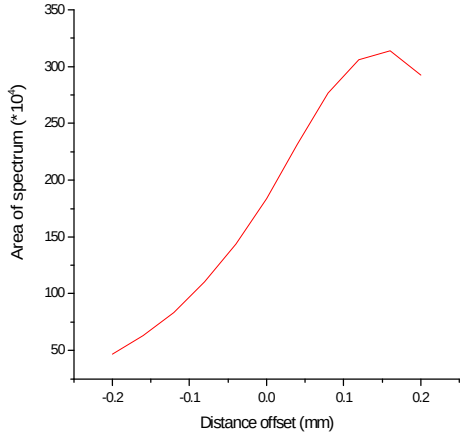

Figure 4.14: Area of spectrum at different distance offset

The relevant sequences of spectra were acquired when the scanning mirror was controlled to rotate symmetrically. These spectra have been analyzed as shown in Figures 4.17, 4.18, 4.19. Experimental results show that these spectra have nearly the same changing trend at different

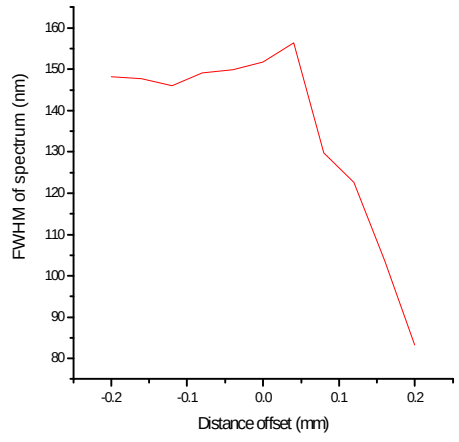

Figure 4.15: FWHM of spectrum at different distance offset

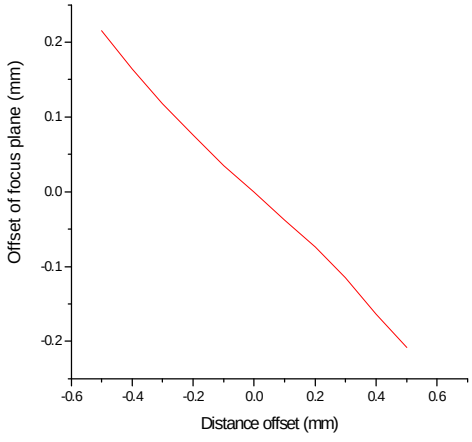

Figure 4.16: Offset of focus plane at different distance offset

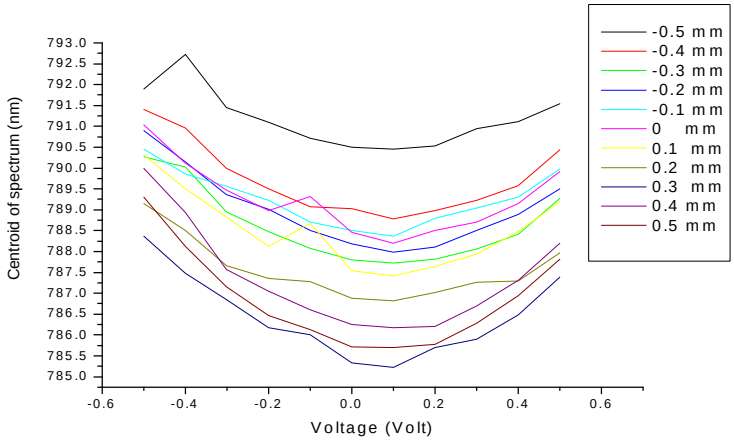

Figure 4.17: Centre of spectrum when scanning mirror rotates

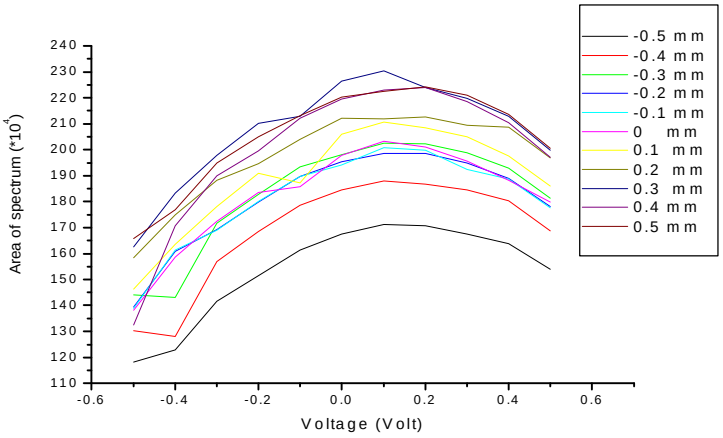

Figure 4.18: Area of spectrum when scanning mirror rotates

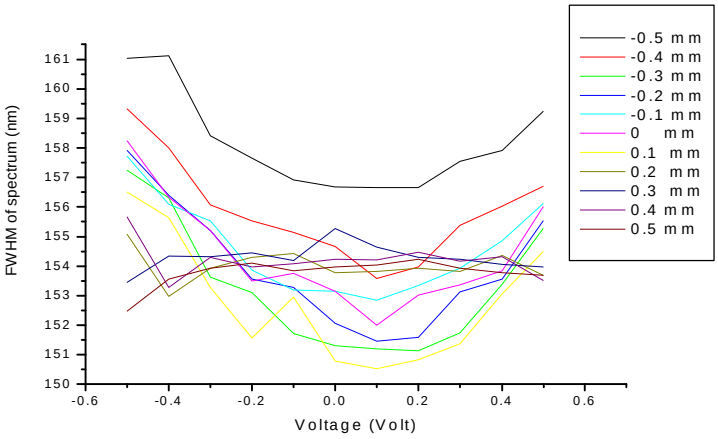

Figure 4.19: FWHM of spectrum when scanning mirror rotates

distance offsets. In Figure 4.18, it can be seen that the tolerance for f_1 can be set to 0.1mm. The fluctuation of the intensity of spectrum within this tolerance will be below 10%. In addition, the offset within this tolerance does not cause obvious translation of the focal plane.

4.3.3 The position of lens 2 f_2

The tolerance for offset of the distance f_2 has been measured using the same method. When moving lens 2 and keeping the sample static, the area, centroid and FWHM of back spectrum have been calculated as shown in Figures 4.20, 4.21, 4.22.

The experimental results have shown that the shape and intensity of spectra have been greatly affected by the distance f_2. The main reason is that small offset of the distance f_2 has caused the translation of focal plane of the sample probe. The relationship between offset of focal plane and offset of f_2 has been investigated and the result is shown in Figure 4.23. A 0.1 mm offset increase can cause the focal plane to go back about 0.05 mm. However, a 0.1 mm offset decrease can cause the focal plane to go forward about 0.04 mm.

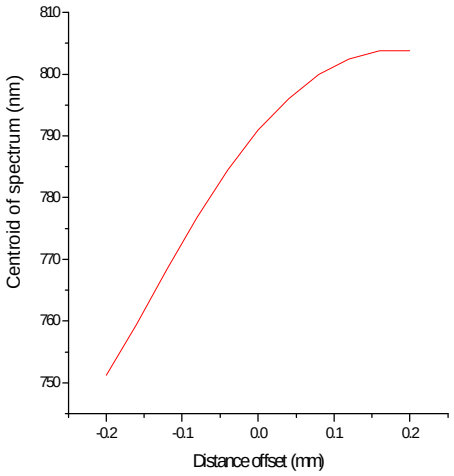

Figure 4.20: Centre of spectrum at different distance offset

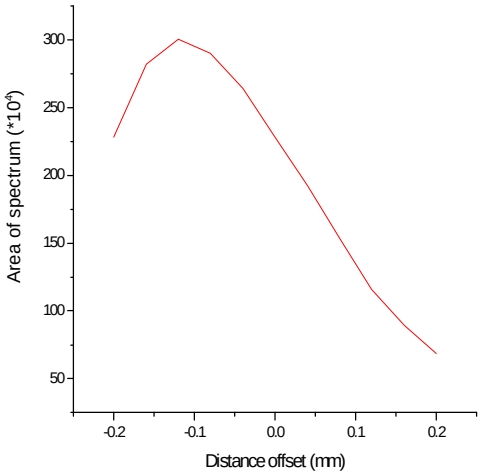

Figure 4.21: Area of spectrum at different distance offset

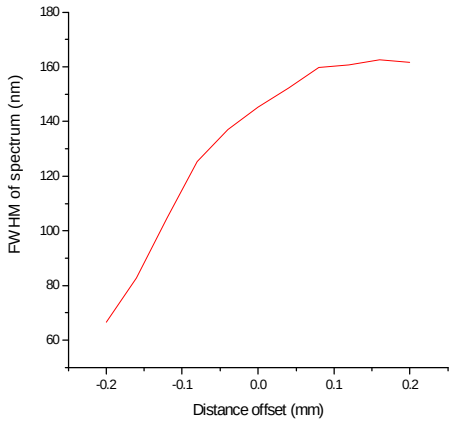

Figure 4.22: FWHM of spectrum at different distance offset

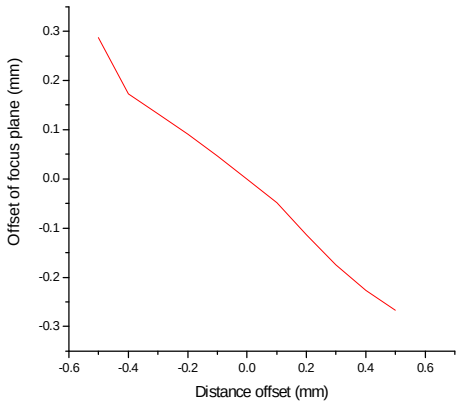

Figure 4.23: Offset of focus plane at different distance offset

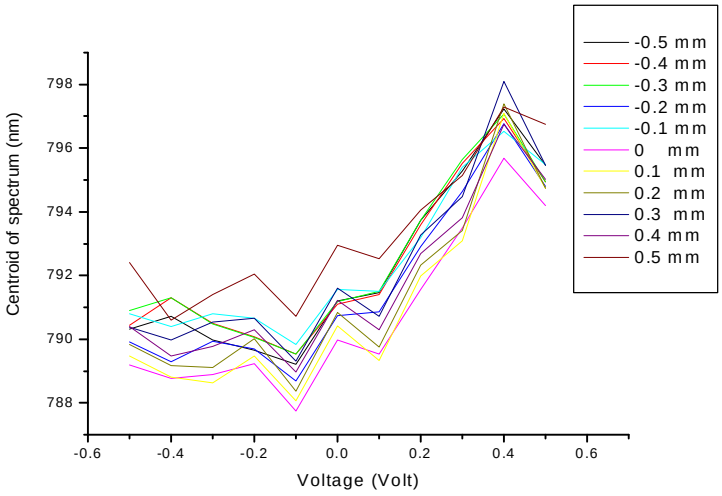

Figure 4.24: Centre of spectrum when scanning mirror rotates

The relevant sequences of spectra were acquired when the scanning mirror was controlled to rotate symmetrically. These spectra have been analyzed as shown in Figures 4.24, 4.25, 4.26. Experimental results show that these spectra have nearly the same changing trend at different distance offsets. In Figure 4.25, it can be seen that the tolerance for f_2 can be set to 0.1 mm. The fluctuation of the intensity of spectrum within this tolerance will be below 10%. In addition, the

offset within this tolerance does not cause obvious translation of the focal plane.

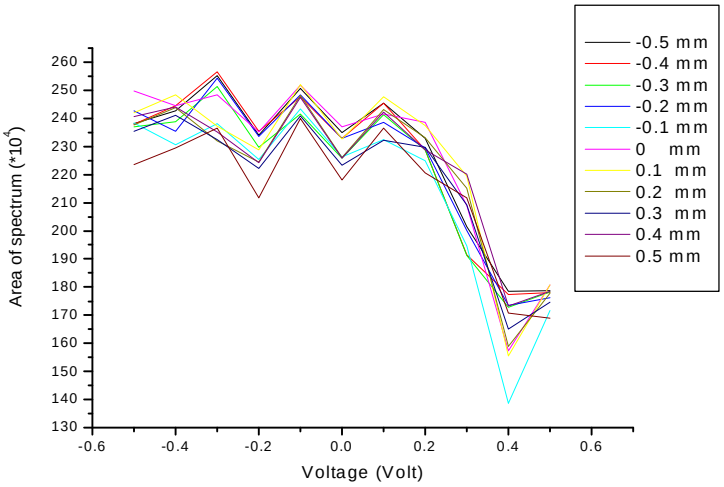

Figure 4.25: Area of spectrum when scanning mirror rotates

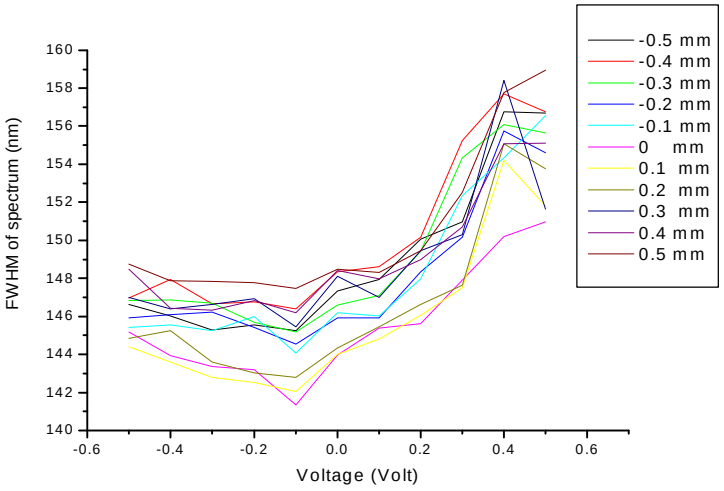

Figure 4.26: FWHM of spectrum when scanning mirror rotates

4.3.4 The position of lens 3 f_3

The tolerance for offset of the distance f_3 has been measured using the same method. When moving lens 3 and keeping the sample static, the area, centroid and FWHM of back spectra were calculated as shown in Figures 4.27, 4.28, 4.29. The experimental results have shown that the

shape and intensity of spectrums have been greatly affected by the distance f_3. The main reason is that small offset of the distance f_3 has caused the translation of focal plane of the sample probe. The relationship between offset of focal plane and offset of f_3 was investigated and the result is shown in Figure 4.30. A 0.1 mm offset of f_3 can cause about 0.1 mm offset of the focal plane. The focal plane will go forward or backward when offset of the distance f_3 increases or decreases.

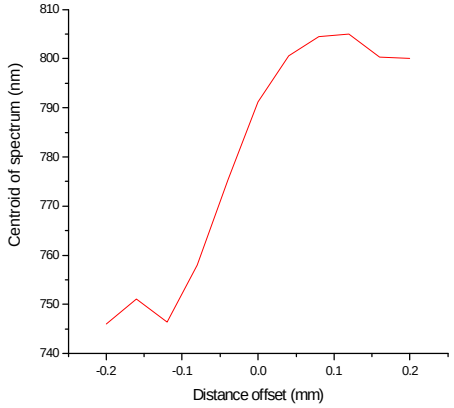

Figure 4.27: Centre of spectrum at different distance offset

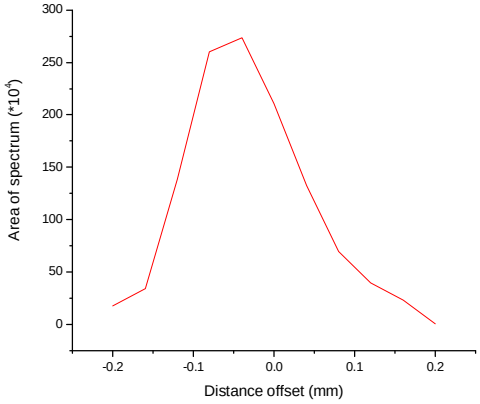

Figure 4.28: Area of spectrum at different distance offset

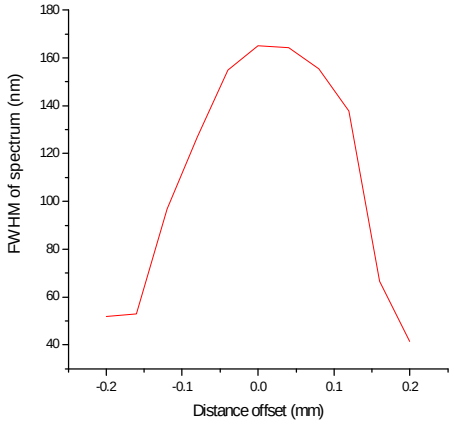

Figure 4.29: FWHM of spectrum at different distance offset

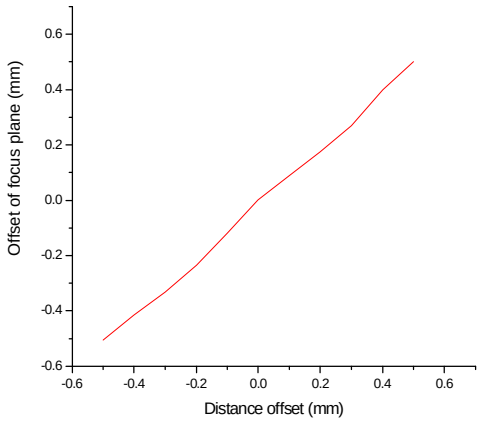

Figure 4.30: Offset of focus plane at different distance offset

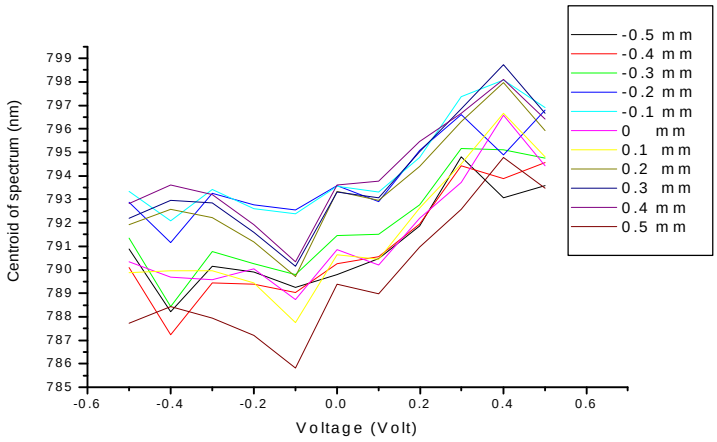

Figure 4.31: Centre of spectrum when scanning mirror rotates

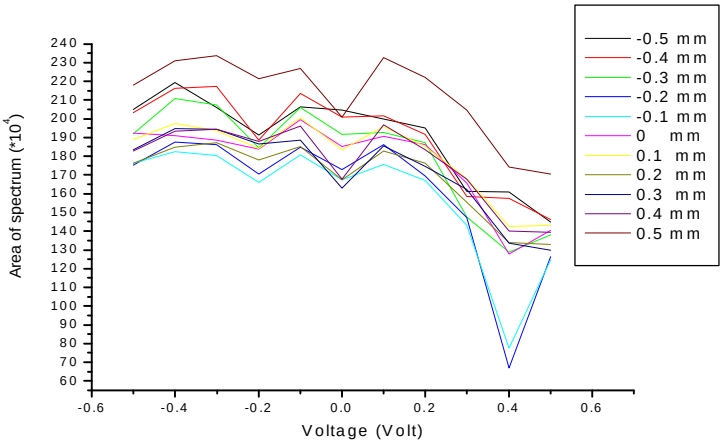

Figure 4.32: Area of spectrum when scanning mirror rotates

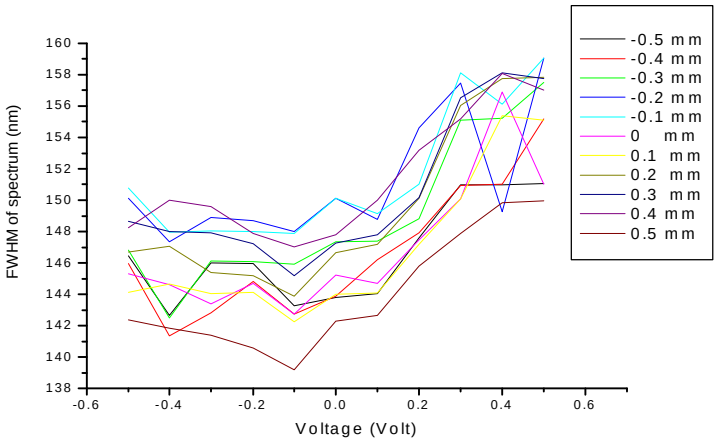

Figure 4.33: FWHM of spectrum when scanning mirror rotates

The relevant sequences of spectra were acquired when the scanning mirror was controlled to rotate symmetrically. These spectra have been analyzed as shown in Figures 4.31, 4.32, 4.33. Experimental results show that these spectra have nearly the same changing trend at different distance offset. In Figure 4.32, it can be seen that the tolerance for f_3 can be set to 0.1 mm. The fluctuation of the intensity of spectrum within this tolerance will be below 10%. In addition, the offset within this tolerance does not cause obvious translation of the focal plane.

4.4 The OCT system properties related to sample probe

4.4.1 The transverse resolution of the OCT system

One of the apparent advantages of the OCT system is that the transverse resolution is completely de-coupled from the axial resolution. The axial resolution is defined by the coherence length and depends on the bandwidth of the light source, whereas transverse resolution depends on the minimum waist radius w_0 of the focused (Gaussian) probe beam. Therefore, the optical design of sample probe of the OCT system can be optimized for lateral scanning, with no effect on the axial resolution.

Using the Gaussian approximation, the beam intensity profile focusing on the sample can be described as [102]

$$I(r,z) = \frac{2}{pw^2}\exp(-\frac{2\cdot r^2}{w^2}) \tag{4.7}$$

where r is the distance from the beam axis and w is the $1/e^2$ beam radius.

$$w = w_0\sqrt{1+\frac{z^2}{b^2}} \tag{4.8}$$

where b is the confocal parameter. w_0 is the beam waist at the focus and can be given as

$$w_0 = \frac{2l_0}{p}(\frac{f}{D}) = \frac{l_0}{p\cdot NA} = \sqrt{\frac{bl_0}{p}} \tag{4.9}$$

where l_0 is the center wavelength of the light source, f is the focal length of the focusing lens 3, D is the diameter of the input beam. NA is the numerical aperture of the lens 3. It is obvious that a large NA focusing lens will have a small beam waist radius and can achieve high transverse resolution as shown in Figure 4.34.

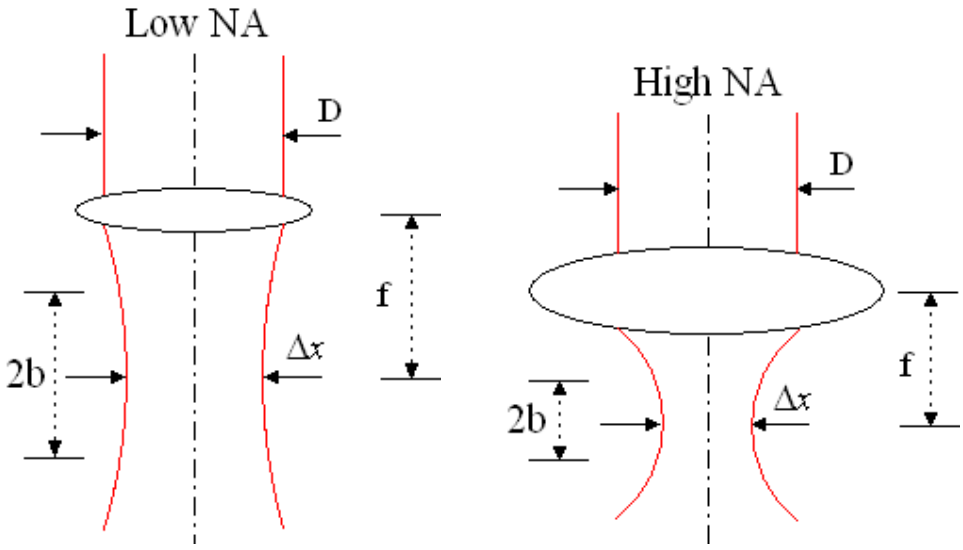

Figure 4.34: Schematic of different NA focusing lens

The transverse resolution Δx of OCT system can be defined in analogy to axial resolution as the FWHM diameter of the probe beam amplitude distribution at the beam waist of the focused probe beam. It can be found by setting

$$\frac{I^2(r,0)}{I^2(0,0)} = \exp(-\frac{4 \cdot r^2}{w_0{}^2}) = \frac{1}{2} \tag{4.10}$$

Then Δx can be solved as

$$\Delta x = 2r = \sqrt{\ln 2} w_0 \tag{4.11}$$

4.4.2 The depth of field (DOF) of the OCT system

DOF is an important parameter of the OCT system that must be considered in optical design, over which the optical beam remains in focus. The FWHM depth of field can be found by setting

$$Ratio = \frac{\int_0^{\infty} I^2(r,z)dr}{\int_0^{\infty} I^2(r,0)dr} = \frac{1}{1+\frac{z^2}{b^2}} \tag{4.12}$$

$Ratio = 0.5$, then DOF can be solved as,

$$DOF = 2z = 2b \tag{4.13}$$

From equations (4.9), (4.11), (4.13), DOF is related to the transverse resolution Δx of the OCT system and can be given as

$$DOF = \frac{2p \cdot \Delta x^2}{\ln 2 \cdot l_0} \tag{4.14}$$

It is a specific problem in OCT system that DOF depends on transverse resolution. Increasing the transverse resolution will lead to the decrease of DOF. For example, a transverse resolution of Δx =20 mm at a centre wavelength of l_0 =800 nm leads to DOF=4.532 mm, whereas a transverse resolution of Δx =2 mm leads to DOF= 45.32 mm. The simulation result relating DOF and transverse resolution is shown in Figure 4.35. It can be seen that transverse resolution $\Delta x < 5mm$ will limit DOF significantly. Hence, a compromise has to be found between a desired transversal resolution and the available DOF for the OCT system.

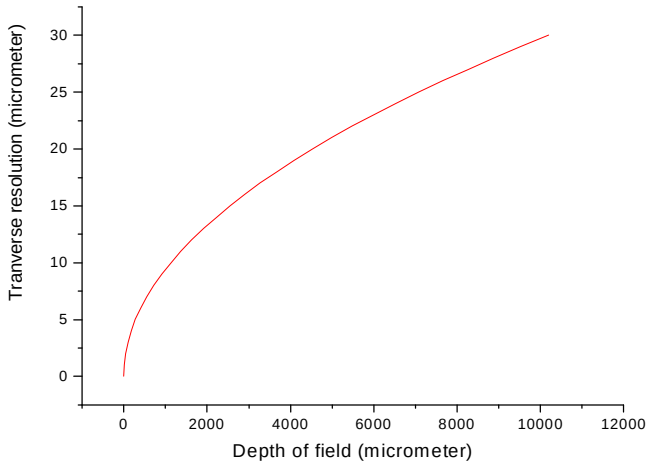

Figure 4.35: Transverse resolution versus depth of field for wavelength l_0 =800nm

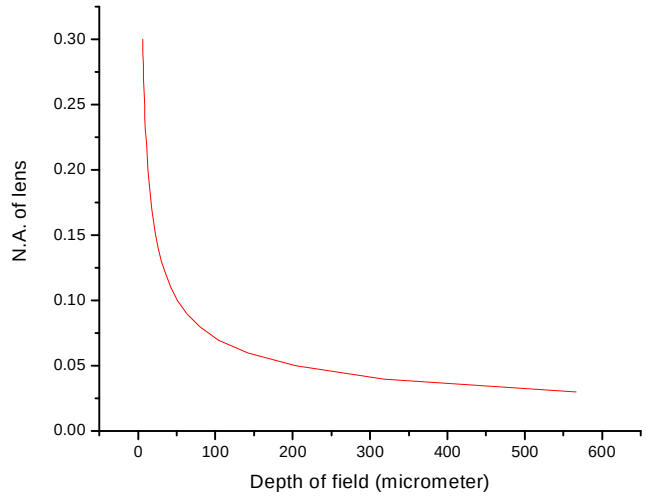

Figure 4.36: N.A. of lens versus depth of field for wavelength l_0 =800nm

In addition, from equations (4.9), (4.11), (4.13), DOF can be related to NA of the focusing lens and may be given as

$$DOF = \frac{2 \cdot l_0}{p \cdot (NA)^2} \tag{4.15}$$

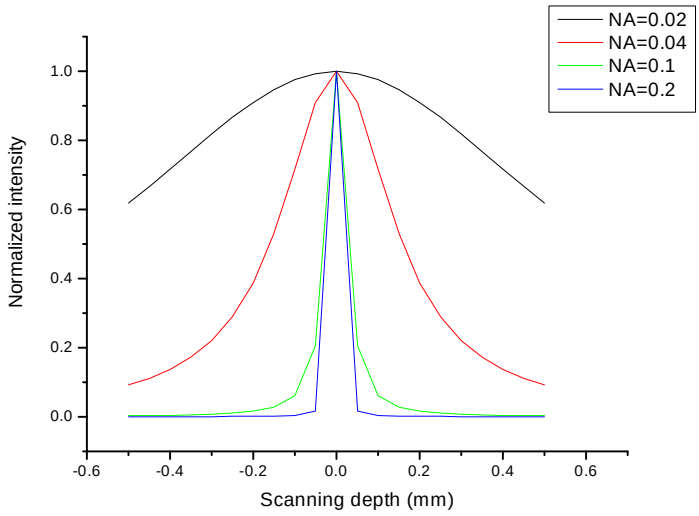

Figure 4.37: Reflected intensity at different scanning depths using different NAs

The simulation result relating DOF and N.A. of the focusing lens is shown in Figure 4.36. It can be seen that $NA < 0.04$ ($\Delta x > 5.3 \ \ mm$) would limit DOF significantly.

The intensity of reflected light may be calculated using equation (4.12). It can be rewritten as

$$Ratio = \frac{1}{1 + \frac{p^2 \cdot NA^4 \cdot z^2}{l_0^2}} \tag{4.16}$$

For focusing lens of different NAs, the relationship between the reflected intensity and the distance from focusing plane are described in equation (4.16). The simulation results are shown in Figure 4.37.

4.4.3 Solutions to overcome the limitations of DOF

In order to obtain larger imaging depth of focus within the tissue, the focusing beam of the sample arm is positioned at the centre of the imaging path. This method can maintain relatively good transversal resolution throughout the imaging depth. However, in case of thick tissues, this method needs a small NA focusing lens and will lead to poor transversal resolution.

To overcome the limitations of DOF while still maintain good transversal resolution along the imaging depth of thick tissues, different methods have been proposed recently: (1) Dynamic focus tracking strategy [103-106]. Special optical setup has been incorporated into the system that dynamically shifts the focus plane without changing the path length of sample arm. (2) Image fusion strategy [63]. Fix the object and shift the focusing lens, or fix the focusing lens and shift the object in steps of say, 100 micrometers, whence several images can be obtained sequentially along the imaging depth. Image fusion technique is then used to integrate them as one new image.

In this project, we will use image fusion strategy and integrate current time domain OCT system with commercial Olympus® Inverted Microscopy IX71. The sample arm will be replaced by the worktable part of IX71 (shown in Figure 4.38). The basic idea of integration method is shown in Figure 4.39. The parallel light will be directed to the two-axis scanning mirror and focused onto the worktable by the objective. The main advantages include: (1) It is convenient to put biological samples on the worktable of IX71 and facilitate operation of OCT system. The

biological experiments can be easily carried out by biologists. (2) Several successive OCT images can be easily obtained by shifting the focal plane of the objective with steps of about 100 micrometers, and then image-fusion technique can be used to combine them into a new image. This will overcome depth-of-field limitation and maintain high transverse resolution at different depths. Dynamic focus tracking technique can also be used to maintain high transverse resolution at different focal depths, but this technique requires a rapid scanning mechanism to move focal plane of the sample arm.

Figure 4.38: Inverted microscope IX71

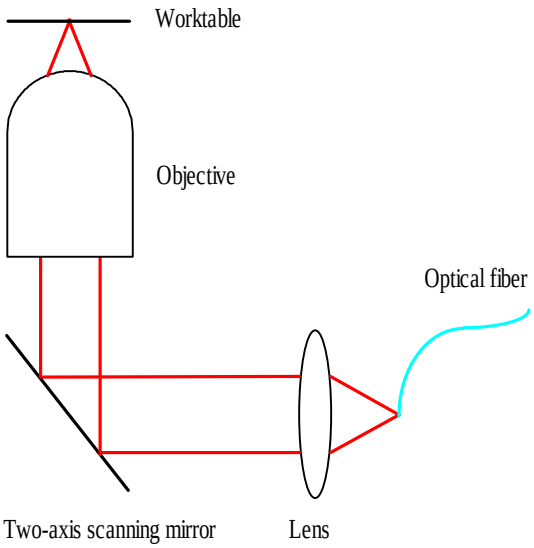

Figure 4.39: Schematic figure of coupling path

4.4.4 The control of the contrast of OCT image

From the simulation result shown in Figure 4.34, it can be seen that although a focusing lens of very small NA, for example 0.04 is used, the reflected intensity from the sample will decrease considerably when the scanning depth is away from the focusing plane. This will lead to a great variation in the contrast of the OCT image. The intensity of the OCT image of focusing plane is correspondingly high; however the intensity of other planes is very low.

Compared to the spectrum from the sample probe, the amplitude of the spectrum from FD_ODL is relatively stable as shown in Figure 3.60. Amplitude contrast of OCT system can be

controlled to some extent by moving the focal plane of the focusing lens forward or backward by 0.5 mm. This would allow the light from the focal plane of the focusing lens to interfere with the light from a scanning depth of 0.5 mm in FD_ODL. However, this method would have to sacrifice half of the scanning depth of OCT system.

4.4.5 The lateral scanning of the sample probe

The scanning rate is one of important design issues of the sample probe. The speed of lateral scanning is typically about 0.1-8 frames per second (fps) and can be controlled by the galvanometer. The lateral displacement during one period of A-scan should be kept 1.5-2 times less than the transverse resolution of the OCT system. Insufficient transverse sampling rate will degrade the transverse resolution of the OCT system.

4.5 Conclusions

In our time-domain OCT system, the sample probe has been designed as shown in Figure 4.3. Geometric ray tracing analysis method has been employed to analyze the relay optics of the sample probe. Some relationship equations have been derived to set up relevant optics components. A two-axis scanning mirror was incorporated into the sample probe, which provides the OCT system 3D real-time imaging capability.

To allow broad-band spectrum of light source can go back into the OCT system, the optics implementation of sample probe was investigated. Experimental results show that the slight position displacements of the lens would lead to the translation in focal plane of the sample probe. The reflected-back spectrum from the focal plane is not very sensitive to the position offset of the lens. The fabrication accuracy for them should be at least 19 ± 0.1 mm, 25 ± 0.1 mm, 50 ± 0.1 mm, 35 ± 0.1mm separately.

The transverse resolution of OCT system is related to the sample probe, while a large NA focusing lens can achieve high transverse resolution, it would decrease the depth of field significantly. Therefore, an appropriate focusing lens should be used to provide a desired transverse resolution and the available depth of field for the OCT system.

Chapter 5 OCT image analysis

5.1 Background

OCT is a relatively new non-invasive imaging technique that provides both high spatial resolution and cross-sectional imaging capability. It is analogous to ultrasound except that near-infrared back-reflected light is detected rather than sound. As it can achieve micro scale resolution with penetration depth of a few millimeters, it has become a particularly useful imaging tool in several biological fields, such as ophthalmology and tissue engineering.

In the case of ophthalmology, OCT systems have been used to investigate the 3-D structure of the whole eye, from the anterior to the posterior of the lens, the retina, and so on. Some ocular diseases are often related with the morphological change of some part of the eye. For instance, glaucoma disease leads to progressive loss of ganglion cells and axons in the retinal nerve fiber layer (RNFL). Segmentation of retinal layers from OCT images and quantitative thickness measurements of RNFL are important to diagnose the progress of glaucoma disease. The quantitative ability of OCT system is an important factor in ocular disease research [107-114].

In tissue engineering, OCT system has been used to monitor cell dynamics in four dimensions (3-D space plus time). A variety of cell processes, such as migration, proliferation, and cell-material interactions can be quantified using suitable image analysis algorithms. These quantitative results can efficiently estimate the effects of biological experiments [37].

However, a large quantity OCT images are often acquired in the experiments. Manual segmentation methods will be slow for their analysis and the results are subject to the operator's variabilities and have no repeatability. It is highly desirable to develop specific, automatic methods to segment OCT images.

5.2 Denoising of OCT images

Noise is a complicated problem in the practical OCT system; it will degrade the contrast of images and obscure microscopic features evident in biological tissues. Speckle noise is the main noise source in OCT system which exists in coherence imaging techniques. As shown in Figure 5.1, multiple backscattering and forward scattering within the dense sample volume alter the shape of the wave front and influence the spatial coherence of the returning wave [115]. In biological tissue, a sample volume contains lots of scatterers, such as cells, organelles, fibers, and fluids.

Speckle forms when light wave from these scatterers or returning wave caused by multiple forward scattering reaches the detector out of phase within the coherence time of the source.

As speckle noise is nonlinear and signal dependent, it can not be removed easily from the signal. It remains when OCT images are formed and complicates some important segmentation tasks of OCT images. In order to suppress the speckle noise and smooth images, some filters have been used for this purpose, such as the Gaussian filter and median filter. However, these conventional filters usually have some limitations. (1) Filters are limited by the filter window. A filter window that is too large will lead to over-smoothing and blurred edges, while a small window filter will have no obvious smoothing effect. (2) Filters only inhibit smoothing near edges and do not enhance edges. (3) Filters are not directional. For noisy images these methods often give poor results and the filtered images are either blurred or over smoothed due to the loss of edge details.

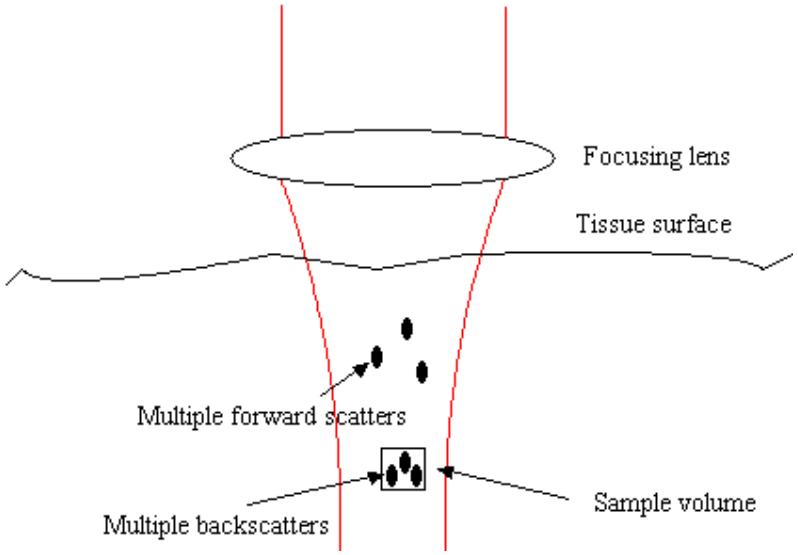

Figure 5.1: Multiple forward scatters and multiple backscatters in the sample volume

5.2.1 Nonlinear PDE-based approaches

Recently image modeling denoising method based on partial differential equations (PDEs) has been widely used [116-127]. Its main advantage is to suppress noise while at the same time preserving the edge details. It can be anisotropic and irrelevant to filter window size and shape. It is particularly suitable for suppressing additive noise.

In a PDE based model, the desired noiseless image $u(x)$ can be taken as the solution of an evolutionary differential equation $u_t(x)$ and the true solution will be reached when $t \to \infty$. In

practical applications we should stop the time "t" at some moment T during this evolutionary process such that $u_T(x)$ is a good approximation of $u(x)$. Different models have been presented in some literatures. Their common points are the considerations of evolution of PDE as a time parameter "t" and the establishment of dynamic data structures which allow modifying the image with the PDE. As some parameters exist in these models and they are related to the initial image and the level of noise, it is not easy to solve these models. When the time scale "t" evolves, an optimal stop time T can be obtained which gives good denoising effects and low computational cost.

In this chapter, we will discuss applications of some nonlinear PDE-based approaches on the denoising of OCT images. The nonlinear diffusion method was first reported by Perona and Malik. They suggested to construct nonlinear multi-scale space to describe images under below criteria [116].

(1) Causality: no spurious detail should be generated in passing from finer to coarser scales.

(2) Immediate localization: boundaries should be sharp and coincide with the semantically meaningful boundaries at that resolution.

(3) Piecewise smoothing: intraregion smoothing should occur preferentially over interregion smoothing.

So the diffusion process can be related to the local image characteristics by introducing a space- and time-variant diffusion coefficient $c(x, y, t)$, and they formulated the following nonlinear diffusion equation:

$$\frac{\partial I(x, y; t)}{\partial t} = \mathrm{div}[c(x, y, t) \cdot \nabla I] \tag{5.1}$$

where div is the divergence operator and ∇ is the gradient operator. The boundary condition is: $I(x, y; 0) = I_0(x, y)$.

5.2.1.1 Perona-Malik (PM) filter [116]

They proposed that $c(x, y, t)$ is chosen as the monotonically decreasing function of the gradient magnitude of an image I, $\|\nabla I\|$. $\|\nabla I\|$ is used to estimate the position of edges. If $\|\nabla I\|$ is small, there is a minor probability of an edge at that position, and $c(\|\nabla I\|)$ is close to 1.

However, if $\|\nabla I\|$ is large, the location is likely to belong to an edge, and the value of $c(\|\nabla I\|)$ is close to zero. They proved that this filter can satisfy the three scale-space criteria and give good diffusion results. If $c(\|\nabla I\|)$ is constant, then this filter reduces to isotropic diffusion.

The isotropic diffusion process diffuses the image equally in all directions. It can remove undesirable noise, but many important features of the image, such as edges and corners, are blurred. This will make edge detection and localization difficult. To overcome these drawbacks, nonlinear diffusion offers a good solution. The diffusivity function is a monotonically decreasing function of the gradient magnitude. So regions with large gradient magnitudes have weak diffusion process, while regions with small gradient magnitudes have strong diffusion process. This leads to the improved filtering effect of structure preservation (or even enhancing) and image denoising. Perona and Malik suggested two diffusivity functions,

$$c_1(\|\nabla I\|) = \frac{1}{1+(\|\nabla I\|/k)^2} \tag{5.2}$$

$$c_2(\|\nabla I\|) = \exp[-(\|\nabla I\|/k)^2] \tag{5.3}$$

where k is a constant and acts as the gradient threshold. It can control the degree of smoothing in the diffusion process and should be fine-tuned for practical applications. Equation (5.2) favours high-contrast edges over low-contrast ones. However, equation (5.3) favours wide regions over smaller ones.

Quite a few diffusion coefficients have been proposed in the research literature over the past decade. Different variations have been proposed and applied successfully in image denoising. In this chapter, we will compare some classical nonlinear diffusion approaches, such as speckle reducing anisotropic diffusion and nonlinear complex diffusion, and evaluate their denoising performance on OCT images.

5.2.1.2 Speckle Reducing Anisotropic Diffusion (SRAD) [120]

The output image $I(x,y;t)$ evolves according to the following PDE:

$$\partial I(x,y;t)/\partial t = \mathrm{div}[c(q)\nabla I(x,y;t)] \tag{5.4}$$

The bounded condition is $I(x,y;0) = I_0(x,y)$; $(\partial I(x,y;t)/\partial \mathbf{n})|\partial\Omega = 0$, where $\partial\Omega$ denotes the border of Ω and $\mathbf{n}$ is the outer normal to the $\partial\Omega$. The diffusion coefficient is

defined as

$$c(q) = \frac{1}{1+[q^2(x,y;t) - q_0^2(t)]/[q_0^2(t)(1+q_0^2(t))]} \tag{5.5}$$

If $c(q)$ is constant, then SRAD reduces to isotropic diffusion. The instantaneous coefficient of variation is

$$q(x,y;t) = \sqrt{\frac{\frac{1}{2}(|\nabla I|/I)^2 - \frac{1}{16}(\nabla^2 I/I)^2}{[1+\frac{1}{4}(\nabla^2 I/I)]^2}} \tag{5.6}$$

$q_0(t)$ is the speckle scale function, $q_0(t) = \frac{\sqrt{\text{var}[z(t)]}}{\overline{z(t)}}$, where $\text{var}[z(t)]$ and $\overline{z(t)}$ are the intensity variance and mean over a homogeneous area at t, respectively. In order to reduce user interaction and avoid choosing a homogeneous region in the image, $q_0(t)$ can be approximated as $q_0(t) \approx \exp(-\frac{1}{6}\cdot t)$ [120].

Assume a sufficiently small time step size of Δt and sufficiently small spatial step size of h in x and y directions, $t = n\Delta t$, $x = ih$, $y = jh$. i, j is the pixel index. The discretization form of items $|\nabla I|/I$, $\nabla^2 I/I$ inside $q(x,y,t)$ can be expressed as

$$|\nabla I|/I = \frac{1}{I_{i,j}^n}\sqrt{\left|\nabla_R I_{i,j}^n\right|^2 + \left|\nabla_L I_{i,j}^n\right|^2} \tag{5.7}$$

where $\nabla_R I_{i,j}^n = \left[\frac{I_{i+1,j}^n - I_{i,j}^n}{h}, \frac{I_{i,j+1}^n - I_{i,j}^n}{h}\right]$, $\nabla_L I_{i,j}^n = \left[\frac{I_{i,j}^n - I_{i-1,j}^n}{h}, \frac{I_{i,j}^n - I_{i,j-1}^n}{h}\right]$,

$$\nabla^2 I/I = \frac{I_{i+1,j}^n + I_{i-1,j}^n + I_{i,j+1}^n + I_{i,j-1}^n - 4I_{i,j}^n}{I_{i,j}^n \cdot h^2} \tag{5.8}$$

5.2.1.3 Nonlinear Complex Diffusion (NCD) [121]

Complex diffusion is a new recently proposed PDE-based method that extends the diffusion process from the real axis to the complex domain. In this method, the diffusion coefficient is a complex-value coefficient. An important observation is that the imaginary value serves as a robust edge-detector (i.e., it is a smoothed second derivative of the initial signal scaled by time) with increasing confidence in time. It thus handles noise well and may serve as a controller for

nonlinear processes [121]. Numerical evidence shows that the qualitative characteristics of the imaginary part in nonlinear processes are similar to the linear case, especially at the zero crossing locations [121]. The nonlinear complex diffusion approach does remove noise from edges, avoids staircasing (a known byproduct of Perona-Malik that can create false edges) and removes more noise [121].

The equation for the nonlinear complex diffusion approach is:

$$\frac{\partial I}{\partial t} = \nabla \cdot (d(\mathrm{Im}(I))\nabla I) \tag{5.9}$$

where $\mathrm{Im}(\cdot)$ is the imaginary value and the diffusivity is defined as

$$d(\mathrm{Im}(I)) = \frac{\exp(iq)}{1+(\frac{\mathrm{Im}(I)}{kq})^2} \tag{5.10}$$

where k is a threshold parameter and $q \in (-p/2; p/2)$ is the phase angle.

5.2.2 Automatic stopping time T selection strategies

In these approaches, stopping time T is an important parameter and its value has a strong effect on the diffusion result. Small T removes noise slightly and does not cause blurring, while large T creates more homogeneous regions. In addition, different images have different features and different diffusion iterations are needed. So a fixed number of iteration will cause some problems when these diffusion methods are used in real applications. Some automatic stopping time selection strategies have been proposed.

(1) The mean absolute error (MAE) between two adjacent diffusion steps can be used to stop the iteration [122]:

$$MAE = \frac{1}{M \times N} \times \sum_{(i,j)=1}^{M,N} \sqrt{(I(i,j,t) - I(i,j,t-1))^2} \tag{5.11}$$

where M, N is the size of the image and $I(i,j,t)$ is the value of pixel (i,j) at time t.

(2) Weickert's criterion is based on the notion of relative variance [123].

$$r(u(t)) = \frac{\mathrm{var}(u(t))}{\mathrm{var}(u(0))} \tag{5.12}$$

where $\mathrm{var}(u(t))$ denote the variance of an image $u(t)$.

The automatic stopping time T can be obtained if knowing the SNR (signal-to-noise ratio),

$$r(u(T)) = \frac{\mathrm{var}(u(T))}{\mathrm{var}(u(0))} = \frac{1}{1+\frac{1}{SNR}} \tag{5.13}$$

(3) Mrázek's criterion is based on the correlation, assuming the noise is uncorrelated with the ideal image [124]. The correlation coefficient is

$$corr(u(0)-u(t),u(t)) = \frac{\mathrm{cov}(u(0)-u(t),u(t))}{\sqrt{\mathrm{var}(u(0)-u(t))\cdot \mathrm{var}(u(t))}} \tag{5.14}$$

The automatic stopping time T can be selected,

$$T = \arg\min_t corr(u(0)-u(t),u(t)) \tag{5.15}$$

5.2.3 Image quality measurement

In order to quantify nonlinear diffusion filtering performance, different measure metrics were calculated based on the original and the filtered images. Extensively used criteria include S/MSE ratio, correlation parameter and structure similarity.

5.2.3.1 Signal-to-minimum square error (S/MSE) ratio [126]

S/MSE is used to evaluate the performance of suppressing noise.

$$\frac{S}{MSE} = 10\log_{10}\left[\frac{\sum_{i=1}^{M} I_i^2}{\sum_{i=1}^{M}(\hat{I}_i - I_i)^2}\right] \tag{5.16}$$

where I is the original image, $\hat{I}$ is the filtered image and M is the image size.

5.2.3.2 Correlation parameter c [126]

c is used to evaluate the performance of edge preservation.

$$c = \frac{\sum_{i=1}^{M}(\Delta I_i - m)\times(\Delta\hat{I}_i - n)}{\sqrt{\sum_{i=1}^{M}(\Delta I_i - m)\times(\Delta I_i - m)\times\sum_{i=1}^{M}(\Delta\hat{I}_i - n)\times(\Delta\hat{I}_i - n)}} \tag{5.17}$$

where ΔI and $\Delta\hat{I}$ are the resultant images using 3×3 Laplacian operator, m, n are the mean values of ΔI and $\Delta\hat{I}$, respectively.

5.2.3.3 Structure similarity (SSIM) [127]

$$SSIM(X,Y) = \frac{(2m_x m_y + C_1)(2s_{xy} + C_2)}{(m_x^2 + m_y^2 + C_1)(s_x^2 + s_y^2 + C_2)} \tag{5.18}$$

where X, Y are the original and denoised images. m_i and s_i ($i = X$ or Y) are the mean and standard deviation of pixels in a defined local window. C_i is the constant to avoid instability.

A mean SSIM index (***MSSIM***) is used to evaluate the overall processing quality of the entire image.

$$MSSIM(X,Y) = \frac{1}{N}\sum_{i=1}^{N} SSIM(X_i, Y_i) \tag{5.19}$$

5.2.4 Experimental results of denoising

Corneal OCT images have been processed using the PM filter, SRAD and NCD methods. Various parameters in these methods can affect the filtering results. In PM filter, the gradient threshold k and the iteration number N play important roles in denoising performance. In SRAD, the iteration number N controls the diffusion process. In NCD, the filtering result is mainly affected by the gradient threshold k and the iteration number N and not much by q if it is small. We have conducted experiments using these methods and will present the filtering results.

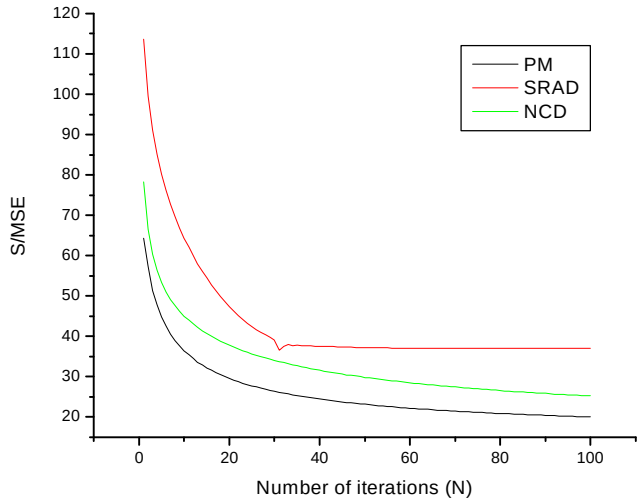

Figure 5.2: Measured S/MSE as iteration number N is varied from 1 to 100

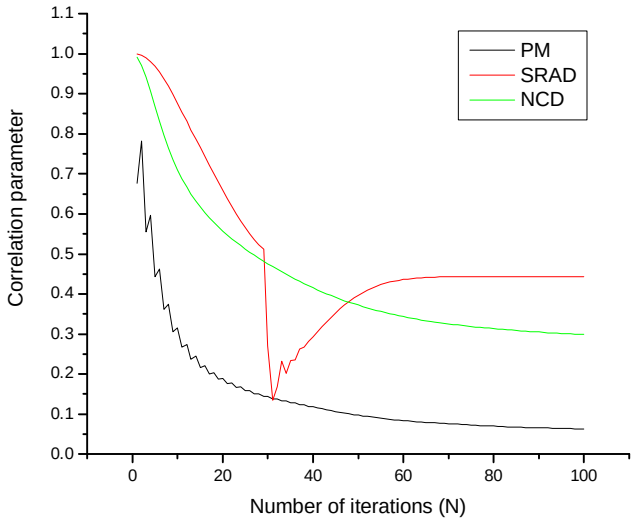

Figure 5.3: Measured correlation parameter c as iteration number N is varied from 1 to 100

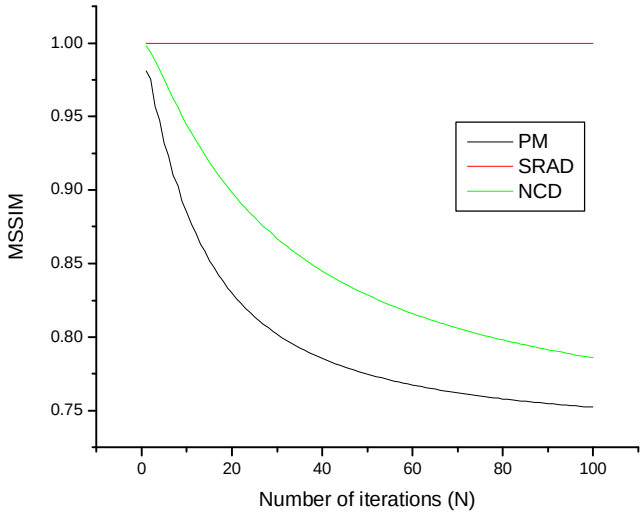

Figure 5.4: Measured MSSIM as iteration number N is varied from 1 to 100

In PM filter, diffusivity function was chosen as equation (5.2) and k =40, a time step Δt =0.24 was set in the numerical implementation. In SRAD, $q_0(t) \approx \exp(-\frac{1}{6} \cdot t)$, parameter h =1, Δt =0.05 were set. In NCD, k =9, $q = p/30$, Δt =0.24 were set. We compared their filtering performance according to these metrics: S/MSE ratio, correlation parameter and structure similarity. The experimental results are shown in Figures 5.2, 5.3, 5.4. It can be seen that these

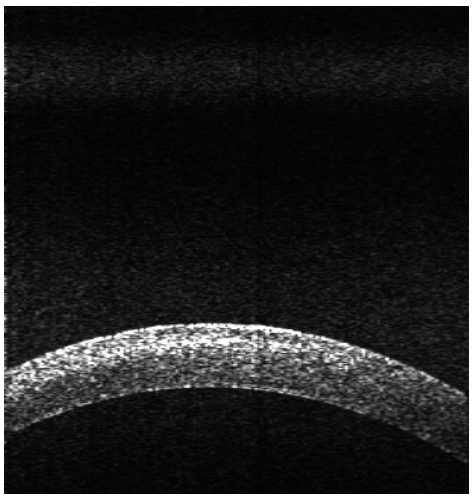

Figure 5.5: Original OCT image

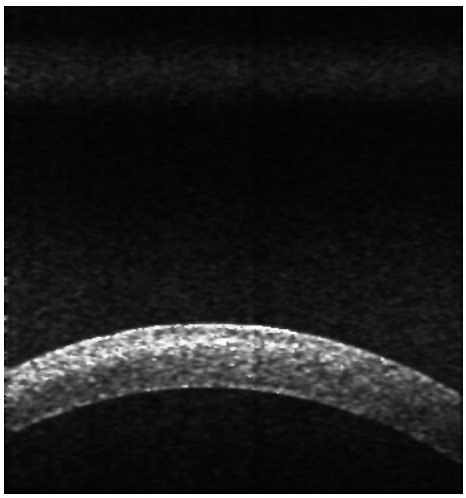

Figure 5.6: PM filtered image, equation (5.2), iterations=20

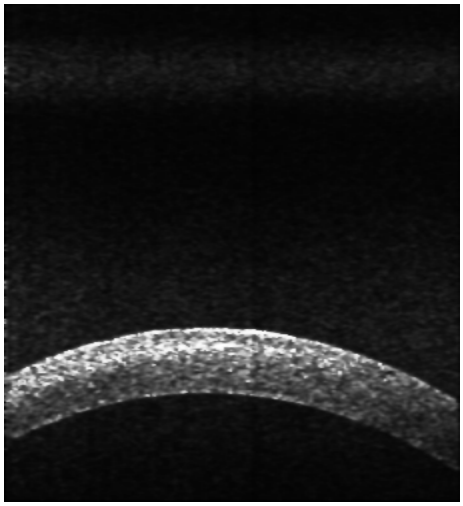

Figure 5.7: PM filtered image, equation (5.3), iterations=20

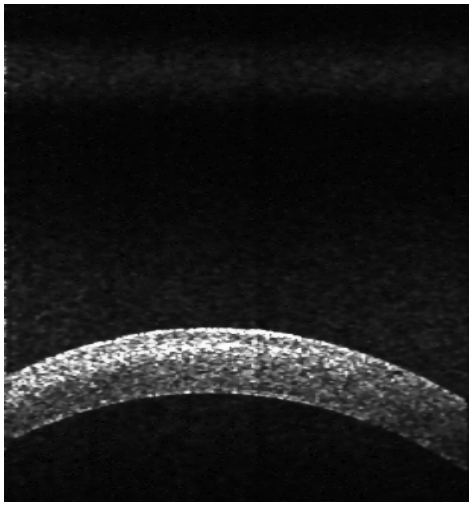

Figure 5.8: SRAD filtered image, iterations=30

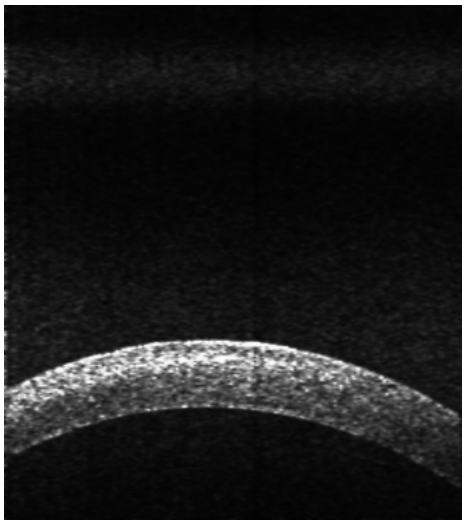

Figure 5.9: NCD filtered image, iterations=30

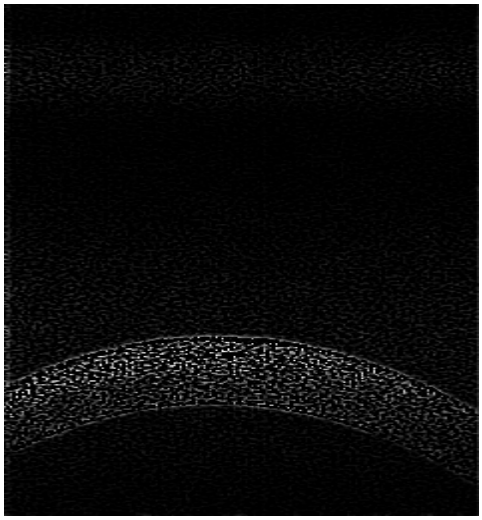

Figure 5.10: Imaginary part of NCD filtered image, iterations=30

metrics will decrease when the iteration number N increases. But the curve of correlation parameter c for SRAD has one valley. S/MSE and MSSIM indicate that SRAD has better noise depression effect and better processing quality than NCD and PM filter.

The filtered images using these methods are shown in Figures 5.6-5.10. Figure 5.5 is the original image, Figure 5.6 and Figure 5.7 are the resulting images using the PM filter. Diffusivity functions were chosen as equation (5.2) and (5.3) separately, and iteration number was set 20. Figure 5.8 is the resulting image using SRAD method and iteration number was set 30. Figure 5.9 is the resulting image using NCD method and iteration number was set 30. Figure 5.10 is the imaginary part (factored 80) of the filtered image using NCD method. It can be used for some segmentation tasks.

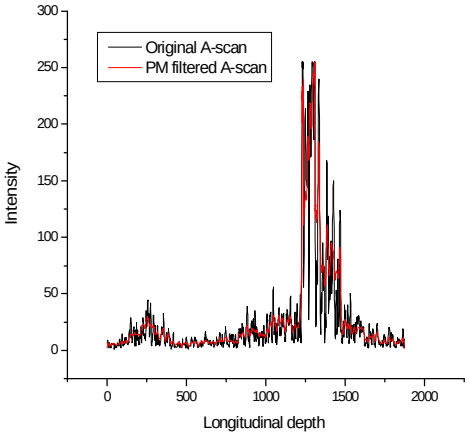

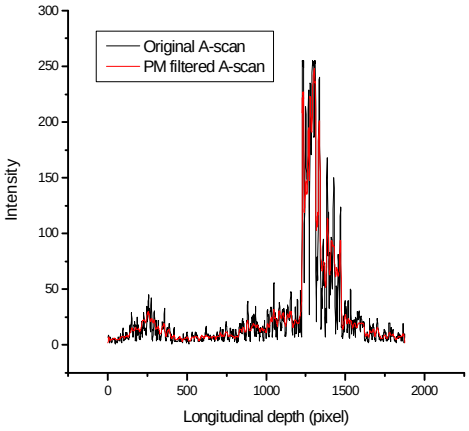

Figure 5.11: The 400th A-scan using PM filter, E(5.2)

Figure 5.12: The 400th A-scan using PM filter, E(5.3)

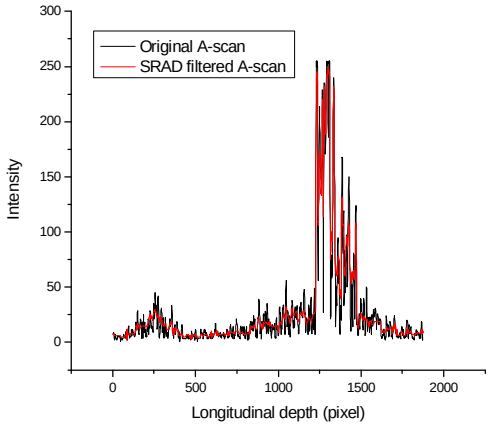

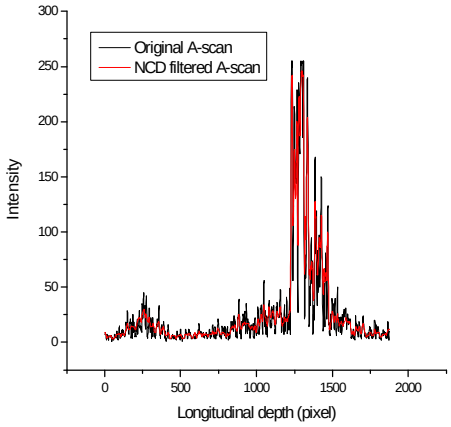

Figure 5.13: The 400th A-scan using SRAD method

Figure 514: The 400th A-scan using NCD method

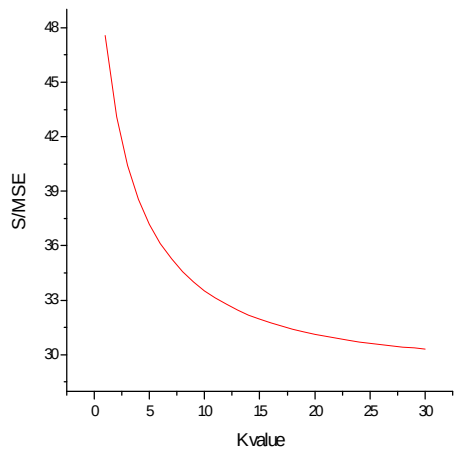

Figure 5.15: Measured S/MSE with increase of k

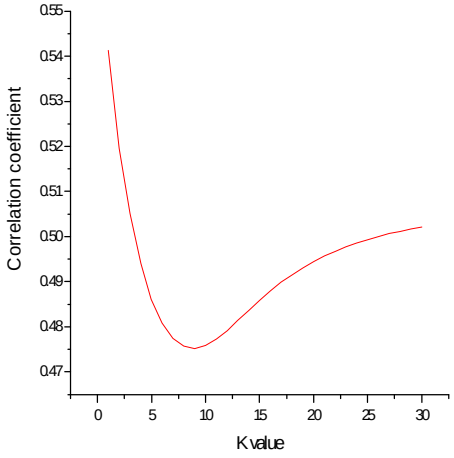

Figure 5.16: Measured c with increase of k

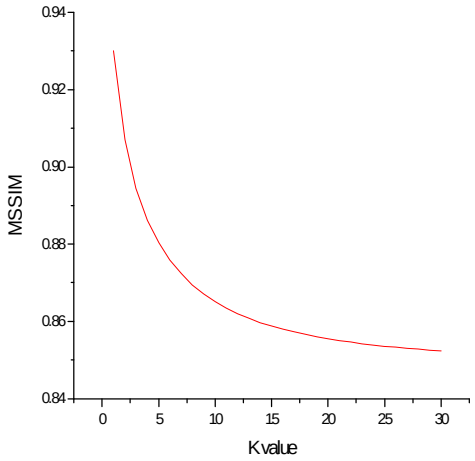

Figure 5.17: Measured MSSIM with increase of k

Figures 5.11-14 show the 400th A-scan from original image and filtered image as shown in Figures 5.6-9. It can be seen that the noise has been suppressed and edges are still preserved well.

In addition, some important parameters in these diffusion methods can be fine tuned. For example, in NCD method, the gradient threshold k was tuned as follows. $N = 30$, $q = p/30$, Δt =0.24 were set. When k was varied from 1 to 30, S/MSE, correlation parameter, and MSSIM were measured as shown in Figures 5.15, 5.16 and 5.17. The optimal value for k can be set 9 where the correlation parameter achieves an extremum value. However, the curves for S/MSE and MSSIM decrease and can't achieve extremum values at k =9.

5.3Segmentation of OCT images

Quantification provides a measure of disease progression and accurate measurement of shape changes may significantly aid in analysis of treatments and diagnosis for certain diseases. To quantitatively extract important parameters from OCT images and efficiently evaluate biological phenomena in the experiments, we will have to employ image analysis technologies. Image segmentation is a crucial step in image analysis which can distinguish objects from background. Many segmentation methods have been proposed and successfully used in analysis of biological images, such as watershed segmentation [128], concavity analysis [129], active contours and level sets [130, 131], etc..

Watershed segmentation is similar to the process of watershed merging that takes place when rain falls over a real landscape. An image can be considered as a topographic surface. Its minima will be found firstly using some automatic segmentation methods and with some segmentation criteria, the image will be partitioned into objects, background as well as watershed lines.

Concavity analysis method offers a good solution for segmenting clumped cells. Some deep boundary pixels, i.e., the concavity pixels in a clump, are automatically detected. Then concavity-based rules will be based to choose good split line, the clumped cells will be separated with each other and automatic counting of cells can be performed.

An active contour is an evolving implicit curve, subject to constraints from a given image, in order to detect or recover objects in the image background. Below is one classical active contour model. The basic idea of this model is to minimize the energy functional $F(c_1, c_2, C)$, defined by

$$F(c_1, c_2, C) = m \cdot \text{Length}(C) + n \cdot \text{Area}(inside(C)) + l_1 \int_{inside(C)} |u_0(x,y) - c_1|^2 \, dxdy + l_2 \int_{outside(C)} |u_0(x,y) - c_2|^2 \, dxdy \tag{5.20}$$

where u_0 is the image, C is any variable curve, c_1, c_2 are the averages of u_0 inside C and outside C. $inside(C)$, $outside(C)$ denotes the region inside C and outside C in the image, respectively. Length(C) denotes the length of C. Area($inside(C)$) denote the area enclosed by C. $m \geq 0$, $n \geq 0$, $l_1 > 0$, $l_2 > 0$ are fixed parameters.

These methods provide important solutions to automatically segment objects in biological images and make process of object counting and measurements fast and precise. Research on automatic segmentation methods for biological images always pose interesting challenges. In this chapter, we will investigate minimal-cost path method for targeted curve extraction. This method does not rely on too much user initialization and only two end points are needed.

5.3.1 Minimum-cost path theory

The basic theory of minimum-cost path has been proposed for many years and used in different research fields [132-138]. A typical application example is in geometrical optics. The principle of Fermat states that light waves of a given frequency traverse the path between two points which takes the least time. In a homogeneous medium where the speed of light does not change with position, the least time is equivalent to the shortest distance between the points, which is a straight line. This is consistent with the phenomena that light wave travels in a straight line in a homogeneous medium.

In the graph subject, some applications seek minimum-cost path. Assumed different weights are assigned to each link in a graph, the cumulative cost between a starting vertex A and a certain destination point x can be obtained by summing up all prescribed weights (costs) along the path linking them. The minimum cumulative cost is defined as

$$U(x) = \min_{C_{Ax}} \int_0^L t\,(C(s))ds \tag{5.21}$$

where C_{Ax} is the set of all paths linking A and x. t is the cost function. L is the path length. The starting and ending points are $C(A) = 0$ and $C(x) = L$, respectively. The line element ds is measured along the path.

The minimum-cost path is the one that has the lowest cumulative cost among all possible paths linking these two vertices. The solution of (5.21) satisfies the Eikonal equation (front propagation equation that physically models wave-light propagation):

$$\left\|\nabla U\right\| = t \tag{5.22}$$

5.3.2 Construction of cost function

The choice of cost function t is important for the segmentation of contours in the images. In this minimal path method, a digital image is considered to be a graph. The contour boundary is

defined as the minimum of the cost function. Then the optimal boundary extraction between two image pixels is transformed for finding the optimal path between two vertices in the graph. The cost function includes the salient features of contours. Some features, such as gradient magnitude, direction of gradient magnitude, Laplacian, intensity on the boundary, have been used to describe properties of the boundary.,

5.3.3 Fast marching method

Existing methods of minimal path search include graph search method and fast marching method [134]. There is no big difference in the overall computational complexity between both methods. However, the graph search method suffers from metrication errors as the generated path will be made by segments with only vertical, horizontal or diagonal directions. The fast marching method will produce more accurate and consistent results, which is an extremely fast scheme based on solving Eikonal equation [134].

Assume $t > 0$, the moving front always propagates "outwards", On 2D Cartesian grids with coordinates i and j, the position of this expanding front can be described by the arrival time map $U(i, j)$ when it crosses each point (i, j). The solution of the following equation will give the correct viscosity solution $u_{i,j}$ for U at point (i, j):

$$\max(u_{i,j} - u_{i-1,j}, u_{i,j} - u_{i+1,j}, 0)^2 + \max(u_{i,j} - u_{i,j-1}, u_{i,j} - u_{i,j+1}, 0)^2 = t_{i,j}^{\ 2} \qquad (5.23)$$

The fast marching method was proposed to solve equation (5.23). The main point of this method is to introduce an order in the selection of the grid points. This order is based on the fact that the arrival time u at any point depends only on neighbors that have smaller values. The front always moves in the same direction, because it requires a single crossing time at each grid point, and hence a point can't be revisited. The minimal path can be obtained by back-propagation on the computed arrival time map U. The back-propagation procedure consists in gradient descent on U starting from destination point x until starting point A is reached.

5.3.3.1 The solution to Eikonal equation under four-connected neighbors [137]

In 2D Cartesian space as shown in Figure 5.18, we will discuss how to solve equation (5.14) and compute the arrival time map U. Assume that points A, B have smaller arrival time u_A and u_B among the four-connected neighbors of point C, then the minimal path to point C

comes from the quadrant AB and intersects AB at point D. This means the arrival time $u_{AB}(C)$ at point C will be dependent on u_A and u_B, and $u_{AB}(C) > u_A$, $u_{AB}(C) > u_B$.

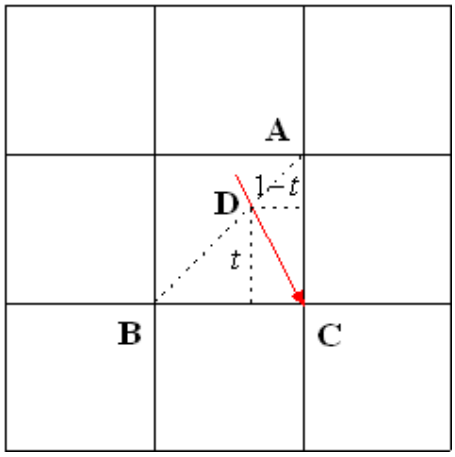

Figure 5.18: The schematic diagram of minimal path in Cartesian grid under four-connected neighbors

The arrival time u_D at point D can be approximated using linear interpolation based on u_A and u_B,

$$u_D = t \cdot u_A + (1-t) \cdot u_B \tag{5.24}$$

where t is the parameter that decides the front propagation direction, $0 \le t \le 1$. Then the arrival time $u_{AB}(C)$ can be approximated as the summation u_D and the traveling time from D to C,

$$u_{AB}(C) = \min_{0 \le t \le 1}(t \cdot u_A + (1-t) \cdot u_B + \sqrt{t^2 + (1-t)^2} \cdot t_C) \tag{5.25}$$

where t_C is the cost at point C. The closed form solution of equation (5.25) can be obtained as,

$$u_{AB}(C) = \begin{cases} \frac{1}{2}(u_A + u_B + \sqrt{2t_C^2 - (u_A - u_B)^2} & \textit{if} \quad u_{AB}(C) > u_A \quad \textit{and} \quad u_{AB}(C) > u_C \\ \min(u_A, u_B) + t_C & \textit{Otherwise} \end{cases} \tag{5.26}$$

5.3.3.2 The solution to Eikonal equation under eight-connected neighbors [137]

Assume that points A, B have smaller arrival time u_A and u_B among the

eight-connected neighbors of point C, then the minimal path to point C comes from the octant AB and intersects AB at point E, as shown in Figure 5.19.

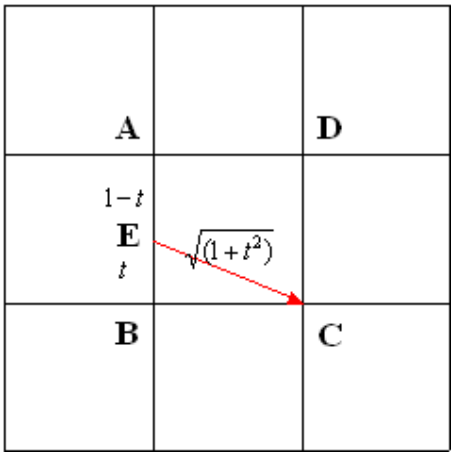

Figure 5.19: The schematic diagram of minimal path in Cartesian grid under eight-connected neighbors

The arrival time u_E at point E can be approximated using linear interpolation based on u_A and u_B,

$$u_E = t \cdot u_A + (1-t) \cdot u_B \tag{5.27}$$

Then the arrival time $u_{AB}(C)$ can be approximated as the summation u_E and the traveling time from E to C,

$$u_{AB}(C) = \min_{0 \le t \le 1} (t \cdot u_A + (1-t) \cdot u_B + \sqrt{1+t^2} \cdot t_C) \tag{5.28}$$

The closed form solution of equation (5.28) can be obtained as,

$$u_{AB}(C) = \begin{cases} u_B + t_C & \text{if} \quad u_B \le u_A \\ u_A + \sqrt{2} \cdot t_C & \text{if} \quad t_C \le \sqrt{2} \cdot (u_B - u_A) \\ u_B + \sqrt{t_C^2 - (u_B - u_A)^2} & \text{Otherwise} \end{cases} \tag{5.29}$$

5.3.3.3 The fast marching algorithm

In detail, the fast marching algorithm is as follows.

(1) Assign the starting point S, with u_S = 0. Label it as *Accepted* point.

(2) Label the N (N = 4 or 8) neighbouring points of S as *Trial* points. Calculate the arrival time u of the *Trial* points according to Equation (5.26) (N = 4) or Equation (5.29) (N = 8).

(3) Label all other points as *Far* points, with $u = \infty$.

(4) Determine the *Trial* point A that has the smallest u value in the *Trial* set.

(5) Remove A from *Trial* set and add it to *Accepted* set.

(6) Label as *Trial* points all N neighbouring points of A that are not already *Accepted* points. If the neighboring point is in *Far* set, removes, and add to the set *Trial* set. Update their arrival time u according to Equation (5.26) (N = 4) or Equation (5.29) (N = 8).

(7) If all points are labeled as *Accepted* points, then exit, else go to step (4).

5.3.4 Experimental results of segmentation

The segmentation experiments have been performed on Corneal OCT image of the rabit eye using fast marching method. Figure 5.20 is the original image. The cost function has been constructed using gradient magnitude and shown in Figure 5.21. In addition, the cost function has been constructed based on SRAD filtered image Figure 5.8 and Figure 5.22 shows the result.

Figure 5.23 is the calculated time map U using Figure 5.21 as cost function, with two input points on the top surface of the corneal, and Figure 5.24 is the resulting image. The red line represents the extracted top surface of the corneal using fast marching method. Figure 5.25 is the calculated time map U using Figure 5.21 as cost function, with two input points on the bottom surface of the corneal, and Figure 5.26 is the resulting image. The red line represents the extracted bottom surface of the corneal using fast marching method.

Figure 5.27 is the calculated time map U using Figure 5.22 as cost function, with two input

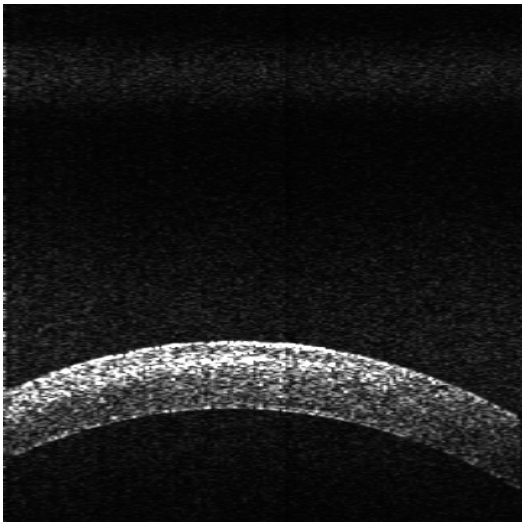

Figure 5.20: The original image

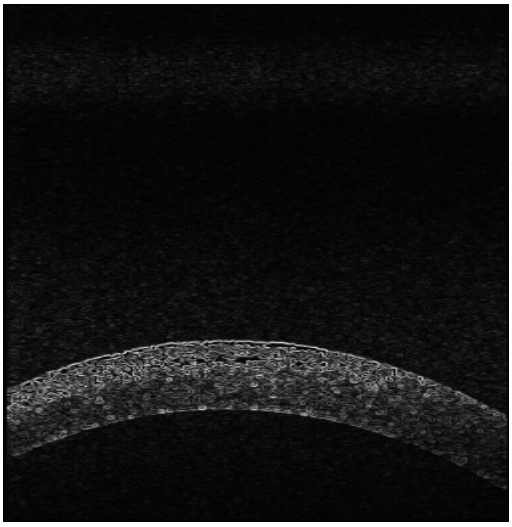

Figure 5.21: Cost function using Figure 5.20

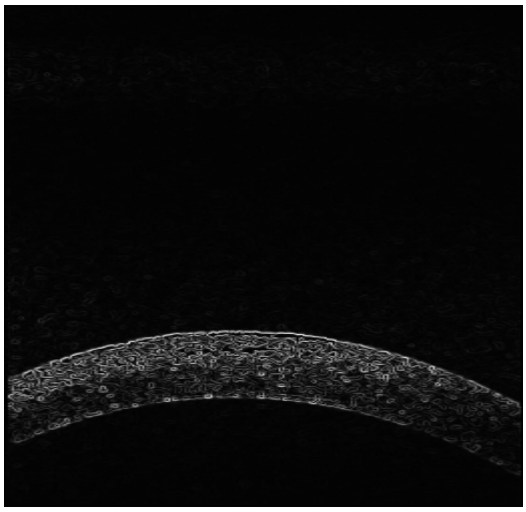

Figure 5.22: Cost function using Figure 5.8

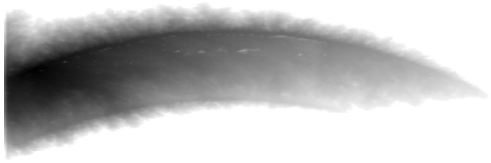

Figure 5.23: Calculated time map U using Figure 5.21

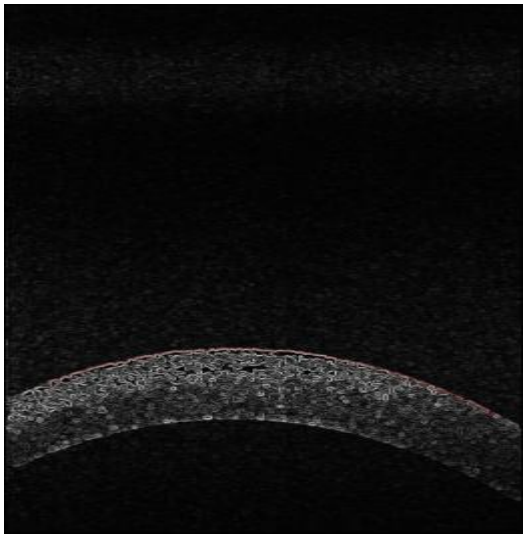

Figure 5.24: Top surface on Figure 5.21

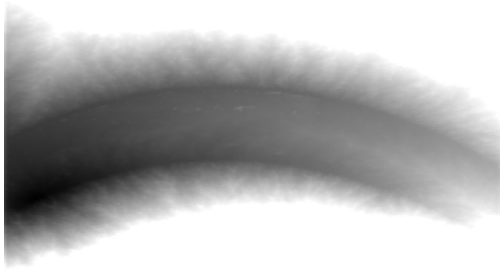

Figure 5.25: Calculated time map U using Figure 5.21

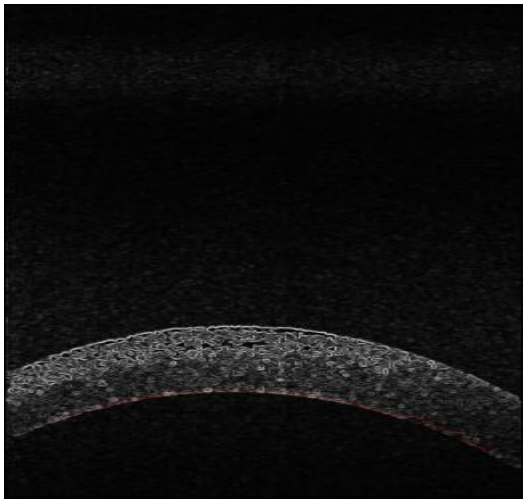

Figure 5.26: Bottom surface on Figure 5.22

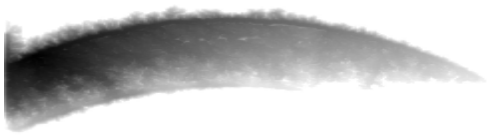

Figure 5.27: Calculated time map U using Figure 5.22

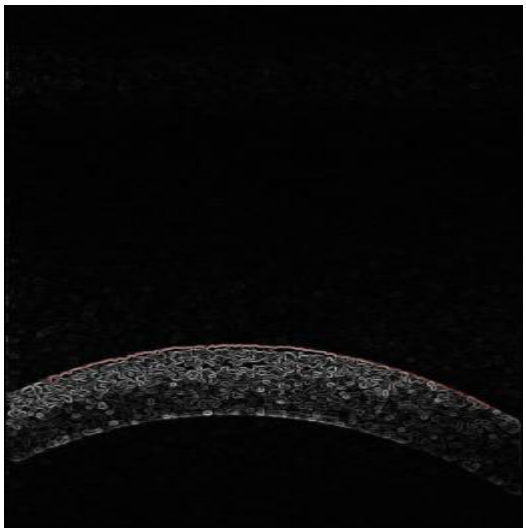

Figure 5.28: Top surface on Figure 5.22

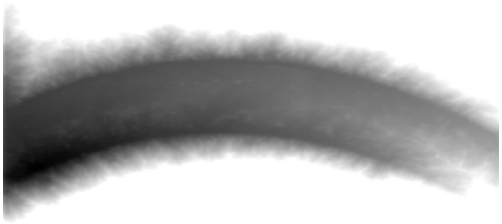

Figure 5.29: Calculated time map U using Figure 5.22

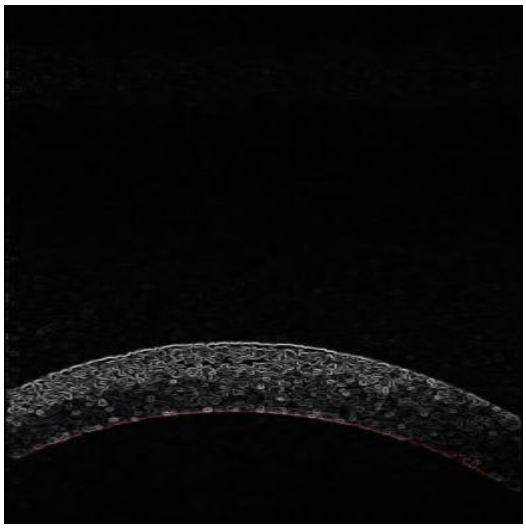

Figure 5.30: Bottom surface on Figure 5.22

points on the top surface of the corneal, and Figure 5.28 is the resulting image. The red line represents the extracted top surface of the corneal using fast marching method. Figure 5.29 is the calculated time map U using Figure 5.22 as cost function, with two input points on the bottom surface of the corneal, and Figure 5.30 is the resulting image. The red line represents the extracted bottom surface of the corneal using fast marching method.

It can be seen that the extracted curves in SRAD filtered image are smoother than those in the original image. This proved that nonlinear diffusion method can depress noise and preserve (or enhance) edge and facilitate the following segmentation tasks.

5.4 Conclusions

In this chapter, we summarized (1) PDE-based diffusion method, (2) Fast marching method separately and applied them for OCT images. As the speckle noise is transformed into additive noise when OCT images form, nonlinear PDE-based diffusion method is particularly suitable for denoising of OCT images. Some classical nonlinear diffusion methods, such as PM filter, SRAD, as well as NCD have been studied. The filtered images using these methods have been shown and the noise suppression and edge preserving effects have been evaluated according to some measurement metrics.

In order to efficiently extract targeted curves in the OCT images, minimal-cost path and fast marching methods have been employed. The detailed description of these algorithms and experimental results have been given.

Chapter 6 Conclusions

In this project, we aim to develop high-resolution, rapid-speed time-domain OCT system and apply it into biological fields. Main works have been done in four areas: (1) Envelope detection technology; (2) Fourier domain optical delay line; (3) Sample arm; (4) Image processing technology.

6.1 Summary of Contributions

The time-domain OCT system has been set up as shown in Figure 1.8. Its design of system components, signal processing technology and system integration for high-resolution imaging was demonstrated in this thesis.

In the introduction of this thesis, current OCT imaging modalities and important design issues for the OCT system have been described. Some novel contrast enhancing methods have been summarized which can improve the diagnostic abilities of the OCT system.

In Chapter 2, according to the basic formulation of interferometric signal of time-domain OCT system, the performance of different envelope detection technologies, such as FFT method and HT method, has been investigated. Experimental results show that FFT or HT method does not extract the envelope well if there are less than 1.5 oscillations inside the envelope of the interferometric signal. About 1.5 oscillations inside the envelope will be enough for extracting the envelope using FFT or HT method.

In Chapter 3, fast FD_ODL for time-domain OCT system has been studied thoroughly. Results show that the offset of the scanning mirror can control numbers of oscillations inside the envelope of the interferometric signal of time-domain OCT system. Some important constrained

conditions about minimal size of the scanning mirror and scanning depth of the OCT system have been obtained. In addition, geometric ray tracing analysis method has been used to analyze the dispersion problem of FD_ODL.

In Chapter 4, the sample probe as shown in Figure 4.3 was designed as it can provide 3D imaging capability. Some relationship equations about the relay optics of the sample probe have been obtained using geometric ray tracing analysis method. In addition, the relationship between the depth of field and the transverse resolution was obtained and an appropriate focusing lens in the sample probe should be used for the OCT system.

In Chapter 5, to suppress speckle noise in OCT images, some classical nonlinear PDE-based diffusion methods, such as PM filter, SRAD, as well as NCD, were investigated. Their filtering effects were evaluated using some measurement metrics. In addition, fast marching method was used to extract the targeted curves in OCT images. Relevant experimental results have been given.

6.2 Future directions of research

Recent advances in lasers, optical fibre technology and electronics components greatly improve the imaging resolution, imaging speed of the OCT system. The rapid, high-resolution OCT systems have been realized in Time-domain and Fourier-domain separately. With a wide range of in vivo application requirements in tissue pathologies and ophthalmology, they have been developed into different kinds of clinical instruments, such as surgical probes, endoscopes and laparoscopes, and integrated with commercial optical microscopes.

Many meaningful research works about the OCT system can be further performed more thoroughly. For example, the formation of OCT images from the envelope of the interferometric signal can be further optimized using different methods. Information about specific objects hidden in the envelope of the interferometric signal can be interpreted or revealed more efficiently. Some

contrast enhancement work for special tissues can be conducted to improve the diagnostic ability of early pathologies using OCT systems. The mapping relationship between tissue structure images and early pathologies can be established to aid in future clinical diagnosis. In addition, automatic and accurate segmentation technologies as well as visualization technologies can be further investigated to facilitate quantitative measurements of biological phenomena using OCT systems.

REFERENCES

[1] S. E. Nissen, J. C. Gurley, D. C. Booth, and A. N. DeMaria, "Intravascular ultrasound of the coronary arteries: current applications and future directions," *The American Journal of Cardiology*, vol. **69**, pp. H18-H29, June 1992.

[2] J. P. Hornack, "The basics of MRI," http://www.cis.rit.edu/htbooks/mri/.

[3] http://www.microscopyu.com/articles/confocal/.

[4] D. Huang, E. A. Swanson, C. P. Lin, J. S. Shuman, W. G. Stinson, W. Chang, M. R. Hee, T. Flotte, K. Gregory, C. A. Puliafito, and J. G.Fujimoto, "Optical coherence tomography," *Science*, vol. **254**, pp. 1178-1181, Nov. 1991.

[5] W. Drexler, U. Morgner, F. X. K¨artner, C. Pitris, S. A. Boppart, X. D. Li, E. P. Ippen, and J. G. Fujimoto, "In vivo ultrahigh-resolution optical coherence tomography," *Optics Letters*, vol. **24**, no. 17, pp. 1221-1223, September 1999.

[6] I. Hartl, X. D. Li, C. Chudoba, R. K. Ghanta, T. H. Ko, and J. G. Fujimoto, "Ultrahigh-resolution optical coherence tomography using continuum generation in an air-silica microstructure optical fiber," *Optics Letters*, vol. **26**, no. 9, pp. 608-610, May 2001.

[7] A. M. Rollins, S. Yazdanfar, J. K. Barton, and J. A. Izatt, "Real-time in vivo color Doppler optical coherence tomography," *Journal of Biomedical Optics*, vol. **7**, no. 1, pp. 123-129, 2002.

[8] J. G. Fujimoto, "Optical coherence tomography for ultrahigh resolution in vivo imaging," *Nature Biotechnology*, vol. **21**, no. 11, pp. 1361-1367, Nov. 2003.

[9] W. Drexler, "Ultrahigh-resolution optical coherence tomography," *Journal of Biomedical Optics*, vol. **9**, no. 1, pp. 47-74, January/February 2004.

[10] J. G. Fujimoto, M. E. Brezinski, G. J. Tearney, S. A. Boppart, B. Bouma, M. R. Hee, J. F. Southern and E. A. Swanson, "Optical biopsy and imaging using optical coherence tomography," *Nature Medicine*, vol. **1**, no. 9, pp. 970-972, 1995.

[11] Y. Pan, E. Lankenau, J. Welzel, R. Birngruber, and R. Engelhardt, "Optical coherence-gated imaging of biological tissues," *IEEE Journal of Selected Topics in Quantum Electronics*, vol. **2**, no.

4, pp. 1029-1034, Dec. 1996.

[12] S. A. Boppart, G. J. Tearney, B. E. Bouma, J. F. Southern, M. E. Brezinski and J. G. Fujimoto, "Noninvasive assessment of the developing Xenopus cardiovascular system using optical coherence tomography," *Proc. Natl. Acad. Sci. USA 94*, pp. 4256-4261, 1997.

[13] Victor X.D. Yang, Maggie L. Gordon, Bing Qi, Julius Pekar, Stuart Lo, Emily Seng-Yue, Alvin Mok, Brian C. Wilson, and I. Alex Vitkin, "High speed, wide velocity dynamic range Doppler optical coherence tomography (Part II): Imaging in vivo cardiac dynamics of Xenopus laevis," *Optics Express*, vol. **11**, no.14, pp.1650-1658, July 2003.

[14] W.Jung, B.Kao, K. M. Kelly, L.-H. L. Liaw, J. S. Nelson, and Z. Chen, "Optical coherence tomography for in vitro monitoring of wound healing after laser irradiation," *IEEE Journal of Selected Topics in Quantum Electronics*, vol. **9**, pp. 222-226, 2003.

[15] Victor X.D. Yang, Maggie L. Gordon, Bing Qi, Julius Pekar, Stuart Lo, Emily Seng-Yue, Alvin Mok, Brian C. Wilson, and I. Alex Vitkin, "High speed, wide velocity dynamic range Doppler optical coherence tomography (Part I): System design, signal processing, and performance," *Optics Express*, vol. **11**, no.7, pp.794-809, April 2003.

[16] C. Xi, D. L. Marks, D. S. Parikh, L. Raskin, and S. A. Boppart, "Structural and functional imaging of 3D microfluidic mixers using optical coherence tomography," *Proc. Natl. Acad. Sci. U.S.A.*, vol. **101**, pp. 7516-7521, 2004.

[17] S. A. Boppart, W. Luo, D. L. Marks, K. W. Singletary, "Optical coherence tomography: feasibility for basic research and image-guided surgery of breast cancer," *Breast Cancer Res Treatment*, vol. **84**, pp. 85-97, 2004.

[18] M. W. Jenkins, F. Rothenberg, D. Roy, V. P. Nikolski, Z. Hu1, M. Watanabe, D. L. Wilson, I. R. Efimov, and A. M. Rollins, "4D embryonic cardiography using gated optical coherence tomography," *Optics Express*, vol. **14**, no. 2, pp. 736-748, January 2006.

[19] K. Bizheva, A. Unterhuber, B. Hermann, B. Povaay, H. Sattmann, and A. F. Fercher, "Imaging ex vivo healthy and pathological human brain tissue with ultra-high-resolution optical coherence tomography," *Journal of Biomedical Optics*, vol. **10**, no. 1, 11006, January/February 2005.

[20] Y. Pan and D. L. Farkas, "Noninvasive imaging of living human skin with dual-wavelength optical coherence tomography in two and three dimensions," *Journal of Biomedical Optics*, vol. **3**, pp. 446-455, 1998.

[21] T. Gambichler, G. Moussa, M. Sand, D. Sand, P. Altmeyer, K. Hoffmann, "Applications of optical coherence tomography in dermatology," *Journal of Dermatological Science*, vol. **40**, no. 2, pp. 85-94, 2005.

[22] Y. Zhao, Z. Chen, C. Saxer, S. Xiang, J. F. De Boer, and J. S. Nelson, "Phase-resolved optical coherence tomography and optical Doppler tomography for imaging blood flow in human skin with fast scanning speed and high velocity sensitivity," *Optics Letters*, vol. **25**, no. 2, pp. 114-116, 2000.

[23] M. Brezinski, K. Saunders, C. Jesser, X. Li, J. Fujimoto, "Index matching to improve optical coherence tomography imaging through blood," *Circulation*, vol. **103**, pp. 1999-2003, 2001.

[24] Victor X.D. Yang, Maggie L. Gordon, Bing Qi, Julius Pekar, Stuart Lo, Emily Seng-Yue, Alvin Mok, Brian C. Wilson, and I. Alex Vitkin, "High speed, wide velocity dynamic range Doppler optical coherence tomography (Part III): in vivo endoscopic imaging of blood flow in the rat and human gastrointestinal tracts," *Optics Express*, vol. **11**, no.19, pp.2416-2424, September 2003.

[25] C. A.Toth, et al, "A comparision of retinal morphology viewed by optical coherence tomography and light microscopy," *Archives of Ophthalmology*, vol. **115**, pp. 1425–1428, 1997.

[26] W. Drexler, U. Morgner, R. K. Ghanta, F. X. KÄrtner, J. S. Schuman, J. G. Fujimoto, "Ultrahigh-resolution ophthalmic optical coherence tomography," *Nature Medicine*, vol. **7**, no. 4, pp. 502-507, April 2001.

[27] B. Povazay, K. Bizheva, B. Hermann, A. Unterhuber, H. Sattmann, A. F. Fercher, W. Drexler, C. Schubert, P. K. Ahnelt, M. Mei, R. Holzwarth, W. Wadsworth, J. Knight, and P. Russell, ''Ultrahigh resolution ophthalmic optical coherence tomography with enhanced penetration,'' *Optics Express*, vol. **11**, no. 17, pp. 1980-1986, 2003.

[28] M. Wojtkowski, R. Leitgeb, A. Kowalczyk, T. Bajraszewski, and A. F. Fercher, "In vivo human retinal imaging by Fourier domain optical coherence tomography," *Journal of Biomedical*

Optics, vol. **7**, pp. 457-463, 2002.

[29] W. Drexler, H. Sattman, B. Hermann, T. H. Ko, M. Stur, A. Unterhuber, C. Scholda, O. Findl, M. Wirtitsch, J. G. Fujimoto, and A. F. Fercher, ‘‘Enhanced visualization of macular pathology using ultrahigh resolution optical coherence tomography,’’ *Archives of Ophthalmology*, vol. **121**, pp. 695-706, May 2003.

[30] C. K. Hitzenberger, “Three-dimensional imaging of the human retina by high-speed optical coherence tomography,” *Optics Express*, vol. **11**, pp. 2753-2761, 2003.

[31] M. Wojtkowski, T. Bajraszewski, I. Gorczynska, P. Targowski, A. Kowalczyk, W. Wasilewski, and C. Radzewicz, “Ophthalmic imaging by spectral optical coherence tomography,” *Am. J. Ophtalm.*, vol. **138,** pp. 412-419, 2004.

[32] U. S.-Erfurth, R. A. Leitgeb, S. Michels, B. Povaz˘ay, S. Sacu, B. Hermann, C. Ahlers, H. Sattmann, C. Scholda, A. F. Fercher, and W. Drexler, “Three-dimensional ultrahigh-resolution optical coherence tomography of macular diseases,” *Investigative Ophthalmology & Visual Science*, vol. **46**, no. 9, pp. 3393-3402, September 2005.

[33] R. J. Zawadzki, S. M. Jones and S. S. Olivier, M. Zhao, B. A. Bower and J. A. Izatt, S. Choi, S. Laut and J. S. Werner, “Adaptive-optics optical coherence tomography for high-resolution and high-speed 3D retinal in vivo imaging,” *Optics Express*, vol. **13**, no. 21, pp. 8532-8546, October 2005.

[34] V. J. Srinivasan, T. H. Ko, M. Wojtkowski, J. G. Fujimoto, “Noninvasive volumetric imaging and morphometry of the rodent retina with high-speed, ultrahigh-resolution optical coherence tomography,” *Investigative Ophthalmology & Visual Science*, vol. **47**, no. 12, December 2006.

[35] W. Tan, A. L. Oldenburg, J. J. Norman, T. A. Desai, S. A. Boppart, “Optical coherence tomography of cell dynamics in three-dimensional tissue models,” *Optics Express*, vol. **14**, no. 16, pp. 7159-7171, August 2006.

[36] A. Dubois, G. Moneron, K. Grieve and A. C. Boccara, “Three-dimensional cellular-level imaging using full-field optical coherence tomography,” *Physics in Medicine and Biology*, vol. **49**, pp. 1227-1234, 2004.

[37] C. Mason, J. F. Markusen, M. A. Town, P. Dunnill, and R. K. Wang, “The potential of optical

coherence tomography in the engineering of living tissue," *Physics in Medicine and Biology*, vol. **49**, pp. 1097-1115, 2004.

[38] http://www.microscopyu.com/articles/phasecontrast/phasemicroscopy.html.

[39] http://www.microscopyu.com/articles/dic/desenarmontdicintro.html.

[40] http://www.microscopyu.com/articles/polarized/polarizedintro.html.

[41] A.F. Fercher, C.K. Hitzenberger, G. Kamp, and S.Y. Elzaiat, "Measurement of intraocular distances by backscattering spectral interferometry," *Optics Communications*, vol. **117**, pp. 43-48, 1995.

[42] A. F. Fercher, ''Optical coherence tomography,'' *Journal of Biomedical Optics*, vol. **1**, pp. 157-173, 1996.

[43] G. Häusler and M. W. Lindner, ""Coherence radar" and "spectral radar"-new tools for dermatological diagnosis," *Journal of Biomedical Optics*, vol. **3**, pp. 21-31, 1998.

[44] Y. H. Zhao, Z. P. Chen, Z. H. Ding, H. W. Ren, J. S. Nelson, "Real-time phase-resolved functional optical coherence tomography by use of optical Hilbert transformation," *Optics Letters*, vol. **27**, no. 2, pp. 98-100, January 2002.

[45] U. Morgner, W. Drexler, F. X. Ka¨rtner, X. D. Li, C. Pitris, E. P. Ippen, and J. G. Fujimoto, ''Spectroscopic optical coherence tomography,'' *Optics Letters*, vol. **25**, no. 2, pp. 111-113, 2000.

[46] N. A. Nassif, B. Cense, B. H. Park, M. C. Pierce, et al., "In vivo high resolution video-rate spectral-domain optical coherence tomography of the human retina and optic nerve," *Optics Express*, vol. **12**, 367, 2003.

[47] R. A. Leitgeb, L. Schmetterer, C. K. Hitzenberger, A. F. Fercher, F. Berisha, M. Wojtkowski, and T. Bajraszewski, "Real-time measurement of in vitro flow by Fourier-domain color Doppler optical coherence tomography," *Optics Letters*, vol. **29**, pp. 171-173, 2004.

[48] M. Wojtkowski, V. J. Srinivasan, T. H. Ko, J. G. Fujimoto, A. Kowalczyk, J. S. Duker, "Ultrahigh-resolution, high-speed, Fourier domain optical coherence tomography and methods for dispersion compensation," *Optics Express*, vol. **12**, no. 11, pp. 2404-2422, May 2004.

[49] G. Moneron, A. C. Boccara, and A. Dubois, "Stroboscopic ultrahigh-resolution full-field optical coherence tomography," *Optics Letters*, vol. **30**, no. 11, pp. 1351-1353, June 2005.

[50] K. Grieve1, A. Dubois, M. Simonutti, M. Paques, J. Sahel, J.-Franc¸ois Le Gargasson, C.

Boccara, “In vivo anterior segment imaging in the rat eye with high speed white light full-field optical coherence tomography,” *Optics Express*, vol. **13**, no. 16, pp. 6286-6295, August 2005.

[51] J. Ai, L. V. Wang, “Synchronous self-elimination of autocorrelation interference in Fourier-domain optical coherence tomography,” *Optics Letters*, vol. **30**, no. 21, pp. 2939-2941, November 2005.

[52] S. L. Jiao, R. Knighton, X. R. Huang, G. Gregori, and C. A. Puliafito, “Simultaneous acquisition of sectional and fundus ophthalmic images with spectral-domain optical coherence tomography,” *Optics Express*, vol. **13**, pp. 444-452, 2005.

[53] A. Dubois, G. Moneron, C. Boccara, “Thermal-light full-field optical coherence tomography in the 1.2 lm wavelength region,” *Optics Communications*, vol. **266**, pp. 738–743, 2006.

[54] J. M. Schmitt, “Optical coherence tomography (oct): A review,” *IEEE J. Selected Topics in Quantum Electronics*, vol. **5**, no. 4, pp. 1205-1215, Jul./Aug. 1999.

[55] D. J. Derickson, P. A. Beck, T. L. Bagwell, D. M. Braun, J. E. Fouquet, F. G. Kellert, M. J. Ludowise, W. H. Perez, T. R. Ranganath, G. R. Trott, and S. R. Sloan, “High-power, low-internal-reflection, edge emitting light-emitting diodes,” *Hewlett-Packard Journal.*, vol. **46**, pp. 43-49, Feb. 1995.

[56] B. Bouma, G. J. Tearney, S. A. Boppart, M. R. Hee, M. E. Brezinski, and J. G. Fujimoto, "High-resolution optical coherence tomogpaphic imaging using a mode-locked Ti: laser source", *Optics Letters*, vol. **20**, 1486-1488, 1995.

[57] A. Unterhuber, B. Hermann, H. Sattmann, B. Povazay, W. Drexler, G. Tempea, V. Yakovlev, C. Schubert, E. M. Anger, P. K. Ahnelt, M. Stur, J. E. Morgan, T. Le, and A. Stingl, ‘‘Compact, low cost Ti:Al_2O_3 laser for in vivo ultrahigh resolution optical coherence tomography,’’ *Optics Letters*, vol. **28**, no. 11, pp. 905-907, 2003.

[58] Y. Wang, Y. Zhao, J. S. Nelson, Z. Chen, and R. S. Windeler, “Ultrahigh-resolution optical coherence tomography by broadband continuum generation from a photonic crystal fiber,” *Optics*

Letters, vol. **28**, no. 3, pp.182-184, Feb. 2003.

[59] H. Lim, Y. Jiang, Y. Wang, Y. C. Huang, Z. Chen, and F. W. Wise, "Ultrahigh-resolution optical coherence tomography with a fiber laser source at 1 m m," *Optics Letters*, vol. **30**, no. 10, pp. 1171-1173, May 2005.

[60] L. Vabre, A. Dubois, and A. C. Boccara, "Thermal-light full-field optical coherence tomography," *Optics Letters*, vol. **27**, no. 7, April 2002.

[61] J. L. Boulnois, "Photophysical processes in recent medical laser developement: A review," *Lasers in Medical Science*, vol. **1**, pp.47-66, 1986.

[62] J. P. Ritz, A. Roggan, C. Isbert, etc.., "Optical properties of native and coagulated porcine liver tissue between 400 and 2400 nm," *Lasers in Surgery and Medicine*, vol. **29**, pp. 205-212, 2001.

[63] A. F. Fercher, W. Drexler, C. K. Hitzenberger and T. Lasser, "Optical coherence tomography --principles and applications," *Reports on Progress in Physics*, vol. **66**, pp. 239-303, Jan. 2003.

[64] P. H. Tomlins and R. K. Wang, "Theory, developments and applications of optical coherence tomography," *Journal of Physics D: Applied Physics*, vol. **38**, pp. 2519–2535, 2005.

[65] C. K. Hitzenberger, M. Danner, W. Drexler, and A. F. Fercher, "Measurement of the spatial coherence of superluminescent diodes," *Journal of Modern Optics*, vol. **46**, pp. 1763-1774, 1999.

[66] http://www.femtolasers.com/.

[67] http://www.newport.com/.

[68] S. Machida, Y. Yamamoto, "Quantum-limited operation of balanced mixer homodyne and heterodyne receivers," *IEEE Journal of Quantum Electronics*, vol. **qe-22**, no. 5, pp. 617-624, May 1986.

[69] K. Takada, "Noise in optical low-coherence reflectometry," *IEEE Journal of Quantum Electronics*, vol. **34**, no. 7, pp. 1098-1108, July 1998.

[70] A. Rollins and J. A. Izatt, "SNR analysis of conventional and optimal fiber optic

low-coherence interferometer topologies," *Proceedings of SPIE*, vol. **3915**, pp. 60-67, 2000.

[71] J. F. de Boer, B. Cense, B. H. Park, M. C. Pierce, G. J. Tearney, and B. E. Bouma, "Improved signal-to-noise ratio in spectral-domain compared with time-domain optical coherence tomography," *Optics Letters*, vol. **28**, pp. 2067-2069, 2003.

[72] C. H. Yang, "Molecular contrast optical coherence tomography: A Review," *Photochemistry and Photobiology*, vol. **81**, pp. 251-237, 2005.

[73] K. D. Rao, M. A. Choma, S. Yazdanfar, A. Rollins, J. A. Izatt, "Molecular contrast in optical coherence tomography by use of a pump-probe technique," *Optics Letters*, vol. **28**, pp. 340-342, 2003.

[74] C. Yang, M. A. Choma, L. A. Lamb, J. D. Simon, J. A. Izatt, "Protein-based molecular contrast optical coherence tomography with phytochrome as the contrast agent," *Optics Letters*, vol. **29**, pp. 1396-1399, 2004.

[75] T. M. Lee, A. L. Oldenburg, S. Sitafalwalla, D. L. Marks, W. Luo, F. J.-J. Toublan, et al., "Engineered microsphere contrast agents for optical coherence tomography," *Optics Letters*, vol. **8**, pp. 1546-1548, 2003.

[76] C. Vinegoni, J. S. Bredfeldt, D. L. Marks, S. A. Boppart, "Nonlinear optical contrast enhancement for optical coherence tomography," *Optics Express*, vol. **12**, no. 2, pp. 331-340, 2004.

[77] Model 2007 user's manual about Nirvana auto-balanced photoreceivers, http://www.newfocus.com.

[78] K. G. Larkin, "Efficient nonlinear algorithm for envelope detection in white light interferometry," *J. Opt. Soc. Am. A*, vol. **13**, no. 4, pp. 832-843, April 1996.

[79] M. Takeda, H. Ina, S. Kobayashi, "Fourier-transform method of fringe-pattern analysis for computer-based topography and interferometry," *J. Opt. Soc. Am.*, vol. **72**, no. 1, pp. 156-160, Jan. 1982.

[80] K. Yu, L. Ji, L. Wang, P. Xue, "How to optimize OCT image," *Optics Express*, vol. **9**, no. 1,

July 2001.

[81] Y. Pan, E. Lankenau, J. Welzel, R. Birngruber, and R. Engelhardt, "Optical coherence—gated imaging of biological tissues," *IEEE Journal of Selected Topics in Quantum Electronics*, vol. **2**, no. 4, pp. 1029-1034, December 1996.

[82] C. B. Su, "Achieving variation of the optical path length by a few millimeters at millisecond rates for imaging of turbid media and optical interferometry: a new technique," *Optics Letters*, vol. **22**, no. 10, pp. 665-667, May 1997.

[83] N. G. Chen and Q. Zhu, "Rotary mirror array for high-speed optical coherence tomography," *Optics Letters*, vol. **27**, no. 8, pp. 607-609, April 2002.

[84] L. B. Liu and N. G. Chen, "Double-pass rotary mirror array for fast scanning optical delay line," Applied Optics, vol. **45**, no. 21, pp. 5426-5431, July 2006.

[85] G. J. Tearney, B. E. Bouma, S. A. Boppart, B. Golubovic, E. A. Swanson and J. G. Fujimoto, "Rapid acquisition of in vivo biological images by use of optical coherence tomography," *Optics Letters*, vol. **21**, no. 17, pp. 1408-1410, September 1996.

[86] J. P. Heritage, A. M. Weiner, and R. N. Thurston, "Picosecond pulse shaping by spectral phase and amplitude manipulation," *Optics Letters*, vol. **10,** no. 12, pp. 609-611, Dec. 1985.

[87] K. F. Kwong, D. Yankelevich, K. C. Chu, J. P. Heritage, and A. Dienes, "400-Hz mechanical scanning optical delay line," *Optics Letters*, vol. **18**, no. 7, pp. 558-560, April 1993.

[88] G. J. Tearney, B. E. Bouma, and J. G. Fujimoto, "High-speed phase- and group-delay scanning with a grating-based phase control delay line," *Optics Letters*, vol. **22**, no. 23, pp. 1811-1813, Dec. 1997.

[89] Andrew M. Rollins, Manish D. Kulkarni, Siavash Yazdanfar, Rujchai Ung-arunyawee, Joseph A. Izatt, "In vivo video rate optical coherence tomography," *Optics Express*, vol. **3**, no. 6, pp. 219-229, Sep. 1998.

[90] W. Drexler, U. Morgner, F. X. K¨artner, C. Pitris, S. A. Boppart, X. D. Li, E. P. Ippen, and J. G. Fujimoto, "In vivo ultrahigh-resolution optical coherence tomography," *Optics Letters*, vol. **24**, no. 17, pp. 1221-1223, Sep. 1999.

[91] Amy L. Oldenburg, J. Joshua Reynolds, Daniel L. Marks, and Stephen A. Boppart, "Fast-Fourier-domain delay line for in vivo optical coherence tomography with a polygonal scanner," *Applied Optics*, vol. **42,** no. 22, pp. 4606-4611, Aug. 2003.

[92] A. D. Aguirre, P. Hsiung, T. H. Ko, I. Hartl, and J. G. Fujimoto, "High-resolution optical coherence microscopy for high-speed, in vivo cellular imaging," *Optics Letters*, vol. **28**, no. 21, pp. 2064-2066, Nov. 2003.

[93] S. Bourquin, A. D. Aguirre, I. Hartl, P. Hsiung, T. H. Ko and J. G. Fujimoto, "Ultrahigh resolution real time OCT imaging using a compact femtosecond Nd:Glass laser and nonlinear fiber," *Optics Express*, vol. **11**, no. 24, pp. 3290-3297, Dec. 2003.

[94] B. E. Bouma and G. J. Tearney, *Handbook of Optical Coherence Tomography*, New York, Basel: Marcel Dekker Inc., 2002.

[95] G. J. Tearney, S. A. Boppart, B. E. Bouma, M. E. Brezinski, N. J. Weissman, J. F. Southern and J. G. Fujimoto, "Scanning single-mode fiber optic catheter–endoscope for optical coherence tomography," *Optics Letters*, vol. **21**, no. 7, pp. 543-545, April 1996.

[96] G. J. Tearney, M. E. Brezinski, B. E. Bouma, S. A. Boppart, C. Pitvis, J. F. Southern, and J. G. Fujimoto, "In vivo endoscopic optical biopsy with optical coherence tomography," *Science*, vol. **276**, no. 5321, pp. 2037-2039, 1997.

[97] F. I. Feldchtein, G. V. Gelikonov, V. M. Gelikonov, R. V. Kuranov, A. M. Sergeev, "Endoscopic applications of optical coherence tomography," *Optics Express*, vol. **3**, no. 6, pp. 257-270, September 1998.

[98] A. M. Sergeev, V. M. Gelikonov, G. V. Gelikonov, F. I. Feldchtein, R. V. Kuranov, N. D. Gladkova, N. M. Shakhova, L. B. Snopova, A. V. Shakhov, I. A. Kuznetzova, A. N. Denisenko, V. V. Pochinko, Yu. P. Chumakov, O. S. Streltzova, "In vivo endoscopic OCT imaging of precancer and cancer states of human mucosa," *Optics Express*, vol. **1**, no. 13, pp. 432-440, December 1997.

[99] S. A. Boppart, B. E. Bouma, C. Pitris, G. J. Tearney, J. G. Fujimoto, M. E. Brezinski, "Forward-imaging instruments for optical coherence tomography," *Optics Letters*, vol. **22**, no. 21, pp. 1618-1620, November 1997.

[100] X.D. Li, W. Drexler, C. Pitris, R. Ghanta, C. Jesser, J. Herrmann, D. Stamper, D. Golden, S. Martin, J.G. Fujimoto, M. Brezinski, "Imaging of osteoarthritlc cartilage with optical coherence tomography: micronstructure and polarization sensitivity," *IEEE Conference on Lasers and Electro-Optics (CLEO)*, CWP5, 1999.

[101] B. E. Bouma and G. J. Tearney, "Power-efficient nonreciprocal interferometer and linear-scanning fiber-optic catheter for optical coherence tomography," *Optics Letters*, vol. **24**, no.

8, pp. 531-533, April 1999.

[102] H. A. Haus, *Waves and fields in optoelectronics*, New Jersey, Englewood Cliffs: Prentice-Hall Inc., 1984.

[103] F. Lexer, C.K. Hitzenberger, W. Drexler, S. Molebny, H. Sattmann, M. Sticker, and A.F. Fercher, "Dynamic coherent focus OCT with depth-independent transversal resolution," *Journal of Modern Optics*, vol. **46**, pp. 541-553, 1999.

[104] B. Qi, A. P. Himmer, L. M. Gordon, X. D. V. Yang, L. D. Dickensheets, and I. A. Vitkin, "Dynamic focus control in high-speed optical coherence tomography based on a microelectromechanical mirror," *Opt. Commun.*, vol. **232**, pp. 123-128, 2004.

[105] M. J. Cobb, X. M. Liu, and X. D. Li, "Continuous focus tracking for real-time optical coherence tomography," *Optics Letters*, vol. **30**, pp. 1680-1682, 2005.

[106] A. Divetia, T. H. Hsieh, J. Zhang, Z. P. Chen, M. Bachman, and G. P. Li, "Dynamically focused optical coherence tomography for endoscopic applications," *Appl. Phys. Lett.*, vol. **86**, #103902, 2005.

[107] D. Koozekanani, K. Boyer, and C. Roberts, "Retinal thickness measurements from optical coherence tomography using a Markov boundary model", *IEEE Transactions on Medical Imaging*, vol. **20**, no. 9, pp. 900-916, September 2001.

[108] T. S. Ralston, D. L. Marks, F. Kamalabadi, and S. A. Boppart, "Deconvolution methods for mitigation of transverse blurring in optical coherence tomography", *IEEE Transactions on Image Processing*, vol. **14**, no. 9, pp. 1254-1264, Sep. 2002.

[109] J. Rogowska, C. M. Bryant, M. E. Brezinski, "Cartilage thickness measurements from optical coherence tomography," *J. Opt. Soc. Am. A*, vol. **20**, no. 2, pp. 357-367, Feb. 2003.

[110] R. A. Costa, D. Calucci, Mirian Skaf, J. A. Cardillo, J. C. Castro, L. A. Melo, Jr, M. C. Martins, and P. K. Kaiser, "Optical coherence tomography 3: automatic delineation of the outer neural retinal boundary and its influence on retinal thickness measurements", *Investigative Ophthalmology & Visual Science*, vol. **45**, no. 7, pp. 2399-2406, July 2004.

[111] A. Herzog, K. L. Boyer, and C. Roberts, "Robust extraction of the optic nerve head in optical coherence tomography", *CVAMIA-MMBIA 2004*, LNCS **3117**, pp. 395–407, 2004.

[112] D. C. Fernández, "Delineating fluid-filled region boundaries in optical coherence tomography images of the Retina," *IEEE Transactions on Medical Imaging*, vol. **24**, no. 8, pp. 929-945, Aug. 2005.

[113] D. C. Fernández, H. M. Salinas, C. A. Puliafito, "Automated detection of retinal layer structures on optical coherence tomography images", *Optics Express*, vol. **13**, no. 25, pp. 10200-10216, Dec. 2005.

[114] K. L. Boyer, A. Herzog, and C. Roberts, "Automatic recovery of the optic nervehead geometry in optical coherence tomography", *IEEE Transactions on Medical Imaging*, vol. **25**, no. 5, pp. 553-570, May 2006.

[115] J. M. Schmitt, S. H. Xiang, and K. M. Yung, "Speckle in optical coherence tomography", *Journal of Biomedical Optics*, vol. **4**, no.1, pp. 95–105, January 1999.

[116] P. Perona and J. Malik, "Scale-space and edge detection using anisotropic diffusion," *IEEE Transaction on Pattern Analysis and Machine Intelligence*, vol. **12**, no. 7, pp. 629–639, Jul. 1990.

[117] X. Hao, S. Gao, and X. Gao, "A novel multiscale nonlinear thresholding method for ultrasonic speckle suppressing," *IEEE Transactions on Medical Imaging*, vol. **18**, no. 9, pp. 787–794, Sep. 1999.

[118] J. S. Jin, Y. Wang, and J. Hiller, "An adaptive nonlinear diffusion algorithm for filtering medical images," *IEEE Trans. Inform. Technol. Biomed.*, vol. **4**, pp. 298–305, Dec. 2000.

[119] Y. Chen, C.A.Z. Barcelos and B. A. Mairz, "Smoothing and edge detection by time-varying coupled nonlinear diffusion equations", *Computer Vision and Image Understanding*, vol. **82**, pp. 85-100, 2001.

[120] Y. Yu and S. T. Acton, "Speckle reducing anisotropic diffusion", *IEEE Transactions on Image Processing*, vol. **11**, no. 11, pp. 1260-1270, Nov. 2002.

[121] G. Gilboa, N. Sochen, and Y. Y. Zeevi, " Image enhancement and denoising by complex

diffusion processes," *IEEE Transactions on Pattern Analysis and Machine Intelligence*, vol. **26**, no. 8, pp. 1020-1036, Aug., 2004.

[122] F. Zhang, Y. M. Yoo, L. M. Koh, and Y. Kim, "Nonlinear diffusion in laplacian pyramid domain for ultrasonic speckle reduction", *IEEE Transactions on Medical Imaging*, vol. **26**, no. 2, pp. 200-211, Feb. 2007.

[123] J. Weickert, "Coherence-enhancing diffusion of colour images", *Image and Vision Computing*, vol. **17**, pp. 201–212, 1999.

[124] P. Mrázek, "Selection of optimal stopping time for nonlinear diffusion filtering", *International Journal of Computer Vision*, vol. **52**, pp. 189–203, May 2003.

[125] C. A. Z. Barcelos, M. Boaventura and E. C. S. JR., "Edge detection and noise removal by use of a partial differential equation with automatic selection of parameters", *Computational and Applied Mathematics*, vol. **24**, no. 1, pp. 131-150, 2005.

[126] H. M. Salinas and D. C. Fernández, "Comparison of PDE-based nonlinear diffusion approaches for image enhancement and denoising in optical coherence tomography", *IEEE Transactions on Medical Imaging*, vol. **26**, no. 6, pp. 761-771, June 2007.

[127] Z. Wang, A. C. Bovik, H. R. Sheikh, and E. P. Simoncelli, "Image quality assessment: from error visibility to structural similarity", *IEEE Transactions on Image Processing*, vol. **13**, no. 4, pp. 600-612, April 2004.

[128] G. Lin, U. Adiga, K. Olson, J.F. Guzowski, C.A. Barnes, and B.Roysam, "A hybrid 3D watershed algorithm incorporating gradient cues and object models for automatic segmentation of nuclei in confocal image stacks," *Cytometry A.* , vol. **56**, no. 1, pp.23-36, Nov. 2003.

[129] S. Kumara, S.H. Ong, S. Ranganatha, T.C. Ong, F.T. Chew， "A rule-based approach for robust clump splitting", *Pattern Recognition*, vol. **39**, pp. 1088 – 1098, 2006.

[130] Y. L. Fok, J. C. K. Chan, and R. T. Chin, "Automated analysis of nerve-cell images using active contour models", *IEEE Transactions on Medical Imaging*, vol. **15**, no. 3, pp. 353-368, June

1996.

[131] D.P. Mukherjee, N. Ray, S.T. Acton, "Level set analysis for leukocyte detection and tracking", *IEEE Transactions on Image Processing*, vol. **13**, no.4, pp. 562 – 572, April 2004.

[132] J. N. Tsitsiklis. "Efficient algorithm for globally optimal trajectories", *IEEE Transactions on Automatic Control*, vol. **40,** no. 9, pp. 1528–1538, 1995.

[133] J. A. Sethian, "A fast marching level set method for monotonically advancing fronts", *Proceedings of the National Academy of Sciences of the United States of America*, vol. **93**, pp. 1591-1595, Feb. 1996.

[134] L. D. Cohen, R. Kimmel, "Global minimum for active contour models: a minimal path approach", *International Journal of Computer Vision*, vol. **24**, no. 1, pp. 57–78, August 1997.

[135] T. Deschamps, L. D. Cohen, "Fast extraction of minimal paths in 3D images and applications to virtual endoscopy", *Medical Image Analysis*, vol. **5**, no. 4, August 2001.

[136] G. J. M. Parker, C. A. M. Wheeler-Kingshott, G. J. Barker, "Estimating distributed anatomical connectivity using fast marching methods and diffusion tensor imaging," *IEEE Transactions on Medical Imaging*, vol. **21**, no. 5, pp. 505-512, May 2002.

[137] P. E. Danielsson and Q. Lin, "A modified fast marching method", *Lecture Notes in Computer Science*, vol. **2749**, pp. 1154−1161, 2003.

[138] M.H. R. Cardinal, J. Meunier, G. Soulez, R. L. Maurice, É. Therasse, and G. Cloutier, "Intravascular ultrasound image segmentation: a three-dimensional fast-marching method based on gray level distributions," *IEEE Transactions on Medical Imaging*, vol. **25**, no. 5, May 2006, pp. 590-601.

Appendix A: Interferometric signal

The wave theory of light provides a natural basis to analyze the OCT interferometric signal. The electric and magnetic fields are vector fields. Light is, of course, a vector phenomenon. In fact, as the electric part of light E is considerably more effective at exerting forces and doing work on charges than that of the magnetic part of light B, and the effect of B on OCT signal will be ignored.

Consider the simplified schematic of OCT system shown in Figure 1.1. The incident optical wave E_0 is split to reference and sample fields, E_R and E_S at the beamsplitter. The reference mirror and sample are positioned at distances l_R and l_S from the beamsplitter respectively.

If the light source is monochromatic, the sample and reference fields may be represented by wave functions

$$\vec{E}_R = E_r(\vec{r})\cos[wt + f_r(\vec{r})] \quad \text{and} \quad \vec{E}_S = E_s(\vec{r})\cos[wt + f_s(\vec{r})] \qquad \text{(A1)}$$

where E_r and E_s are the field amplitudes of the reference and sample arms.

w is the angular frequency of the light source.

f_r and f_s is the relative phase of the reference and sample optical fields.

In addition, the sample and reference fields may be expressed in phasor form :

$$E_R = E_r e^{-j(2b_r l_r - wt)} \quad \text{and} \quad E_S = E_s e^{-j(2b_s l_s - wt)} \qquad \text{(A2)}$$

where b is the propagation constant.

The time averaged photocurrent I at the detector is given by

$$I = \frac{he}{hn} \cdot \frac{|E_R + E_S|^2}{2h_0} = \frac{he}{2hnh_0} \cdot I_D \qquad \text{(A3)}$$

where h is the detector quantum efficiency, e is the electronic charge, hn is the photon

energy, and h_0 is the intrinsic impedance of free space.

Assume the beamsplitter has 50% splitting ratio, then

$$E_r = E_s = \frac{1}{2}E_0 \tag{A4}$$

Assuming that the reference optical field is parallel to the sample optical field, the superposition of the optical fields at the detector may be written as:

$$\begin{aligned} I_D &= |E_R + E_S|^2 = \frac{1}{2}|E_r|^2 + \frac{1}{2}|E_s|^2 + \frac{1}{4}E_R{}^* E_S + \frac{1}{4}E_R E_S{}^* \\ &= \frac{1}{2}|E_r|^2 + \frac{1}{2}|E_s|^2 + \frac{1}{2}real\{E_R{}^* E_S\} \\ &= \frac{1}{2}I_r + \frac{1}{2}I_s + \frac{1}{2}\sqrt{I_r I_s}\cos(2b_r l_r - 2b_s l_s + f(t)) \\ &= \frac{1}{2}I_r + \frac{1}{2}I_s + \frac{1}{2}\sqrt{I_r I_s}\cos(\Delta j) \end{aligned} \tag{A5}$$

where $f(t)$ is the relative phase difference between the reference and sample waves.

If $f(t) = 0$, $b_r = b_s = b = \frac{2p}{nl}$, then the phase difference between the two optical fields is given by

$$\Delta j = \frac{2p}{nl}(2l_r - 2l_s) = \frac{2p\Delta l}{nl} \tag{A6}$$

In equation (A5), the first two terms at the right side represent the DC component of the signal, while the last term is the oscillatory AC component which represents the interference term between the reference and sample optical fields. This last term varies sinusoidally and is contained in the real part of the cross-spectral term $E_R{}^* E_S$.

In fact, any real light source has a finite spectral bandwith and is not monochromatic. The interference term of the light source can be obtained by integrating over the harmonic content of the light source. The photocurrent of the detector is proportional to the interference term,

$$I \propto real\{\int_{-\infty}^{\infty} E_R(w)E_S(w) * \frac{dw}{2p}\} = real\{\int_{-\infty}^{\infty} S(w)e^{-j\Delta j} * \frac{dw}{2p}\} \tag{A7}$$

where

$$S(w) = E_r(w)E_s(w), \tag{A8}$$

and $$\Delta f(w) = 2b_r(w)l_r - 2b_s(w)l_s, \tag{A9}$$

If the sample optical field has the identical spectral component as the reference optical field, then $S(w)$ is the power spectral density of the light source, and $\Delta f(w)$ is the phase difference between each frequency component of the two fields.

Assuming that the spectrum of light source is bandlimited with a center frequency of w_0, the propagation constant b may be rewritten using first-order Taylor expansion :

$$b_r(w) = b_s(w) = b(w_0) + b'(w_0)(w - w_0) \tag{A10}$$

Then equation (A7) becomes:

$$\begin{aligned} I \propto real\{\int_{-\infty}^{\infty} S(w)e^{-j\Delta l b(w)} * \frac{dw}{2p}\} &= real\{\int_{-\infty}^{\infty} S(w)e^{-j\Delta l[b(w_0)+b'(w_0)(w-w_0)]}\frac{dw}{2p}\} \\ &= real\{e^{-jb(w_0)\Delta l}\int_{-\infty}^{\infty} S(w)e^{-jb'(w_0)(w-w_0)\Delta l}\frac{dw}{2p}\} \\ &= real\{e^{-jw_0\Delta t_p}\int_{-\infty}^{\infty} S(w)e^{-j(w-w_0)\Delta t_g}\frac{dw}{2p}\} \end{aligned} \tag{A11}$$

where Δt_p and Δt_g are the phase and group delays defined as

$$\Delta t_p = \frac{b(w_0)}{w_0}\Delta l = \frac{\Delta l}{v_p} \tag{A12}$$

$$\Delta t_g = b'(w_0)\Delta l = \frac{\Delta l}{v_g} \tag{A13}$$

where v_p, v_g are the phase and group velocities.

Equation (A11) shows that interferometric term of the photocurrent consists of a carrier and an envelope. The envelope will determine the axial point spread function of the interferometer.

Appendix B: Signal to noise ratio (SNR)

B.1. Receiver noise

The receive noise is the total noise in the photodiode detector. It mainly has three components which are thermal noise, temperature noise and amplifier noise. The receiver noise is the most important noise in OCT system and greatly affects the system signal to noise.

Thermal noise arises from the random motion of electrons in the photodiode resistor and can be given by

$$s_{th}^2 = \frac{4k_B TB}{R_{eff}} \tag{B1}$$

Where k_B is Boltzmann's constant, T is the temperature, and B is the electronic detection bandwidth. R_{eff} is the effective load resistance.

The temperature noise is caused by the random fluctuations in temperature between the detector and its environment. It can be expressed as

$$s_{temp}^2 = 4k_B T^2 KB \tag{B2}$$

If the background is assumed to be in equilibrium with the detector, $K = 4e s T^3 A$, where e is the permeability, s is Stefan-Boltzmans constant and A is the detector area.

The amplifier noise is given by

$$s_{amp}^2 = \frac{G^2 B 4k_B (T_A + T_R)}{R_{eff}} \tag{B3}$$

G is the amplifier gain, T_A is the amplifier noise temperature and T_R is the noise temperature of the detector load resistance.

In fact, it is difficult in evaluating the receiver noise due to several parameters which have effect on. A relatively lower limit value can be found by using input current noise (ICN) or the

noise equivalent power (NEP) obtained from the manufacturer specifications.

$$ICN = 3pA/\sqrt{Hz} \tag{B4}$$

Then an estimate value for receiver noise can be given by

$$s_{rec}^{2} = (ICN)^{2} B \tag{B5}$$

B.2. Shot noise

Photon shot noise is caused by quantization of the light, i.e. the photocurrent consists of photons with certain energy, and therefore it does not "float" as a continuous medium. Thus, the random arrival of photons is detected as noise. The photon shot noise can be written as

$$s_{shot}^{2} = 2qBi_{dc} \tag{B6}$$

Where q is the free electron charge, and i_{dc} is the mean detector photocurrent given by

$$i_{dc} = S_{v}(P_{ref} + P_{inc}) \tag{B7}$$

B.3. Intensity noise/beat noise

An excess intensity noise arises from the time fluctuations of the intensity and is given by

$$s_{ex}^{2} = (1+V^{2}) i_{dc}^{2} \frac{B}{\Delta v} \tag{B8}$$

Where V is the light source degree of polarization, B is the electrical bandwidth, Δv is the effective bandwidth given by

$$\Delta v = \sqrt{\frac{p}{2\ln 2}} c \frac{\Delta l}{l_{0}^{2}} \tag{B9}$$

B.4. Suppressing noise in OCT system

Effectively suppressing noise will improve system sensitivity. High SNR of the OCT system will accurately detect very low intensity levels of backscattered light. To achieve high SNR, we adopt dual balanced detection technique. Dual balanced detection technique can be used to suppress the excess laser noise within an OCT system and operate closer to the shot noise limit. Its

basic theory is shown in Figure B.1.

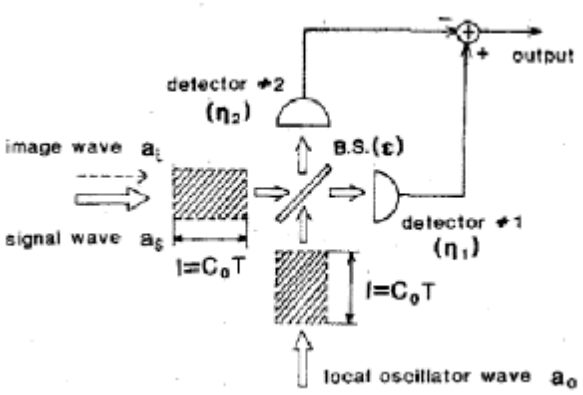

Figure B.1. A balanced receiver

Assume that the signal wave is expressed as $\hat{a}_s = (A_s + \Delta\hat{A}_s)e^{j(w_0+w_{if})t}$ and a local oscillator wave is expressed as $\hat{a}_0 = (A_0 + \Delta\hat{A}_0)e^{jw_0 t}$, where A_s and A_0 are the average amplitudes (positive real), $\Delta\hat{A}_s$ and $\Delta\hat{A}_0$ are the fluctuation operators which consist of two Hermitian quadrature noise components.

$$\Delta\hat{A}_s = \Delta\hat{A}_{s1} + j\Delta\hat{A}_{s2} \tag{B10}$$

The photocurrent $\hat{I}_1$ that has been measured in photodetector 1 can be represented as

$$\hat{I}_1 = \frac{2eh_1}{T}\sqrt{e(1-e)}A_0[A_s\cos(w_{if}t) + \frac{1-e}{2e}A_0 + \frac{1-e}{e}\Delta\hat{A}_{01} + \frac{1-h_1}{eh_1}\Delta\hat{C}_{01}$$
$$+\left\{\Delta\hat{A}_{s1} + \Delta\hat{A}_{i1} + \frac{1-h_1}{eh_1}(\Delta\hat{C}_{s1} + \Delta\hat{C}_{i1})\right\}\cos(w_{if}t)$$
$$+\left\{-\Delta\hat{A}_{s2} + \Delta\hat{A}_{i1} + \frac{1-h_1}{eh_1}(-\Delta\hat{C}_{s2} + \Delta\hat{C}_{i2})\right\}\sin(w_{if}t)] \tag{B11}$$

The photocurrent $\hat{I}_2$ that has been measured in photodetector 2 can be similarly represented as

$$\hat{I}_2 = \frac{2eh_2}{T}\sqrt{e(1-e)}A_0[-A_s\cos(w_{if}t) + \frac{1}{2}\sqrt{\frac{e}{1-e}}A_0 + \sqrt{\frac{e}{1-e}}\Delta\hat{A}_{01} + \sqrt{\frac{h_2}{(1-e)h_2}}\Delta\hat{A}_{01}$$

$$+\left\{-\Delta\hat{A}_{s1}-\Delta\hat{A}_{i1}+\sqrt{\frac{1-h_2}{(1-e)h_2}}(\Delta\hat{d}_{s1}+\Delta\hat{d}_{i1})\right\}\cos(w_{if}t)$$

$$+\left\{\Delta\hat{A}_{s2}-\Delta\hat{A}_{i2}+\sqrt{\frac{1-h_2}{(1-e)h_2}}(-\Delta\hat{d}_{s2}+\Delta\hat{d}_{i2})\right\}\sin(w_{if}t)] \qquad \text{(B12)}$$

The subtracted output current between two detectors following the intermediate frequency (IF) bandpass filtering measures

$$\hat{I}_1-\hat{I}_2=\frac{2e(h_1+h_2)}{T}\sqrt{e(1-e)}A_0[A_s\cos(w_{if}t)+\frac{h_1\sqrt{(1-e)/e}-h_2\sqrt{e/(1-e)}}{h_1+h_2}\Delta\hat{A}_{01}$$

$$+\left\{\Delta\hat{A}_{s1}+\Delta\hat{A}_{i1}+\sqrt{\frac{h_1(1-h_1)/e}{h_1+h_2}}(\Delta\hat{C}_{s1}+\Delta\hat{C}_{i1})-\sqrt{\frac{h_2(1-h_2)/(1-e)}{h_1+h_2}}(\Delta\hat{d}_{s1}+\Delta\hat{d}_{i1})\right\}\cos(w_{if}t)$$

$$+\left\{-\Delta\hat{A}_{s2}+\Delta\hat{A}_{i2}+\sqrt{\frac{h_1(1-h_1)/e}{h_1+h_2}}(-\Delta\hat{C}_{s2}+\Delta\hat{C}_{i2})-\sqrt{\frac{h_2(1-h_2)/(1-e)}{h_1+h_2}}(\Delta\hat{d}_{s1}+\Delta\hat{d}_{i1})\right\}\sin(w_{if}t)]$$

(B13)

From equation (B13), it can be seen that the subtracted output current between two detectors can cancel out the background and intensity noise (the product of A_0 and $\Delta\hat{A}_{01}$) as well as DC photocurrent. However, due to the p phase difference introduced at the beam splitter, the interference signals (the product of A_s and A_0) do not cancel but instead add at the two detectors.

For 50/50 fiber optic coupler, light traveling in a "bar" path through it (ie, from an upper port to a lower port or vice versa) obtains a $-p/2$ phase shift relative to the light that travels in a "cross" path (ie, from an upper port to an upper port, or lower port to a low port).

Appendix C: Simulation results of FD_ODL

C.1. Below is some simulation results about FD_ODL. To simplify the analysis, assume that $\Delta y = 0.00$, $\Delta z = 0.00$.

Unit: degree

Table C1 Diffraction angle for wavelength $l = 900nm$

q' ($l = 900nm$)	Rotation angle of scanning mirror (a)	g'	$\Delta g'_{deflection}$
3.43981283	-4.5	28.72321873	0.03781623
3.43981283	-4.0	28.71521555	0.02981305
3.43981283	-3.5	28.70818342	0.02278092
3.43981283	-3.0	28.70211114	0.01670864
3.43981283	-2.5	28.69698911	0.01158661
3.43981283	-2.0	28.69280925	0.00740675
3.43981283	-1.5	28.68956501	0.00416251
3.43981283	-1.0	28.68725131	0.00184880
3.43981283	-0.5	28.68586452	0.00046202
3.43981283	0.0	28.68540250	0.00000000
3.43981283	0.5	28.68586452	0.00046202
3.43981283	1.0	28.68725131	0.00184880
3.43981283	1.5	28.68956501	0.00416251
3.43981283	2.0	28.69280925	0.00740675
3.43981283	2.5	28.69698911	0.01158661

3.43981283	3.0	28.70211114	0.01670864
3.43981283	3.5	28.70818342	0.02278092
3.43981283	4.0	28.71521555	0.02981305
3.43981283	4.5	28.72321873	0.03781623

Table C2 Diffraction angle for wavelength $l = 850nm$

$q'(l = 850nm)$	Rotation angle of scanning mirror (a)	g'	$\Delta g'_{deflection}$
1.71913135	-4.5	28.74785260	0.06245010
1.71913135	-4.0	28.73463495	0.04923244
1.71913135	-3.5	28.72302152	0.03761902
1.71913135	-3.0	28.71299365	0.02759115
1.71913135	-2.5	28.70453531	0.01913280
1.71913135	-2.0	28.69763302	0.01223052
1.71913135	-1.5	28.69227585	0.00687335
1.71913135	-1.0	28.68845532	0.00305282
1.71913135	-0.5	28.68616541	0.00076290
1.71913135	0.0	28.68540250	0.00000000
1.71913135	0.5	28.68616541	0.00076290
1.71913135	1.0	28.68845532	0.00305282
1.71913135	1.5	28.69227585	0.00687335
1.71913135	2.0	28.69763302	0.01223052

1.71913135	2.5	28.70453531	0.01913280
1.71913135	3.0	28.71299365	0.02759115
1.71913135	3.5	28.72302152	0.03761902
1.71913135	4.0	28.73463495	0.04923244
1.71913135	4.5	28.74785260	0.06245010

Table C3 Diffraction angle for wavelength $l = 800nm$

$q'(l = 800nm)$	Rotation angle of scanning mirror (a)	g'	$\Delta g'_{deflection}$
0.00000000	-4.5	28.77238627	0.08698377
0.00000000	-4.0	28.75397496	0.06857245
0.00000000	-3.5	28.73779870	0.05239620
0.00000000	-3.0	28.72383132	0.03842881
0.00000000	-2.5	28.71205031	0.02664781
0.00000000	-2.0	28.70243680	0.01703430
0.00000000	-1.5	28.69497543	0.00957293
0.00000000	-1.0	28.68965433	0.00425183
0.00000000	-0.5	28.68646504	0.00106254
0.00000000	0.0	28.68540250	0.00000000
0.00000000	0.5	28.68646504	0.00106254
0.00000000	1.0	28.68965433	0.00425183
0.00000000	1.5	28.69497543	0.00957293

0.00000000	2.0	28.70243680	0.01703430
0.00000000	2.5	28.71205031	0.02664781
0.00000000	3.0	28.72383132	0.03842881
0.00000000	3.5	28.73779870	0.05239620
0.00000000	4.0	28.75397496	0.06857245
0.00000000	4.5	28.77238627	0.08698377

Table C4 Diffraction angle for wavelength $l = 750nm$

$q'(l = 750nm)$	Rotation angle of scanning mirror (a)	g'	$\Delta g'_{deflection}$
-1.71913135	-4.5	28.79668487	0.11128236
-1.71913135	-4.0	28.77312970	0.08772719
-1.71913135	-3.5	28.75243435	0.06703185
-1.71913135	-3.0	28.73456520	0.04916269
-1.71913135	-2.5	28.71949336	0.03409085
-1.71913135	-2.0	28.70719458	0.02179208
-1.71913135	-1.5	28.69764917	0.01224667
-1.71913135	-1.0	28.69084186	0.00543936
-1.71913135	-0.5	28.68676180	0.00135930
-1.71913135	0.0	28.68540250	0.00000000
-1.71913135	0.5	28.68676180	0.00135930
-1.71913135	1.0	28.69084186	0.00543936

-1.71913135	1.5	28.69764917	0.01224667
-1.71913135	2.0	28.70719458	0.02179208
-1.71913135	2.5	28.71949336	0.03409085
-1.71913135	3.0	28.73456520	0.04916269
-1.71913135	3.5	28.75243435	0.06703185
-1.71913135	4.0	28.77312970	0.08772719
-1.71913135	4.5	28.79668487	0.11128236

Table C5 Diffraction angle for wavelength $l = 700nm$

$q'(l = 700nm)$	Rotation angle of scanning mirror (a)	g'	$\Delta g'_{deflection}$
-3.43981283	-4.5	28.82061413	0.13521162
-3.43981283	-4.0	28.79199377	0.10659126
-3.43981283	-3.5	28.76684822	0.08144572
-3.43981283	-3.0	28.74513662	0.05973412
-3.43981283	-2.5	28.72682387	0.04142137
-3.43981283	-2.0	28.71188050	0.02647800
-3.43981283	-1.5	28.70028254	0.01488004
-3.43981283	-1.0	28.69201147	0.00660897
-3.43981283	-0.5	28.68705409	0.00165158
-3.43981283	0.0	28.68540250	0.00000000
-3.43981283	0.5	28.68705409	0.00165158

-3.43981283	1.0	28.69201147	0.00660897
-3.43981283	1.5	28.70028254	0.01488004
-3.43981283	2.0	28.71188050	0.02647800
-3.43981283	2.5	28.72682387	0.04142137
-3.43981283	3.0	28.74513662	0.05973412
-3.43981283	3.5	28.76684822	0.08144572
-3.43981283	4.0	28.79199377	0.10659126
-3.43981283	4.5	28.82061413	0.13521162

For the maximum rotation angle 4.5 degree, $\Delta g'_{\max imum} = 0.09739540$ degree has been produced among the broad band wavelength light source. However the deflection degree of the back-scattered light from the incoming direction will be $\Delta g'_{\max imum\ \ deflection} = 0.13521162$ degree.

C.2. Below is some simulation results when problem of optics alignment has been introduced into system. We will see the effects when there is a little slight displacement between lens and diffraction grating or scanning mirror separately.

Assume that $\Delta y = 0.01, \Delta z = 0.00$, this means the optics alignment displacement between lens and diffraction grating nearly equals to 0.5mm.

Table C6 Diffraction angle for wavelength $l = 900nm$

$q'(l = 900nm)$	Rotation angle of scanning mirror (a)	g'	$\Delta g'_{deflection}$
3.43981283	-4.5	28.72292847	0.03752597

3.43981283	-4.0	28.71495893	0.02955643
3.43981283	-3.5	28.70796003	0.02255752
3.43981283	-3.0	28.70192062	0.01651812
3.43981283	-2.5	28.69683116	0.01142865
3.43981283	-2.0	28.69268361	0.00728111
3.43981283	-1.5	28.68947148	0.00406898
3.43981283	-1.0	28.68718972	0.00178722
3.43981283	-0.5	28.68583475	0.00043224
3.43981283	0.0	28.68540250	0.00000000
3.43981283	0.5	28.68589871	0.00049620
3.43981283	1.0	28.68731728	0.00191478
3.43981283	1.5	28.68966294	0.00426044
3.43981283	2.0	28.69293930	0.00753680
3.43981283	2.5	28.69715149	0.01174898
3.43981283	3.0	28.70230610	0.01690359
3.43981283	3.5	28.70841126	0.02300876
3.43981283	4.0	28.71547664	0.03007414
3.43981283	4.5	28.72351348	0.03811098

Table C7 Diffraction angle for wavelength $l = 850nm$

q' ($l = 850nm$)	Rotation angle of scanning mirror (a)	g'	$\Delta g'_{deflection}$

1.71913135	-4.5	28.74761231	0.06220981
1.71913135	-4.0	28.73442242	0.04901991
1.71913135	-3.5	28.72283640	0.03743390
1.71913135	-3.0	28.71283565	0.02743315
1.71913135	-2.5	28.70440417	0.01900167
1.71913135	-2.0	28.69752854	0.01212604
1.71913135	-1.5	28.69219785	0.00679535
1.71913135	-1.0	28.68840368	0.00300118
1.71913135	-0.5	28.68614004	0.00073753
1.71913135	0.0	28.68540250	0.00000000
1.71913135	0.5	28.68619258	0.00079008
1.71913135	1.0	28.68850877	0.00310626
1.71913135	1.5	28.69235566	0.00695315
1.71913135	2.0	28.69773932	0.01233682
1.71913135	2.5	28.70466826	0.01926576
1.71913135	3.0	28.71315348	0.02775097
1.71913135	3.5	28.72320847	0.03780596
1.71913135	4.0	28.73484932	0.04944681
1.71913135	4.5	28.74809474	0.06269224

Table C8 Diffraction angle for wavelength $l = 800nm$

$q'(l = 800nm)$	Rotation angle of	g'	$\Delta g'_{deflection}$

	scanning mirror (a)		
0.00000000	-4.5	28.77238627	0.08698377
0.00000000	-4.0	28.75397496	0.06857245
0.00000000	-3.5	28.73779870	0.05239620
0.00000000	-3.0	28.72383132	0.03842881
0.00000000	-2.5	28.71205031	0.02664781
0.00000000	-2.0	28.70243680	0.01703430
0.00000000	-1.5	28.69497543	0.00957293
0.00000000	-1.0	28.68965433	0.00425183
0.00000000	-0.5	28.68646504	0.00106254
0.00000000	0.0	28.68540250	0.00000000
0.00000000	0.5	28.68646504	0.00106254
0.00000000	1.0	28.68965433	0.00425183
0.00000000	1.5	28.69497543	0.00957293
0.00000000	2.0	28.70243680	0.01703430
0.00000000	2.5	28.71205031	0.02664781
0.00000000	3.0	28.72383132	0.03842881
0.00000000	3.5	28.73779870	0.05239620
0.00000000	4.0	28.75397496	0.06857245
0.00000000	4.5	28.77238627	0.08698377

Table C9 Diffraction angle for wavelength $l = 750nm$

$q'(l=750nm)$	Rotation angle of scanning mirror (a)	g'	$\Delta g'_{deflection}$
-1.71913135	-4.5	28.79711639	0.11171389
-1.71913135	-4.0	28.77351172	0.08810922
-1.71913135	-3.5	28.75276749	0.06736499
-1.71913135	-3.0	28.73484999	0.04944749
-1.71913135	-2.5	28.71973026	0.03432776
-1.71913135	-2.0	28.70738399	0.02198148
-1.71913135	-1.5	28.69779137	0.01238886
-1.71913135	-1.0	28.69093708	0.00553458
-1.71913135	-0.5	28.68681022	0.00140772
-1.71913135	0.0	28.68540250	0.00000000
-1.71913135	0.5	28.68671660	0.00131410
-1.71913135	1.0	28.69074985	0.00534735
-1.71913135	1.5	28.69751020	0.01210769
-1.71913135	2.0	28.70700842	0.02160591
-1.71913135	2.5	28.71925969	0.03385719
-1.71913135	3.0	28.73428365	0.04888115
-1.71913135	3.5	28.75210448	0.06670197
-1.71913135	4.0	28.77275096	0.08734846
-1.71913135	4.5	28.79625664	0.11085414

Table C10 Diffraction angle for wavelength $l = 700nm$

q' ($l = 700nm$)	Rotation angle of scanning mirror (a)	g'	$\Delta g'_{deflection}$
-3.43981283	-4.5	28.82166826	0.13626576
-3.43981283	-4.0	28.79292742	0.10752492
-3.43981283	-3.5	28.76766291	0.08226041
-3.43981283	-3.0	28.74583367	0.06043116
-3.43981283	-2.5	28.72740439	0.04200189
-3.43981283	-2.0	28.71234543	0.02694292
-3.43981283	-1.5	28.70063264	0.01523013
-3.43981283	-1.0	28.69224733	0.00684482
-3.43981283	-0.5	28.68717628	0.00177378
-3.43981283	0.0	28.68540250	0.00000000
-3.43981283	0.5	28.68694765	0.00154514
-3.43981283	1.0	28.69179132	0.00638882
-3.43981283	1.5	28.69994818	0.01454567
-3.43981283	2.0	28.71143133	0.02602882
-3.43981283	2.5	28.72625915	0.04085665
-3.43981283	3.0	28.74445544	0.05905293
-3.43981283	3.5	28.76604945	0.08064695
-3.43981283	4.0	28.79107611	0.10567361
-3.43981283	4.5	28.81957608	0.13417358

Above simulation results has shown that a slight displacement between diffraction grating and lens has no much obvious effect on the emanative angle.

C.3. Assume that $\Delta y = 0.00, \Delta z = 0.01$, this means the optics alignment displacement between lens and scanning mirror nearly equals to 0.5mm.

Table C11 Diffraction angle for wavelength $l = 900nm$

q' ($l = 900nm$)	Rotation angle of scanning mirror (a)	g'	$\Delta g'_{deflection}$
3.43981283	-4.5	28.62035074	-0.06505176
3.43981283	-4.0	28.62393916	-0.06146335
3.43981283	-3.5	28.62844035	-0.05696215
3.43981283	-3.0	28.63385093	-0.05155158
3.43981283	-2.5	28.64016895	-0.04523355
3.43981283	-2.0	28.64739392	-0.03800858
3.43981283	-1.5	28.65552673	-0.02987577
3.43981283	-1.0	28.66456971	-0.02083280
3.43981283	-0.5	28.67452658	-0.01087592
3.43981283	0.0	28.68540250	0.00000000
3.43981283	0.5	28.69720405	0.01180155
3.43981283	1.0	28.70993924	0.02453674
3.43981283	1.5	28.72361757	0.03821507
3.43981283	2.0	28.73825000	0.05284750

3.43981283	2.5	28.75384904	0.06844654
3.43981283	3.0	28.77042876	0.08502626
3.43981283	3.5	28.78800483	0.10260233
3.43981283	4.0	28.80659458	0.12119208
3.43981283	4.5	28.82621707	0.14081457

Table C12 Diffraction angle for wavelength $l = 850nm$

$q'(l = 850nm)$	Rotation angle of scanning mirror (a)	g'	$\Delta g'_{deflection}$
1.71913135	-4.5	28.64453670	-0.04086581
1.71913135	-4.0	28.64296602	-0.04243648
1.71913135	-3.5	28.64293936	-0.04246314
1.71913135	-3.0	28.64444609	-0.04095641
1.71913135	-2.5	28.64747808	-0.03792443
1.71913135	-2.0	28.65202964	-0.03337286
1.71913135	-1.5	28.65809752	-0.02730498
1.71913135	-1.0	28.66568088	-0.01972163
1.71913135	-0.5	28.67478123	-0.01062127
1.71913135	0.0	28.68540250	0.00000000
1.71913135	0.5	28.69755100	0.01214850
1.71913135	1.0	28.71123543	0.02583293
1.71913135	1.5	28.72646695	0.04106444

1.71913135	2.0	28.74325914	0.05785664
1.71913135	2.5	28.76162812	0.07622562
1.71913135	3.0	28.78159256	0.09619006
1.71913135	3.5	28.80317375	0.11777124
1.71913135	4.0	28.82639567	0.14099316
1.71913135	4.5	28.85128508	0.16588258

Table C13 Diffraction angle for wavelength $l = 800nm$

$q'(l = 800nm)$	Rotation angle of scanning mirror (a)	g'	$\Delta g'_{deflection}$
0.00000000	-4.5	28.66890813	0.08698377
0.00000000	-4.0	28.66216568	0.06857245
0.00000000	-3.5	28.65759678	0.05239620
0.00000000	-3.0	28.65518341	0.03842881
0.00000000	-2.5	28.65491115	0.02664781
0.00000000	-2.0	28.65676903	0.01703430
0.00000000	-1.5	28.66074956	0.00957293
0.00000000	-1.0	28.66684859	0.00425183
0.00000000	-0.5	28.67506537	-0.01033714
0.00000000	0.0	28.68540250	0.00000000
0.00000000	0.5	28.69786595	0.01246345
0.00000000	1.0	28.71246504	0.02706254

0.00000000	1.5	28.72921250	0.04380999
0.00000000	2.0	28.74812448	0.06272198
0.00000000	2.5	28.76922064	0.08381814
0.00000000	3.0	28.79252420	0.10712170
0.00000000	3.5	28.81806200	0.13265950
0.00000000	4.0	28.84586462	0.16046211
0.00000000	4.5	28.87596648	0.19056398

Table C14 Diffraction angle for wavelength $l = 750nm$

$q'(l = 750nm)$	Rotation angle of scanning mirror (a)	g'	$\Delta g'_{deflection}$
-1.71913135	-4.5	28.69333087	0.00792837
-1.71913135	-4.0	28.68143283	-0.00396967
-1.71913135	-3.5	28.67233243	-0.01307008
-1.71913135	-3.0	28.66600429	-0.01939821
-1.71913135	-2.5	28.66242767	-0.02297483
-1.71913135	-2.0	28.66158631	-0.02381620
-1.71913135	-1.5	28.66346838	-0.02193412
-1.71913135	-1.0	28.66806645	-0.01733606
-1.71913135	-0.5	28.67537742	-0.01002509
-1.71913135	0.0	28.68540250	0.00000000
-1.71913135	0.5	28.69814725	0.01274474

-1.71913135	1.0	28.71362151	0.02821901
-1.71913135	1.5	28.73183950	0.04643700
-1.71913135	2.0	28.75281985	0.06741735
-1.71913135	2.5	28.77658563	0.09118312
-1.71913135	3.0	28.80316446	0.11776195
-1.71913135	3.5	28.83258861	0.14718610
-1.71913135	4.0	28.86489510	0.17949260
-1.71913135	4.5	28.90012586	0.21472335

Table C15 Diffraction angle for wavelength $l = 700nm$

$q'(l = 700nm)$	Rotation angle of scanning mirror (a)	g'	$\Delta g'_{deflection}$
-3.43981283	-4.5	28.71767052	0.03226801
-3.43981283	-4.0	28.70066188	0.01525938
-3.43981283	-3.5	28.68706589	0.00166339
-3.43981283	-3.0	28.67684991	-0.00855259
-3.43981283	-2.5	28.66998693	-0.01541558
-3.43981283	-2.0	28.66645544	-0.01894706
-3.43981283	-1.5	28.66623936	-0.01916314
-3.43981283	-1.0	28.66932795	-0.01607456
-3.43981283	-0.5	28.67571573	-0.00968678
-3.43981283	0.0	28.68540250	0.00000000

-3.43981283	0.5	28.69839332	0.01299082
-3.43981283	1.0	28.71469849	0.02929598
-3.43981283	1.5	28.73433358	0.04893108
-3.43981283	2.0	28.75731954	0.07191704
-3.43981283	2.5	28.78368270	0.09828020
-3.43981283	3.0	28.81345491	0.12805240
-3.43981283	3.5	28.84667361	0.16127110
-3.43981283	4.0	28.88338202	0.19797951
-3.43981283	4.5	28.92362927	0.23822676

Above simulation results has shown that a slight displacement between scanning mirror and lens has obvious effect on the emanative angle. It will amplify the emanative angle and some wavelength light can't go back into system. So it is important to improve the accuracy of distance between scanning mirror and lens.

When problem of the optics alignment has been introduced into system, for the maximum rotation angle 4.5 degree, $\Delta g'_{\max imum} = 0.09741220$ degree has been produced among the broad band wavelength light source. However the deflection degree from the incoming direction will be $\Delta g'_{\max imum\ \ deflection} = 0.23822676$ degree. It can be seen that the problem of the optics alignment between diffraction grating and lens has no much effect on the emanative angle. However, the problem of the optics alignment between scanning mirror and lens will amplify the emanative angle, it will cause the back-reflected light deflect more from the incoming light.

Experiments have shown that the spectrum of back-reflected light has been greatly affected

by the slight deflection $\Delta g'$. Broad spectrum has been reduced to narrow spectrum. Some part of light can't go back into OCT system.

C.4. We further to simulate the diffraction angle g_1' when the light comes from double-pass mirror and go to diffraction grating again. Assume that $\Delta y = 0.00, \Delta z = 0.00$, below is some simulation results.

Table C16 Diffraction angle for wavelength $l = 900nm$

$q_1'(l = 900nm)$	Rotation angle of scanning mirror (a)	g_1'	$\Delta g'_{1deflection}$
3.47305427	-4.5	28.68491339	-0.00048911
3.46601817	-4.0	28.68509851	-0.00030399
3.45983627	-3.5	28.68522500	-0.00017750
3.45449853	-3.0	28.68530702	-0.00009549
3.44999636	-2.5	28.68535658	-0.00004592
3.44632252	-2.0	28.68538374	-0.00001876
3.44347114	-1.5	28.68539657	-0.00000593
3.44143767	-1.0	28.68540133	-0.00000117
3.44021888	-0.5	28.68540243	-0.00000008
3.43981283	0.0	28.68540250	0.00000000
3.44021888	0.5	28.68540243	-0.00000008
3.44143767	1.0	28.68540133	-0.00000117
3.44347114	1.5	28.68539657	-0.00000593

3.44632252	2.0	28.68538374	-0.00001876
3.44999636	2.5	28.68535658	-0.00004592
3.45449853	3.0	28.68530702	-0.00009549
3.45983627	3.5	28.68522500	-0.00017750
3.46601817	4.0	28.68509851	-0.00030399
3.47305427	4.5	28.68491339	-0.00048911

Table C17 Diffraction angle for wavelength $l = 850nm$

$q_1'(l = 850nm)$	Rotation angle of scanning mirror (a)	g_1'	$\Delta g'_{1deflection}$
1.77395866	-4.5	28.68458116	-0.00082134
1.76235152	-4.0	28.68489205	-0.00051045
1.75215441	-3.5	28.68510446	-0.00029804
1.74335044	-3.0	28.68524218	-0.00016033
1.73592512	-2.5	28.68532541	-0.00007709
1.72986629	-2.0	28.68537100	-0.00003151
1.72516405	-1.5	28.68539255	-0.00000996
1.72181074	-1.0	28.68540053	-0.00000197
1.71980093	-0.5	28.68540238	-0.00000012
1.71913135	0.0	28.68540250	0.00000000
1.71980093	0.5	28.68540238	-0.00000012
1.72181074	1.0	28.68540053	-0.00000197

1.72516405	1.5	28.68539255	-0.00000996
1.72986629	2.0	28.68537100	-0.00003151
1.73592512	2.5	28.68532541	-0.00007709
1.74335044	3.0	28.68524218	-0.00016033
1.75215441	3.5	28.68510446	-0.00029804
1.76235152	4.0	28.68489205	-0.00051045
1.77395866	4.5	28.68458116	-0.00082134

Table C18 Diffraction angle for wavelength $l = 800nm$

$q_1'(l = 800nm)$	Rotation angle of scanning mirror (a)	g_1'	$\Delta g'_{1deflection}$
0.07633981	-4.5	28.68424553	-0.00115697
0.06017615	-4.0	28.68468348	-0.00071902
0.04597704	-3.5	28.68498270	-0.00041981
0.03371857	-3.0	28.68517669	-0.00022582
0.02338026	-2.5	28.68529391	-0.00010859
0.01494487	-2.0	28.68535813	-0.00004438
0.00839842	-1.5	28.68538849	-0.00001402
0.00373008	-1.0	28.68539973	-0.00000277
0.00093214	-0.5	28.68540232	-0.00000018
0.00000000	0.0	28.68540250	0.00000000
0.00093214	0.5	28.68540232	-0.00000018

0.00373008	1.0	28.68539973	-0.00000277
0.00839842	1.5	28.68538849	-0.00001402
0.01494487	2.0	28.68535813	-0.00004438
0.02338026	2.5	28.68529391	-0.00010859
0.03371857	3.0	28.68517669	-0.00022582
0.04597704	3.5	28.68498270	-0.00041981
0.06017615	4.0	28.68468348	-0.00071902
0.07633981	4.5	28.68424553	-0.00115697

Table C19 Diffraction angle for wavelength $l = 750nm$

$q_1'(\ l = 750nm)$	Rotation angle of scanning mirror (a)	g_1'	$\Delta g'_{1deflection}$
-1.62141350	-4.5	28.68391355	-0.00148895
-1.64210570	-4.0	28.68447717	-0.00092533
-1.66028202	-3.5	28.68486225	-0.00054025
-1.67597341	-3.0	28.68511190	-0.00029060
-1.68920642	-2.5	28.68526277	-0.00013974
-1.70000334	-2.0	28.68534540	-0.00005710
-1.70838229	-1.5	28.68538446	-0.00001804
-1.71435730	-1.0	28.68539894	-0.00000357
-1.71793833	-0.5	28.68540228	-0.00000023
-1.71913135	0.0	28.68540250	0.00000000

-1.71793833	0.5	28.68540228	-0.00000023
-1.71435730	1.0	28.68539894	-0.00000357
-1.70838229	1.5	28.68538446	-0.00001804
-1.70000334	2.0	28.68534540	-0.00005710
-1.68920642	2.5	28.68526277	-0.00013974
-1.67597341	3.0	28.68511190	-0.00029060
-1.66028202	3.5	28.68486225	-0.00054025
-1.64210570	4.0	28.68447717	-0.00092533
-1.62141350	4.5	28.68391355	-0.00148895

Table C20 Diffraction angle for wavelength $l = 700nm$

$q_1'(l = 700nm)$	Rotation angle of scanning mirror (a)	g_1'	$\Delta g'_{1deflection}$
-3.32091256	-4.5	28.68359229	-0.00181021
-3.34609184	-4.0	28.68427752	-0.00112498
-3.36820896	-3.5	28.68474569	-0.00065681
-3.38730186	-3.0	28.68504920	-0.00035331
-3.40340307	-2.5	28.68523262	-0.00016989
-3.41653993	-2.0	28.68533308	-0.00006943
-3.42673463	-1.5	28.68538058	-0.00002193
-3.43400435	-1.0	28.68539817	-0.00000433
-3.43836132	-0.5	28.68540223	-0.00000027

-3.43981283	0.0	28.68540250	0.00000000
-3.43836132	0.5	28.68540223	-0.00000027
-3.43400435	1.0	28.68539817	-0.00000433
-3.42673463	1.5	28.68538058	-0.00002193
-3.41653993	2.0	28.68533308	-0.00006943
-3.40340307	2.5	28.68523262	-0.00016989
-3.38730186	3.0	28.68504920	-0.00035331
-3.36820896	3.5	28.68474569	-0.00065681
-3.34609184	4.0	28.68427752	-0.00112498
-3.32091256	4.5	28.68359229	-0.00181021

From the simulation results, we can know that double-pass mirror has solved perfectly the problem of the emanative angle. $\Delta g'_{1\ deflection}$ has been reduced to nearly omitted angle. All wavelength light component will nearly parallel the incoming direction and go back into OCT system.